Doctoral Dissertations and Master's Theses

2017

On the Interaction between Gravity Waves and Atmospheric Thermal Tides

Ryan Matthew Agner
Embry-Riddle Aeronautical University

Follow this and additional works at: https://commons.erau.edu/edt

Part of the Atmospheric Sciences Commons

ON THE INTERACTION BETWEEN GRAVITY WAVES AND ATMOSPHERIC THERMAL TIDES

BY

RYAN MATTHEW AGNER

A dissertation submitted in partial fulfillment of the requirements for the degree of Doctor of Philosophy of Engineering Physics at Embry-Riddle Aeronautical University, 2017

ON THE INTERACTION BETWEEN GRAVITY WAVES AND ATMOSPHERIC THERMAL TIDES

By

Ryan Matthew Agner

This Dissertation was prepared under the direction of the candidate's Dissertation Committee Chair, Dr. Alan Z. Liu and has been approved by the members of his dissertation committee. It was submitted to the College of Arts and Sciences and was accepted in partial fulfillment of the requirements for the

Degree of

Doctor of Philosophy in Engineering Physics.

Dr. Alan Z. Liu, Ph.D
Committee Chair

Dr. Michael P. Hickey, Ph.D
Committee Member

Dr. Jonathan B. Snively, Ph.D
Committee Member

Dr. Gary R. Swenson, Ph.D
Committee Member

Dr. Terry Oswalt, Ph.D
Department Chair, Physical Sciences

Dr. Michael P. Hickey, Ph.D
Dean of Research and Graduate Studies

Dr. Karen Gaines, Ph.D
Dean, College of Arts and Sciences

05/05/2017
Date

ii

Acknowledgements

I would first like to thank my wife of 8 years, Nikisha. She is one of the major reasons that I chose to pursue my Ph.D. and has been a constant source of love and support in the entire time I have known her. You are my life, thank You for everything. I also want to send my love to our 2 year old daughter Nora.

I would like to thank Dr. Alan Liu for providing the guidance throughout the dissertation work and writing. Your ideas and suggestions were invaluable to my effort of this entire project. Many thanks to you for allowing me to be with my family while completing this degree. To my committee members Dr. Hickey, Dr. Snively and Dr. Swenson, thank you for lending your time and expertise in reviewing this body of work.

Thanks go to my Mother, Carole Rogers and my Father, Samuel Agner Jr. for your unconditional love and support throughout my entire life and for instilling in me your values, morals and ethics that guide me. Thanks also go to my older sister, Amanda and my younger sister, Sarah. We have all been through good times and bad times and have emerged from them with stronger bonds than before. To my mother-in-law and sister-in-law I would like to express my gratitude for everything you have given both of us, from coming all the way from India to help take care of Nora while I finished this degree and for your love. Thanks are given to my entire family for everything you have given me throughout my life.

Abstract

Gravity waves and thermal tides are two of the most important dynamical features of the atmosphere. They are both generated in the lower atmosphere and propagate upward transporting energy and momentum to the upper atmosphere. This dissertation focuses on the interaction of these waves in the Mesosphere and Lower Thermosphere (MLT) region of the atmosphere using both observational data and Global Circulation Model (GCMs). The first part of this work focuses on observations of gravity wave interactions with the tides using both LIDAR data at the Star Fire Optical Range (SOR, 35°N, 106.5°W) and a meteor radar data at the Andes LIDAR Observatory (ALO, 30.3°S, 70.7°W). At SOR, the gravity waves are shown to enhance or damp the amplitude of the diurnal variations dependent on altitude while the phase is always delayed. The results compare well with previous mechanistic model results and with the Japanese Atmospheric General circulation model for Upper Atmosphere Research (JAGUAR) high resolution global circulation model. The meteor radar observed the GWs to almost always enhance the tidal amplitudes and either delay or advance the phase depending on the altitude. When compared to previous radar results from the same meteor radar when it was located in Maui, Hawaii, the Chile results are very similar while the LIDAR results show significant differences. This is because of several instrument biases when calculating GW momentum fluxes that is not significant when determining the winds. The radar needs to perform large amounts of all-sky averaging across many weeks, while the LIDAR directly detects waves in a small section of sky.

The second part of this work focuses on gravity wave parameterization scheme effects on the tides in GCMs. The Specified Dynamics Whole Atmosphere Community Climate

Model (SD-WACCM) and the extended Canadian Middle Atmosphere Model (eCMAM) are used for this analysis. The gravity wave parameterization schemes in the eCMAM (Hines scheme) have been shown to enhance the tidal amplitudes compared to observations while the parameterization scheme in SD-WACCM (Lindzen scheme) overdamps the tides. It is shown here that the Hines scheme assumption that only small scale gravity waves force the atmosphere do not create enough drag to properly constrain the tidal amplitudes. The Lindzen scheme produces too much drag because all wave scales are assumed to be saturated thus continuing to provide forcing on the atmosphere above the breaking altitude.

The final part of this work investigates GWs, tides and their interactions on a local time scale instead of a global scale in the two GCMs. The local time GWs in eCMAM are found to have a strong seasonal dependence, with the majority of the forcings at the winter pole at latitudes where the diurnal variations are weak limiting their interactions. In SD-WACCM, the largest local GW forcings are located at mid latitudes near where the diurnal variations peak causing them to dampen the diurnal amplitudes. On a local time level the diurnal variations may be a summation of many tidal modes. The analysis reveals that in eCMAM the DW1 tidal mode is by far the dominant mode accounting for the local time variations. The high amount of modulation of GWs by the DW1 tidal winds does not allow it to be properly constrained, causing it to dominate the local time diurnal variations. Similarly, the DW1 projection of GW forcing is dominant over all other other modes and contributes the most to the local time diurnal GW variations. The local time wind variations in SD-WACCM are influenced by several tidal modes because the DW1 tide is of compatible amplitudes to other modes. This is because of the increased damping on the tide by the GWs. It is also found that the local GW diurnal variations have significant contributions from all tidal modes due to the time and location of the forcing being dependent only on the tropospheric source regions and not the at altitude tidal winds.

Contents

List of Figures

List of Tables

Chapter 1

Introduction

Upper atmospheric features are affected by a multitude of lower atmospheric waves which transport energy and momentum from the troposphere into the Mesosphere-Lower Thermosphere (MLT) region. Gravity waves (GWs) are a major source of this energy transport system and can be generated from flow over orography, convective storms or frontal systems. They are local scale waves having horizontal wavelengths from a few tens of kilometers up to a few thousand but have been shown to have global scale effects. As they propagate upward from the source regions in the troposphere their amplitudes will grow due to decreasing density. At some altitude the waves amplitude will grow too large and will break depositing their energy and momentum into the background flow. A seasonal dependence in the preferential direction of breaking GWs in the MLT region, due to a seasonal dependence in the stratospheric jets, causes eastward (westward) accelerations of the mean winds in the summer (winter) hemisphere. The Coriolis effect then causes these accelerations to turn towards the winter hemisphere inducing a meridional circulation at these altitudes from the summer pole to the winter pole. To conserve mass, a corresponding upward (downward) adiabatic flow is created at the summer (winter) poles. The upward expansion of the air at the summer pole causes the temperatures to lower while the downward compression at the winter pole increases the temperatures creating the cold summer mesopause (*Lindzen*, 1981). GWs are also known to modify the Quasi Biennial Oscillation (*Xue et al.*, 2012a)

and can also affect the atmospheric thermal tides.

Thermal tides are another major feature of the atmosphere. Unlike GWs, the tides are a global scale persistent feature of the atmosphere. They are generated by solar heat absorption of tropospheric water vapor and stratospheric ozone. The main thermal tide reflects its solar heating source with a diurnal (24 hour) period with maximum amplitudes at tropical latitudes. Several sub-harmonics (12hr, 8hr, 6hr) also exists and are important at other latitudes (*Chapman and Lindzen*, 1970). When propagating upward these waves also grow in amplitude reaching maximums in the MLT region similar to GWs. Due to their large amplitudes and nearly constant presence, they have major affects on many atmospheric and ionospheric dynamics (*Immel et al.*, 2006).

GWs are one dynamical feature affected by the tides but an inverse relationship also exists wherein the GWs can change the tidal amplitudes and phases. The tides act as a slowly varying background to GWs which, due to the large scale difference between the two, modulates the GWs. When the GWs break, they transfer their energy into the background winds of which the tides are a major component. The interactions between the two have been extensively studied in the past through observations and models but a complete picture is still lacking. In observations, it is very difficult to parse the tides from the observed diurnal variations using a single ground based instrument. The variability and intermittency of GWs also poses a challenge (*Liu et al.*, 2013). For models, computational limits force a parameterization of GWs which include many assumptions on GW propagation and dissipation due to limited observational constraints. More investigations are needed to properly and realistically constrain GW parameterization schemes.

1.1 Motivation and Outline

The main goal of this work is to investigate how different assumptions about GW propagation and dissipation in current parameterization schemes affect the thermal tide. There

are three major parts in this dissertation. Two of them use two separate GCM's to study the GW affects on the tides with the third using two different observational techniques. Each part seeks to answer one or two of the following science questions of this work:

1. How do small scale GWs effect the local diurnal variations in observations?

2. How does the Lindzen and Hines GW parameterization schemes affect the tidal amplitudes?

3. What is the effect of the parameterized GWs on local time diurnal variations in eCMAM and SD-WACCM?

4. Which tidal components contribute most to the local time diurnal variations in eCMAM and SD-WACCM?

To answer these questions, this dissertation is divided into several chapters as described here. Chapter 2 provides a detailed description of GWs and tides, their mathematical derivations from first principles with some observations and modeling results of each. Descriptions of how GWs and tides can interact with each other are also included.

The GW parameterization schemes in GCMs contain many tunable parameters that account for GW mechanisms that are not well understood. Observations are used to constrain these parameters. For the GW parameterizations, the zonal mean zonal winds are the main atmospheric property used to tune the schemes with the tidal amplitudes and phases not typically considered. Chapter 3 of this dissertation presents observations of the GW-tidal interactions to help inform future work on modeling GWs. The chapter is separated into two major parts. The first part is based upon work submitted to the Journal of Atmospheric and Solar-Terrestrial Physics which uses a LIDAR station in New Mexico to derive GW modulation by the diurnal variations and GW affects on the amplitude and phases of the diurnal variations. The second part of the chapter is similar but instead uses a meteor radar located in Chile. It also compares the results from the LIDAR in New Mexico and the

same meteor radar when it was in Maui, Hawaii to determine any instrument biases when analyzing GW-tidal interactions. This chapter answers the first scientific question.

Chapter 4 is based upon a work submitted to the Journal of Geophysical Research: Atmospheres and studies how some assumptions in the Lindzen and Hines GW parameterization schemes affect the DW1 tide in GCMs. Each scheme was created using a separate set of assumptions about how GWs propagate and dissipate. Previous studies have revealed that models which use the Lindzen scheme tend to supress the tidal amplitudes compared to observations (*England et al.*, 2006; *McLandress*, 1998) while those that use the Hines scheme tend to enhance them (*McLandress*, 1998; *Meyer*, 1999). In this chapter, the DW1 tide and the background winds are analyzed with the GW forcing calculated from the parametrization schemes to determine which basic GW assumptions may cause the discrepancies in the tide. This works to answer the second scientific question.

One caveat of comparing GCM results of the tides and ground based observations is that the tides are an inherently global feature while a single location can only detect variations that may contain a summation of several tidal modes. Chapter 5 again studies the affects of GW parameterization schemes on the tide but on a local time scale in both the eCMAM and SD-WACCM providing a more direct comparison to observations. This analysis can also determine which of the tidal modes are most responsible for the local time variations in the winds and GW forcing in the models. Chapter 5 addresses both the third and fourth scientific questions. The conclusions for this work are in chapter 6.

Chapter 2

Thermal Tide and Gravity Waves

2.1 Atmospheric Thermal Tides

2.1.1 Introduction

The concept of tides is very familiar to most people in terms of the rising and falling ocean levels at the shore. Atmospheric thermal tides have not entered the common language in the same manner. While both ocean and atmospheric tides share a similar name, they are very different in their sources, behavior and effects on the planet. Ocean tides are generated by the asymmetric gravitational pull of the moon on opposite sides of the earth. The gravitational pull on the side nearest the moon is stronger than on the side facing away. The effect is to rise the ocean levels on both the near and opposite sides of the earth creating a strong semidiurnal wave. The moon's tidal forces can also affect the atmosphere but since the density is lower the change is far smaller (*Akmaev*, 2006).

Atmospheric thermal tides are created through daily heating of the atmosphere by the sun and as such have a strong diurnal component with some subharmonics reaching comparable amplitudes. The solar heating mainly occurs in the lower atmosphere by tropospheric water vapor and stratospheric ozone (*Forbes*, 1995). The wave then propagates into the upper atmosphere increasing in amplitude reaching a maximum in the MLT region. Here the tides
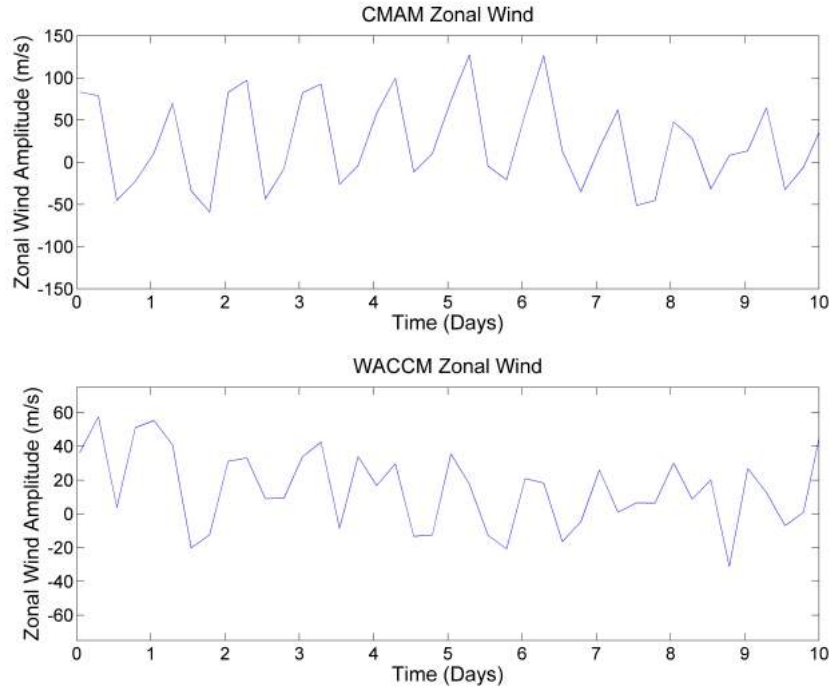
Figure 2.1: Zonal wind (m/s) for the first 10 days of March 2006 at $100°$ longitude, $30°$ latitude and 95km altitude from eCMAM (top) and SD-WACCM (bottom).

are of equivalent amplitudes to the background winds and are a dominant dynamical feature. Figure 2.1 shows the zonal winds for the first 10 days of March 2006 at $100°$ longitude, $30°$ latitude and 95 km altitude. The top plot is results from the eCMAM while the bottom is from the SD-WACCM. Neither model specifies the creation of the tides with both generated self-consistently. In both models, the most noticeable pattern is the daily variation in the wind amplitude indicating the diurnal thermal tides. Here, the diurnal tide is by far the strongest dynamical feature in the winds.

Due to their large amplitudes the interactions between tides and other features of the atmosphere are very important. They can interact with other large scale wave such as planetary waves, which can have periods of several days generating non-migrating tides (*Mayr et al.*, 2003; *Hagan and Roble*, 2001). The tidal winds can push ions in the lower ionosphere affecting the E-layer dynamo electric fields causing detectable modulations in the F-region of the ionosphere (*Immel et al.*, 2006). Tides also interact with smaller scale
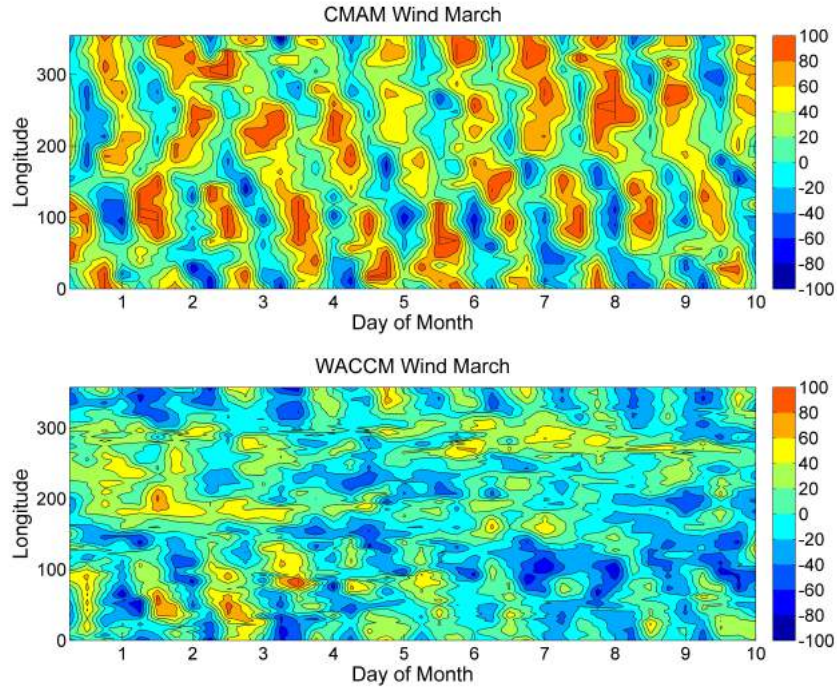
Figure 2.2: Zonal wind (m/s) at 95km altitude and -25° latitude for the first ten days of March 2006 from eCMAM (top) and SD-WACCM (bottom).

gravity waves. The changing background atmospheric conditions modulate gravity wave propagation while gravity waves themselves may adjust tidal amplitudes and structures (*Liu et al.*, 2013; *Agner and Liu*, 2015; *Ortland and Alexander*, 2006).

The thermal tides are global scale waves in both longitude and time. Figure 2.2 shows the zonal winds in both models again over the first 10 days of March but with an additional longitude dimension at -25° latitude and 95 km altitude. In CMAM the diurnal variations are clearly seen with the phase lines moving westward with time. This is due to the westward motion of the sun and thus the solar heating moving across the earth. This is also seen in WACCM but not as clearly and will be discussed in later chapters.

Since the source of the thermal tides is the daily heating action of the atmosphere by the sun, the main tide will have a diurnal period with a latitude dependent wavelength. This heating is not perfectly sinusoidal throughout the day, leading to several subharmonics appearing at different latitudes and altitudes. A general two dimensional global scale wave

7

may be written as:

$$f(\lambda, t) = A(\lambda, t)\sin(\sigma\Omega t + s\lambda - \phi(\lambda, t)) \tag{2.1}$$

where λ is the longitude, t is time, ϕ is the time and longitude dependent phase, A is the longitude and time dependent amplitude and $\Omega = (2\pi)/86400$ is the earths radial frequency. The quantity σ is an integer that represents multiples of the earths rotation rate so that $\sigma = (1, 2, 3)$ is a wave with a (24 hr, 12 hr, 8 hr) period. The zonal wavenumber, s, may be negative or positive. A migrating tide occurs when $\sigma = s$ which means that the tidal phase is not dependent on longitude. Since the sun is the main source of the thermal tides and moves westward with time, a westward (eastward) propagating wave is defined to have a positive (negative) zonal wavenumber. Tidal components are typically specified by pairs of σ and s. The main tide for instance is the (1,1) tidal component indicating it has a diurnal period and propagating westward with a zonal wavenumber of one. An eastward propagating semidiurnal with a zonal wavenumber of 2 tide would be indicated by (2,-2). A common alternate method to specify the tidal component uses letters and a single number. A "D", "S" or "T" are used for the diurnal, semidiurnal or terdiurnal wave periods and the propagation direction is written as "W", "E" or "S" for westward, eastward or stationary. The absolute value of the zonal wavenumber is used instead of the full value since the direction is already specified. In this notation convention the (1,1) tidal component is the DW1 tide and the (2,-2) is the SE2 tide. This is the more common convention and will be used throughout this work.

2.1.2 Classical Tidal Theory

The classical theory of tides provides a simplified description of the wave modes that are supported by the atmosphere. It assumes the atmosphere is motionless and isothermal and involves linearizing the momentum, continuity, and thermodynamic equations to derive a

single eigenfunction eigenvalue equation describing the waves. Separation of variables is then used to obtain Laplace's tidal equation to describe the latitudinal dependence of the wave modes and the vertical structure equation to describe the vertical structure. A shortened version of the theory is presented here with more details found in *Chapman and Lindzen* (1970) and *Forbes* (1995)

To begin the horizontal momentum equations in spherical coordinates are

$$\frac{Du}{Dt} - \frac{uv}{a}\tan\phi - fv = -\frac{\partial\Phi}{a\cos\phi\partial\lambda},$$
$$\frac{Dv}{Dt} - \frac{u^2}{a}\tan\phi - fu = -\frac{\partial\Phi}{a\partial\phi}, \qquad (2.2)$$

where a is the earth's radius, $\Phi = g*height$ is the geopotential height, and λ and ϕ are the spherical coordinate in the zonal and meridional directions. The full time derivatives in spherical coordinates is defined as

$$\frac{D}{Dt} = \frac{\partial}{\partial t} + u\frac{\partial}{a\cos\phi\partial\lambda} + v\frac{\partial}{a\partial\phi} + w\frac{\partial}{\partial z}. \qquad (2.3)$$

The continuity equation in spherical coordinates is given by

$$\frac{1}{a\cos\phi}\left(\frac{\partial u}{\partial\lambda} + \frac{\partial v\cos\phi}{\partial\phi}\right) + \frac{\partial w}{\partial z} + \frac{w}{H} = 0, \qquad (2.4)$$

where u, v and w are the zonal meridional and vertical winds respectively, z is the coordinate in the vertical direction and H is the scale height of the atmosphere which is around 7-8 km. The thermodynamic equation is

$$\frac{D\theta}{Dt} = 0, \qquad (2.5)$$

where θ is the potential temperature. Using the conversion between geometric and pressure coordinates and the definition for potential temperature a relation between θ and Φ can be

found as follows

$$z = H\ln\left(\frac{p_0}{p}\right),$$

$$\theta = T_0\left(\frac{p_0}{p}\right)^{R/C_p}.$$

(2.6)

Substituting and rearraging,

$$\kappa = R/C_p,$$

$$\frac{\theta}{T_0} = \left(\frac{p_0}{p}\right)^{\kappa},$$

$$\ln\theta = \ln T_0 + \kappa\frac{z}{H}.$$

(2.7)

Now taking the definition of the geopotential height and substituting this relation in we find

$$\frac{\partial\Phi}{\partial z} = g = \frac{RT_0}{H} = \frac{R}{H}\theta e^{-\kappa z/H}.$$

(2.8)

The five equations, (2.2), (2.4), (2.5), and (2.8) are a set of governing equations for a shallow atmosphere on a spherical earth. To find waves that are supported by the atmosphere the equations must first be linearized by introducing perturbations to all quantities in a motionless, isothermal basic state. The linearization process is shown below for the zonal momentum equation so the reader may understand how it is performed in other sections. First replace the dynamical terms with a mean plus the perturbation (e.g., $u \to \overline{u} + u'$).

$$\frac{Du}{Dt} - \frac{uv}{a}\tan\phi - fv = -\frac{\partial\Phi}{a\cos\phi\partial\lambda},$$

$$\frac{D(\overline{u} + u')}{Dt} - \frac{(\overline{u} + u')(\overline{v} + v')}{a}\tan\phi - f(\overline{v} + v') = -\frac{\partial(\overline{\Phi} + \Phi')}{a\cos\phi\partial\lambda}.$$

(2.9)

From here, several terms may be ignored. First, any term with a mean alone is dropped since only the perturbed quantities are needed. In addition, nonlinear quantities with two perturbations multiplied together may also be ignored, since a small term multiplied with a small term is even smaller. The zonal momentum equation then becomes,

$$\frac{Du'}{Dt} - fv' = -\frac{\partial\Phi'}{a\cos\phi\partial\lambda},$$

(2.10)

Using the same linearization method, the other four governing equations become,

$$\frac{Dv'}{Dt} - fv' = -\frac{\partial \Phi'}{a \cos\phi \partial\phi},$$

$$\frac{1}{a \cos\phi}\left(\frac{\partial u'}{\partial\lambda} + \frac{\partial v' \cos\phi}{\partial\phi}\right) + \frac{\partial w'}{\partial z} - \frac{w'}{H} = 0,$$

$$\frac{\partial \Phi'}{\partial z} = \frac{R}{H}e^{-\kappa z/H}\theta',$$

$$\frac{\partial \theta'}{\partial t} + \frac{\kappa\bar{\theta}}{H}w' = 0,$$

(2.11)

where the last line is the linearized thermodynamic equation and is derived from (2.5) by rearranging, taking a full derivative and linearizing. To find wave solutions from these linearized governing equations sinusoidal solutions in longitude and time are assumed in the following form,

$$(u',v',w',\Phi',\theta') = Re([\tilde{u},\tilde{v},\tilde{u},\tilde{\Phi},\tilde{\theta}]e^{is\lambda - \omega t}),$$

(2.12)

where the terms with tilde are complex amplitudes, s is the wavenumber in longitude, and ω is the radial frequency. The solutions are substituted into (2.10) and (2.11) eliminating the time and longitude derivatives which become,

$$-i\omega\tilde{u} - f\tilde{v} = -\frac{is\tilde{\Phi}}{a \cos\phi},$$

$$-i\omega\tilde{v} - f\tilde{u} = -\frac{\tilde{\Phi}}{a\partial\phi},$$

$$\frac{1}{a \cos\phi}(is\tilde{u} + \frac{\partial\tilde{v}\cos\phi}{\partial\phi}) + \frac{\partial\tilde{w}}{\partial z} - \frac{\tilde{w}}{H} = 0,$$

(2.13)

$$\frac{\partial\tilde{\Phi}}{\partial z} = \frac{R}{H}e^{-\kappa z/H}\tilde{\theta},$$

$$-i\omega\tilde{\theta} + \frac{\kappa\bar{\theta}}{H}\tilde{w} = 0.$$

11

Next the $\widetilde{u}$ and $\widetilde{v}$ are found in terms of the geopotential from the momentum equations,

$$\widetilde{u} = -\frac{1}{a(f^2 - \omega^2)}\left(\frac{ws\widetilde{\Phi}}{\cos\phi} + f\frac{\partial\widetilde{\Phi}}{\partial\phi}\right),$$

$$\widetilde{v} = -\frac{i}{a(f^2 - \omega^2)}\left(\frac{fs\widetilde{\Phi}}{\cos\phi} + \omega\frac{\partial\widetilde{\Phi}}{\partial\phi}\right). \tag{2.14}$$

The last two equations of (2.11) can be solved together, eliminating $\widetilde{\theta}$,

$$-i\omega\frac{\partial\Phi}{\partial z} + \kappa\frac{Re^{-\kappa z/H}}{H^2}\overline{\theta}\widetilde{w} = 0, \tag{2.15}$$

which with the Brunt Väisälä frequency and the potential temperature in an iosthermal atmosphere become

$$N^2 = \frac{\kappa g}{H},$$

$$\overline{\theta} = T_0 e^{\kappa z/H}, \tag{2.16}$$

and (2.8) becomes,

$$-i\omega\frac{\partial\Phi}{\partial z} + N^2\widetilde{w} = 0. \tag{2.17}$$

Solving for $\widetilde{w}$,

$$\widetilde{w} = \frac{i\omega}{N^2}\frac{\partial\widetilde{\Phi}}{\partial z}. \tag{2.18}$$

Substituting equations (2.14) and (2.18) into the linearized continuity equation yields a single, separable boundary value equation where the z and ϕ subscripts refer to derivatives with respect to those paramerters,

$$\widetilde{\Phi}_{zz} - \frac{\widetilde{\Phi}_z}{H} + \frac{N^2}{\omega a^2\cos\phi}\left(\frac{-s^2\omega\widetilde{\Phi} - fs\widetilde{\Phi}_\phi\cos\phi}{(f^2 - \omega^2)\cos\phi} + \left[\frac{fs\widetilde{\Phi} + \omega\widetilde{\Phi}_\phi\cos\phi}{f^2 - \omega^2}\right]_\phi\right) = 0. \tag{2.19}$$

Using a separation of variables the equation becomes,

$$\frac{Z_{zz} - Z_z/H}{Z} = \frac{1}{\Theta}\frac{N^2}{\omega a^2\cos\phi}\left(\frac{s^2\omega\Theta + fs\Theta_\phi}{(f^2 - \omega^2)\cos\phi} - \left[\frac{fs\Theta + \omega\Theta_\phi}{f^2 - \omega^2}\right]_\phi\right), \tag{2.20}$$

12

where Z and Θ are general solutions for the ordinary differential equation. Setting the right hand side of (2.20) to a separation constant, $-N^2/gh$, gives Laplace's Tidal Equation (*Laplace*, 1825). This is a latitudinally dependent equation describing wave modes supported by the atmosphere. Laplace derived this equation in the 18$^{\text{th}}$ century to describe the behavior of a shallow ocean that covers the earth. The shallow ocean in this case is the atmopshere,

$$\frac{N^2}{\omega a^2 \cos\phi} \left(\frac{s^2\omega\Theta + fs\Theta_\phi \cos\phi}{(f^2-\omega^2)\cos\phi} - \left[\frac{fs\Theta + \omega\Theta_\phi \cos\phi}{f^2-\omega^2} \right]_\phi \right) + \frac{N^2}{gh}\Theta = 0. \tag{2.21}$$

This can be written in a more standard simplified form by normalizing the frequency by the Earth's rotation and a simple change of variables as follows,

$$-\left[\frac{\Theta_\mu(1-\mu^2)}{\mu^2-\nu^2} \right]_\mu + \frac{1}{\mu^2-\nu^2}\left[\frac{s^2}{1-\mu^2} + \frac{s(\mu^2+\nu^2)}{\nu(\mu^2-\nu^2)} \right]\Theta + \gamma\Theta = 0, \tag{2.22}$$

where $\nu = \omega/(2\Omega)$, $\mu = \sin\phi$, and $\gamma = \dfrac{4\Omega^2 a^2}{gh}$, which is called Lamb's Parameter. Laplace's equation has eigenfunction solutions in discreet sets of wave frequencies and wavenumbers. Traditionally, the nomenclature for identifying specific frequency-wavenumber pairs are in the form of (s,n) with s being the wavenumber and n being the meridional wave index which is related to the number of wave nodes in the latitudinal direction. These solutions are known as Hough functions due to Sydney Samuel Hough's work in providing solutions for Laplace's equation (*Hough*, 1898). It is very difficult to analytically solve for these Hough modes but it can be easily done numerically. Figure 2.3 shows the numerically solved solutions of Laplace's tidal equation using a recent method developed by *Wang et al.* (2016) for several dominant Hough modes. This method solves the tidal equation using normalized associated Legendre polynomial expansions. The boundary conditions for the solutions are that $\Theta = 0$ when $\mu = -1$ and 1 which are the poles. As seen in the plots some modes are symmetric about the equator while others are antisymmetric. The symmetry can quickly be determined from the values of s and n with symmetric modes having an even $s+n$ while antisymmetric modes
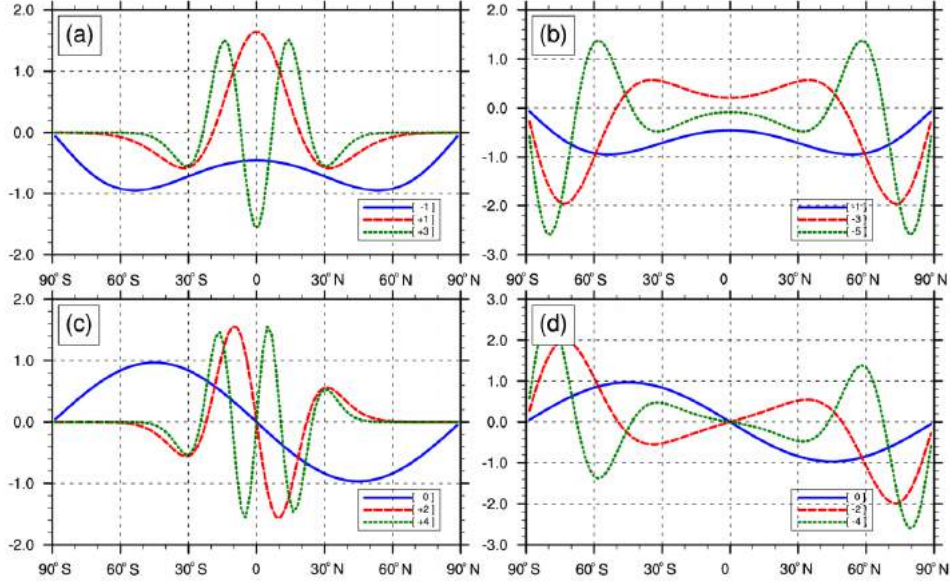
Figure 2.3: Symmetric (a,b) and antisymmetric (c,d) Hough modes for DW1 computed using associated Legendre polynomial expansions. The labels represent the value of n (*Wang et al.*, 2016).

have an odd $s+n$. Additionally, a negative value of n indicates a westward propagating mode while a positive value indicates an eastward mode.

Whether a mode propagates away from its source region is determined by first setting the left hand side of equation (2.20) equal to the separation constant,

$$Z_{zz} - \frac{1}{H}Z_z + \frac{N^2}{gh}Z = 0, \tag{2.23}$$

giving what is known as the vertical structure equation. A general solution for this is,

$$Z = Ae^{z/2H}exp\left[\left(\pm\sqrt{\frac{1}{4H^2} - \frac{N^2}{gh}}\right)z\right]. \tag{2.24}$$

The scale height does not change very much with altitude, so the terms inside the brackets will determine if the wave will propagate into the upper altitudes. If the term under the square root has a positive value, the exponential term will either decay, the negative solution, or grow infinitely, the positive solution, with altitude. Infinite growth is not realistic since

it would require infinite energy so this solution would decay exponentially with altitude resulting in a mode that is trapped at its source altitude. If the term under the square root is negative, then

$$Z \propto exp\left[\left(\pm i\sqrt{\frac{N^2}{gh} - \frac{1}{4H^2}}\right)z\right],\qquad(2.25)$$

which is a solution that will propagate with altitude. The only term that can vary is the h which is the equivalent depth and describes the depth of a shallow ocean that will yield modes with the same frequencies and horizontal structure as our atmosphere. Solving for h gives the relation,

$$0 < h < \frac{4H^2N^2}{g},\qquad(2.26)$$

describing conditions when waves will propagate away from the source region. Using both Laplace's Tidal Equation and the vertical structure equation together, the latitudinal and vertical structures of a wave mode may be found. The Hough mode solution for a specific mode will give the latitudinal structure. The equavalent depth can then be found through Lamb's parameter giving the vertical structure from equation (2.24).

2.1.3 Thermal Tidal Heating

The wave modes we are interested in here are the thermal atmospheric tides which are forced through absorption of solar energy by the atmosphere. With the earth undergoing a full rotation once every 24 hours, the suns position across the earth has a 24 hour or diurnal period of heating and cooling resulting in a strong diurnal wave mode. The heating of the atmosphere has a dependence on latitude due to the curvature of the earth with higher latitudes receiving less direct light. Figure 2.4 shows an example of this uneven heating rate of the earth-atmosphere system at 225° longitude at 18UT on March 15 2006 from the eCMAM. In order for a Hough mode to strongly respond to the heating, its latitudinal structure needs to be projected relatively well on to the profile. To find which Hough modes are able to most efficiently absorb the solar radiation it can be assumed that the heating
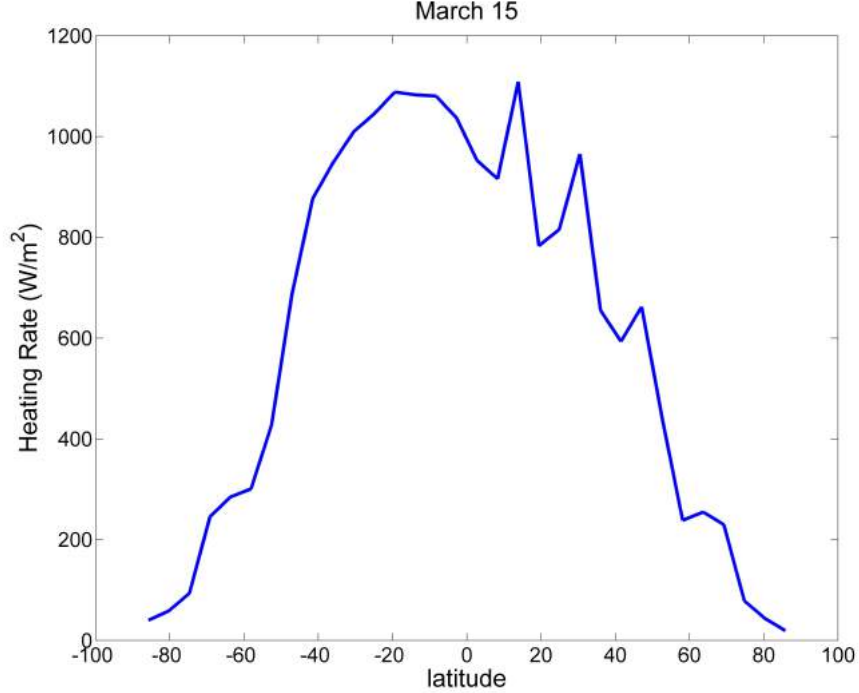
Figure 2.4: Heating Rates of the earth-atmosphere system at $225°$ longitude on March 15 2006, 18UT in CMAM.

rate is separable as:

$$\frac{\partial Q}{\partial t} = J = \sum_s \sum_n \sum_\omega \Theta_n(\phi) Q_n(z) e^{i(s\lambda + \omega t)}, \tag{2.27}$$

where Q is the heat term and Θ_n are the Hough functions. The heating rates of various atmospheric constituents can be found from models and decomposed into the Hough functions using least squares fits. Figure 2.5 shows the vertical structure of heating rates for several Hough modes for the O_2, O_3 and H_2O vapor from a radiative transfer model called PHODIS (*Vichare and Rajaram*, 2013); the left plot shows the diurnal vertical heating rates, while the right shows the semidiurnal.

The heating rates for Hough modes of the same period widely vary with the relative differences being very similar between constituents. In the diurnal plot, the (1,-2) mode absorbs the most heat by far, with the (1,1) and (1,-4) modes being very similar. Even
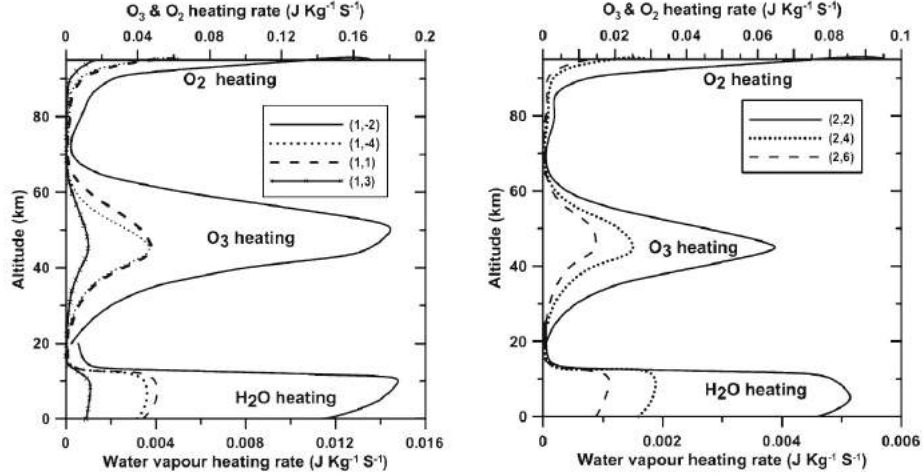
Figure 2.5: Diurnal (left) and semidiurnal (right) vertical heating rates due to O_3, O_2 and H_2O vapor decomposed into Hough functions at equinox (*Vichare and Rajaram*, 2013).

though the (1,-2) mode dominates the heat absorption, it is a trapped mode because h=-12.2703 and will not propagate away from the source region (*Forbes*, 1995). As a result this mode does not have much significance in the MLT region. The (1,-4) mode is also largely trapped with h=-1.7581. The (1,1) mode on the other hand will propagate upward, h=0.6909, with increasing amplitude and is the most significant mode observed in the upper atmosphere. For the semidiurnal heating rates, the (2,2), h=7.8519, is the largest and the (2,4), h=2.1098, and (2,6), h=0.9565, modes are smaller. Unlike the diurnal modes, all three of these semidiurnal modes are vertically propagating (*Forbes*, 1995).

2.2 Gravity Waves

2.2.1 Introduction

While the thermal tides are global scale atmospheric waves forced by the sun, gravity waves (GWs) are a more localized dynamical feature whose sources are primarily located in the lower atmosphere. They have a wide variety of periods from a few minutes up to the inertial period ($2\pi/f$) and horizontal scales from tens to thousands of kilometers (*Fritts and*

17

Alexander, 2003). A GW is produced when a parcel of air is displaced vertically through any number of mechanisms discussed below. When an air parcel is dislocated upward it moves into a region of lower density air so that it becomes heavier relative to its surroundings. At this point, the parcel will sink down due to gravity. Its downward acceleration will then cause it to overshoot its original equilibrium position sinking into a higher density environment. Now the parcel will begin to rise again due to bouyancy back towards equilibrium. It will again overshoot and this process will continue until the energy is lost to the surrounding air. The waves have an overall upward propagation as even those launched downward will reflect off the ground and is responsible for much of the energy and momentum transfer from lower altitudes into the upper atmosphere.

A modeled example of GWs is shown in Fig. 2.6 from the high resolution WACCM. The standard default version of this model has a horizontal resolution of 2.5° in longitude and 1.9° in latitude. The vertical resolution varies with altitude; it is 3.5 km above 65 km, 1.75 km around 50 km altitude, 1.1-1.4 km below 30 km and 1.1 km in the tropopause and much higher in the planetary boundary layer (*Liu et al.*, 2014). The horizontal resolution especially is too coarse to directly resolve GW so they must be parameterized. More details about the parameterization scheme are discussed in a later chapter. The WACCM used for the figure has an increased horizontal resolution of 0.25° in longitude and latitude with a 0.1 scale height vertical resolution. For these simulations the GW parameterizations are turned off so the only GWs in the model are directly resolved waves. At this time in the model a tropical cyclone is present at 167° east and 20° south and is at the center of a series of circular waves seen at most altitudes. The waves are shown to increase in amplitude with altitude as expected and became a global scale feature in the mesosphere and lower thermosphere. Even with the increased resolution the model can only resolve larger GWs. This caused some dynamical features such as the stratosphere/mesosphere jet to not close at the correct altitudes due to insufficient zonal forcing suggesting that smaller scale GWs are very important in the overall momentum budget of the atmosphere.
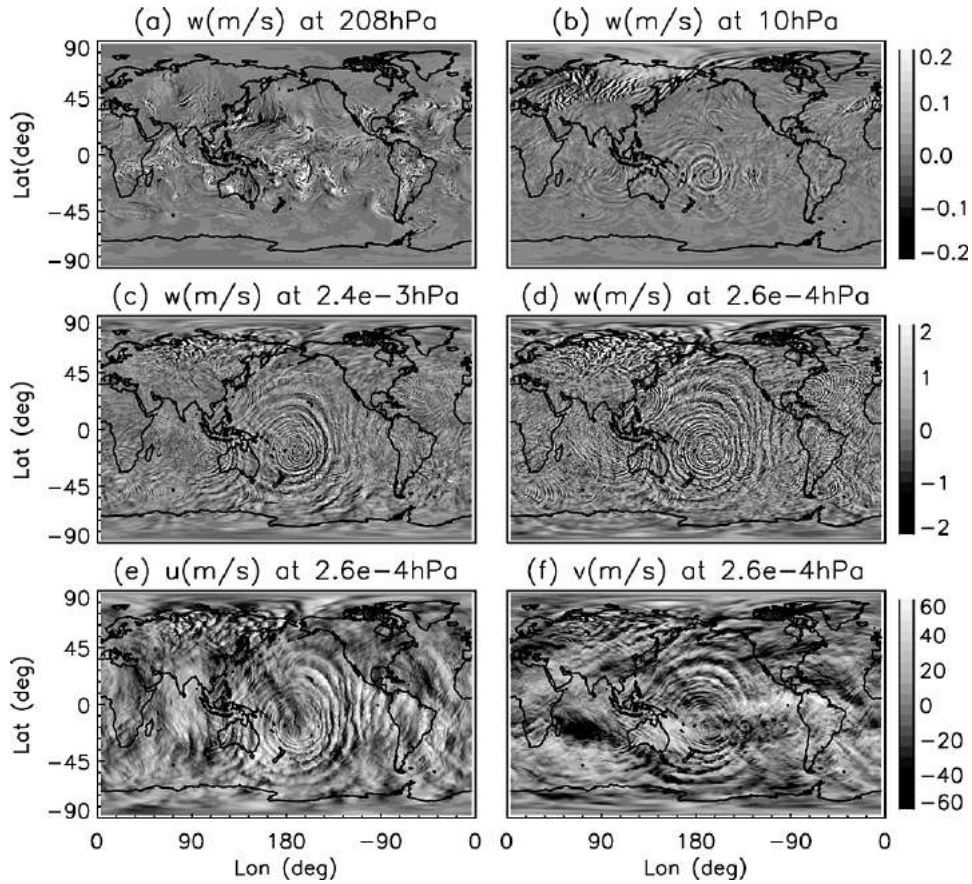
Figure 2.6: Winds results from the high resolution WACCM showing the scale of some GWs. The approximate altitudes in each panel are 11 km (a), 30 km (b), 87 km (c) and 100 km (d,e,f). Only the vertical winds are shown at the lower altitudes because the horizontal perturbations due to GW are much smaller than other dynamical features at these altitudes. All wind components are shown at 100 km (*Liu et al.*, 2014).

Sources for GWs are separated into two main categories, orographic and non-orographic. Orographic GWs are also known as mountain waves due to the way in which they are created. When air flows over topography such as mountains air parcels are lifted up from their equilibrium altitudes into the lower density higher altitudes creating GWs. For steady background wind, the phase speeds of mountain waves are zero relative to the ground because the mechanism lifting the air does not move. Numerical studies have shown that mountain waves are important in tropospheric weather dynamics where wave breaking can influence the large scale flows in the troposphere and lower stratosphere (*McFarlane*, 1987). They can also reach mesospheric heights and have been observed with horizontal wavelengths of around 10-100km (*Bacmeister et al.*, 1990; *Alexander et al.*, 2009; *Jiang and Doyle*, 2008).

Non-orographic GWs are generated in a variety of ways and include a full range of possible wavelengths and frequencies. Some examples of non-orographic sources include convective systems such as thunderstorms and typhoons, moving frontal systems and wind shear (*Fritts and Alexander*, 2003). While it has been known that these dynamical features produce gravity waves, the wave spectra generated by specific sources are not well understood. For instance, a wave must first be observed in the atmosphere through an observational technique that gives the waves traveling direction and speed so that its point origin may be estimated. With the travel time and direction discovered a dynamical feature must also be present at the correct time and location. This is often not the case because the observed GW may not have been from a source that is easily identifiable like a storm but from wind shear or secondary generation from other breaking waves. Establishing the spectra of different wave sources requires a multitude of GW observations with known origins. This is quite difficult because of the complex dynamics and intermittency of these sources.

While it is difficult to ascertain the exact source of a particular GW, observations are plentiful in the upper atmosphere. GWs are able to be observed directly with instruments such as airglow imagers or LIDAR's and indirectly by measuring momentum fluxes with different types of radars. In some cases GW signatures may be seen in lower atmospheric
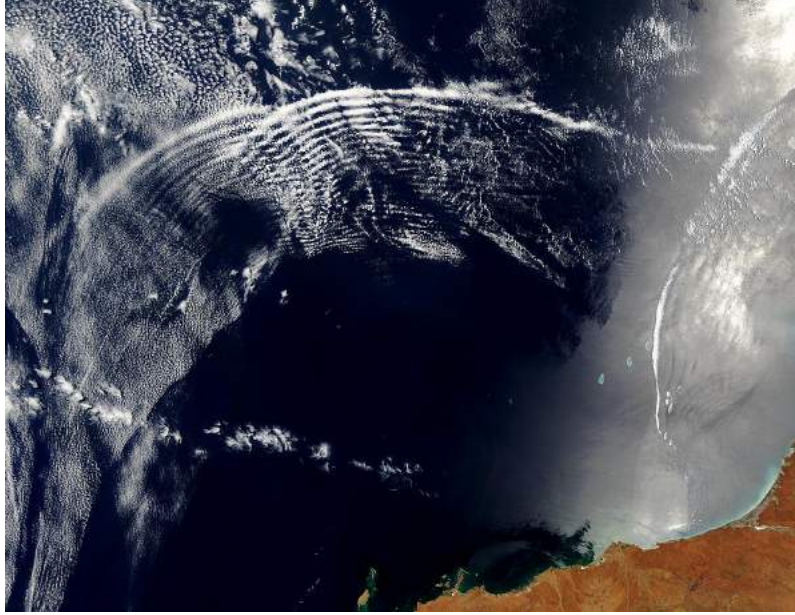
Figure 2.7: Observation of two separate GW moving through a cloud layer near Australia on November 11, 2003. Photo was taken by the MODIS instrument onboard the Terra satellite (*Descloitres*, 2003).

clouds. Figure 2.7 shows two overlapping GWs traveling through the cloud layer away from the Australian coast on November 11, 2003. As seen here the source for GW may be quite far from its current location even in the lower atmosphere due to the angle at which they propagate. These particular waves are thought to be orographic waves from a mountain range near the Australian coast.

As GWs propagate upward, they will encounter changing background wind conditions which can change their properties or cause them to break. If the background wind is in the same direction as the horizontal GW propagation the wind will reduce the intrinsic frequency of the wave. If the instrinsic frequency is reduced to zero the wave will break and its energy is deposited into the background flow. This process is known as critical layer filtering (*Nappo*, 2013). It can occur at any point in the atmosphere but is common at the stratospheric jet altitude due to its strength and relative consistency. An important consequence of this filtering is that the majority of GWs that are able to reach mesospheric heights tend to propagate opposite the stratospheric jet since they are able to pass through.

When these GW travel into the MLT region, their amplitudes will continue to grow because of the decrease in density. At a certain altitude depending on the background winds, the waves will break or become saturated. A GW is saturated (amplitude limited) when the horizontal wind amplitude in the wave propagation direction becomes equal to the GW's intrinsic phase speed which is the phase speed of the wave relative to the wind in the propagation direction (*Lindzen*, 1981; *Ejiri et al.*, 2009). As this point is approached the energy and momentum in the wave, which originated in the lower troposphere, will begin to transfer into the mean winds. It is this energy transport mechanism which provides an important balance and coupling to the entire atmosphere.

One of the more notable effects of GW breaking in the MLT region is the cold summer mesopause which is the coldest region of the atmosphere. As stated above GW in the mesosphere have a preferential direction due to critical layer filtering in the stratosphere. In the summer hemisphere, the westward flow in the stratosphere causes an eastward preference in mesopheric GW. When these waves break and deposit their momentum into the mean westward mesospheric winds, the overall effect is to decelerate the flow. In the winter hemisphere, the preferentially westward propagating GWs decelerate the mean eastward winds in the mesosphere. The Coriolis force will act to turn the decelerated flow in both hemispheres toward the winter pole inducing an overall flow from the summer pole to the winter pole. The flow at the summer pole pulls air from lower altitudes and cool it adiabatically producing the cold summer mesopause (*Fritts and Alexander*, 2003; *Garcia and Solomon*, 1985; *Yamashita*, 2008).

GWs have also been linked numerically to the Quasi Biennial Oscillation (QBO), which is an alternating pattern of eastward and westward stratospheric zonal mean winds in low latitudes (*Baldwin et al.*, 2001; *Giorgetta et al.*, 2002; *Schirber et al.*, 2015). The average period for the oscillations is 26 months with a maximum amplitude of around 20m/s. *Xue et al.* (2012b) found that when including Coriolis force effects in the WACCM gravity wave parameterization scheme, effectively including inertial GW, the QBO was able to be pro-

duced internally within the model without the need to impose it directly. *Kim et al.* (2013) specifically parameterized convective GWs in the Met Office Unified Model which resulted in QBO variabilities that are closer to observations. This behavior is not limited to GCM's. For example, an extended version of the U.S. Navy's operational numerical weather prediction model, NAVGEM, implemented a stochastic Lindzen based GW parameterization scheme. Using this scheme the QBO was reproduced internally within the weather model (*McCormack et al.*, 2015).

2.2.2 Linear Theory

Much of the original work on gravity wave mathematical theory was established by *Hines* (1960) and is summarized here. In this treatment the atmosphere is assumed to be stationary and isothermal. To begin the equations of conservation of momentum in the horizontal and vertical directions are (*Fritts and Alexander*, 2003);

$$
\begin{aligned}
\frac{Du}{Dt} - fv + \frac{1}{\rho}\frac{\partial p}{\partial x} &= X, \\
\frac{Dv}{Dt} - fu + \frac{1}{\rho}\frac{\partial p}{\partial y} &= Y, \\
\frac{Dw}{Dt} + \frac{1}{\rho}\frac{\partial p}{\partial z} &= 0,
\end{aligned}
\tag{2.28}
$$

where X and Y are non-conservative forces. Cartesian coordinates are used here instead of spherical coordinates due to the smaller local scales of GW. The conservation of mass and energy are

$$
\begin{aligned}
\frac{1}{\rho}\frac{D\rho}{Dt} + \frac{\partial u}{\partial x} + \frac{\partial v}{\partial y} + \frac{\partial w}{\partial z} &= 0, \\
\frac{D\theta}{Dt} &= Q,
\end{aligned}
\tag{2.29}
$$

where Q is a heating term that is zero for adiabatic processes. The next step is to linearize this set of equations along with the potential energy equation in equation (2.7). The linearization process is identical to the example shown in the previous section. The heating and non-

conservative forces are assumed to be zero. The linearized set of equations are

$$\frac{Du'}{Dt} + w'\frac{\partial \overline{u}}{\partial z} - fv' + \frac{\partial}{\partial x}\left(\frac{p'}{\overline{\rho}}\right) = 0,$$

$$\frac{Dv'}{Dt} + w'\frac{\partial \overline{v}}{\partial z} - fu' + \frac{\partial}{\partial y}\left(\frac{p'}{\overline{\rho}}\right) = 0,$$

$$\frac{Dw'}{Dt} + \frac{\partial}{\partial z}\left(\frac{p'}{\overline{\rho}}\right) - \frac{1}{H}\left(\frac{p'}{\overline{\rho}}\right) + g\left(\frac{\rho'}{\overline{\rho}}\right) = 0,$$

$$\frac{D}{Dt}\left(\frac{\theta'}{\overline{\theta}}\right) + w'\frac{N^2}{g} = 0,$$ (2.30)

$$\frac{D}{Dt}\left(\frac{\rho'}{\overline{\rho}}\right) + \frac{\partial u'}{\partial x} + \frac{\partial v'}{\partial y} + \frac{\partial w'}{\partial z} - \frac{w'}{H} = 0,$$

$$\frac{\theta'}{\overline{\theta}} = \frac{1}{c_s^2}\left(\frac{p'}{\overline{\rho}}\right) - \frac{\rho'}{\overline{\rho}},$$

where c_s is the sound speed, and the total derivatives also linearized as

$$\frac{D}{Dt} = \frac{\partial}{\partial t} + \overline{u}\frac{\partial}{\partial x} + \overline{v}\frac{\partial}{\partial y}.$$ (2.31)

As with the tides, a solution to the set of governing equations is assumed but using all three dimensions plus time instead of just longitude and time. This is due to the localized nature of the interested waves being able to propagate in all directions with time. The solutions take the form of

$$\left(u', v', w', \frac{\theta'}{\overline{\theta}}, \frac{p'}{\overline{\rho}}, \frac{\rho'}{\overline{\rho}},\right) = \left(\tilde{u}, \tilde{v}, \tilde{w}, \tilde{\theta}, \tilde{p}, \tilde{\rho},\right) * \exp\left[i\left(kx + ly + mz - \omega t\right) + \frac{z}{2H}\right],$$ (2.32)

where the tilde terms are the complex amplitudes, H is the atmospheric scale height, and k, l, and m are the wavenumbers in the x, y and z directions respectively. Upon substitution

of the assumed solution the linearized governing equations become

$$-i\hat{\omega}\tilde{u} - f\tilde{v} + ik\tilde{p} = 0,$$

$$-i\hat{\omega}\tilde{v} - f\tilde{u} + il\tilde{p} = 0,$$

$$-i\hat{\omega}\tilde{w} + \left(im - \frac{1}{2H}\right)\tilde{p} = -g\tilde{\rho},$$

$$-i\hat{\omega}\tilde{\theta} + \left(\frac{N^2}{g}\right)\tilde{w} = 0,$$

$$-i\hat{\omega}\tilde{\rho} + ik\tilde{u} + il\tilde{v} + \left(im - \frac{1}{2H}\right)\tilde{w} = 0,$$

$$\tilde{\theta} = \frac{\tilde{p}}{c_s^2} - \tilde{\rho},$$

(2.33)

where $\hat{\omega} = \omega - k\overline{u} - l\overline{v}$ is the intrinsic frequency of the wave and is the frequency observed if the observer is moving with the background instead of being stationary on the ground. These six equations may be combined into a single dispersion relation by demanding the coefficients go to zero,

$$\hat{\omega}^2 = \frac{N^2\left(k^2 + l^2\right) + f^2\left(m^2 + \frac{1}{4H^2}\right)}{k^2 + l^2 + m^2 + \frac{1}{4H^2}}.$$

(2.34)

which may also be written as

$$m^2 = \frac{\left(k^2 + l^2\right)\left(N^2 - \hat{\omega}^2\right)}{\tilde{\omega}^2 - f^2} - \frac{1}{4H^2},$$

(2.35)

This is the GW dispersion relation, which relates intrinsic wave frequency to the horizontal and vertical wavenumbers and the background state. As before, N is the Brunt Väisälä (buoyancy) frequency and is an important quantity for gravity waves describing the maximum frequency of GW that the atmosphere can support. It may be written in terms of the

potential temperature or the density

$$N^2 = \frac{g}{\theta}\frac{\partial \theta}{\partial z}. \tag{2.36}$$

From these equations, the square of the Brunt Väisälä frequency is positive when the potential temperature increases with altitude. Physically the potential temperature describes the temperature a parcel of air would have if it was adiabatically lowered from its initial altitude to a reference level that is typically 1000hPa. If the potential temperature of an air parcel is higher than of its surroundings it will experience a buoyant force and begin to rise, and sink if it is lower than that of its environment due to gravity. When the potential temperature increases with height, air parcels will naturally rise to their equilibrium position leading to atmospheric stability. If it were to decrease with altitude, the air parcels would begin to rise due to buoyancy into regions with even smaller potential temperatures increasing the buoyant force. This would cause instability in the atmosphere leading to overturing until stability is restored. Thus, in addition to describing the maximum frequency supported by the atmosphere, N^2 is also a measure of atmospheric stability with a positive (negative) value indicating a stably (unstably) stratified atmosphere.

GWs are important to the overall momentum and energy balance of the atmosphere so waves that do not propagate vertically from the source regions are typically not extensively studied. From the dispersion relation, if a GW is vertically propagating with real horizontal wavenumbers, the intrinsic frequency must be $|f| < \tilde{\omega} < N$. GWs on the smaller end of this frequency scale have large enough wavelengths to be affected by the Coriolis force and are known as inertial gravity waves. For these waves the horizontal scales are much larger than the vertical ($k^2, l^2 << m^2$) and the dispersion relation can be simplified to

$$\hat{\omega}^2 = \frac{N^2\left(k^2 + l^2\right)}{m^2} + f^2, \tag{2.37}$$

also assuming $m^2 >> 1/4H^2$. The majority of GWs are much smaller scale though and

are closer to the Brunt Väisälä frequency which has a period of around five minutes. For non-inertial waves, $\hat{\omega} >> f$, the horizontal wavenumber can be understood to have only one combined horizontal component, k, since on smaller scales a local coordinate system with the x component taken to be in the wave propagation direction is more convenient. Under this simplification the dispersion relation for smaller scale GW in terms of the observed wave frequency is written as

$$\omega = u_0 k \pm \left[\frac{N^2 k^2}{k^2 + m^2 + \dfrac{1}{4H^2}} \right]^{1/2}, \tag{2.38}$$

where u_0 is the background wind and the Coriolis effect is ignored since it is much smaller than the other terms. From this relation for non-intertial GW, the group velocity (C_g) which descibes the direction of energy propagation can be found using the Boussinesq approximation (*Nappo*, 2013):

$$\begin{aligned} C_{gx} &= \frac{\partial \omega}{\partial k} = u_0 + \frac{m^2}{N^2} \left(c_x - u_0 \right)^3, \\ C_{gz} &= \frac{\partial \omega}{\partial m} = -\frac{k|m|}{N} \left(c_x - u_0 \right)^3, \end{aligned} \tag{2.39}$$

where c_x and c_z are the phase velocities:

$$\begin{aligned} c_x &= \frac{\omega}{k} = u_0 + \frac{N}{k} \cos \beta, \\ c_z &= \frac{\omega}{m} = u_0 \frac{k}{m} + \frac{N}{m} \cos \beta, \\ \cos \beta &= \frac{k}{\sqrt{k^2 + m^2}}, \end{aligned} \tag{2.40}$$

An interesting consequence of the phase and group velocity relations is that GW phase fronts are slanted at some angle β from the horizontal that it is highly dependent on the wave frequency. The sign difference between the vertical group and phase velocities also means that an upward (downward) propagating GW will have downward (upward) propagating phase fronts. A diagram showing the slanted GW phase fronts and the orientation of the phase, c, and group, C_g, velocities is shown in Fig. 2.8. The blue slanted lines are the phase lines of the upward propagating wave with the arrows indicating an air parcels propagation
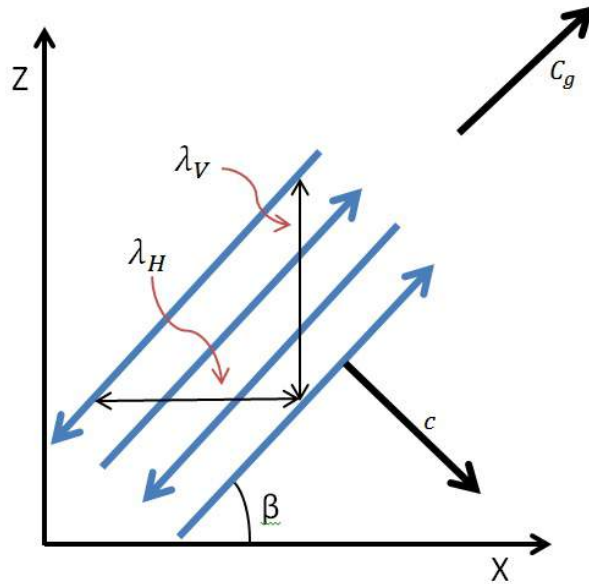
Figure 2.8: Diagram of slanted GW phase fronts showing the vertical and horizontal wavelengths.

direction. The vertical wavelength, λ_v, is defined to be the vertical distance from a phase line to the next line that is 2π away. The horizontal wavelength, λ_h, is the horizontal distance between phase lines that are 2π apart.

2.2.3 GW Momentum Flux

An important property of GWs is their ability to transport and deposit momentum and energy from the lower atmosphere to the upper atmosphere. The vertical flux of horizontal momentum, or simply momentum flux, is used to quantify this and is defined as:

$$\overrightarrow{F}_{mom} = - \left(\rho_0 \overline{u'w'}, \rho_0 \overline{v'w'} \right), \tag{2.41}$$

in the zonal and meridional directions respectively. Estimates of GW momentum flux are essential to parameterization schemes used in models. The magnitude determines where wave breaking levels occur which defines the vertical profile of wave dissipation. This in turn

creates the wave forcing profile that helps to balance the entire model. Many observational studies have been performed to provide estimates of the GW momentum fluxes both at single locations and globally.

Satellites are commonly used to attain a global estimate of the absolute GW momentum fluxes from temperature profiles. *Geller et al.* (2013) used the HIRDLS and SABER satellite data as well as the Vorcore superpressure balloons to calculate GW momentum fluxes in the stratosphere for January and July 2006. The calculated fluxes had a strong seasonal dependence with the summertime GW fluxes much larger than in the winter. There was also a distinct hemispherical dependence with a large peak occurring at both months in the summer hemisphere and a smaller peak in the northern. At the January solstice, the GW momentum fluxes reach up to around 0.75mPa at 40 km and are much lower elsewhere. At the July solstice, the fluxes are much larger reaching a peak of about 6mPa in the HIRDLS data.

Other observational methods can also give GW momentum flux estimates, but are generally only able to derive them at a single location. Meteor radars are a very common method due to their ease of operation, long data sets and observation altitude in the highly dynamic MLT region. Similar to satellites, the momentum fluxes calculated with these radars are an average over some length time. As a result the estimates are for an average of many waves instead of individual wave events. For example, *Placke et al.* (2015) used a MF radar located at Saura (69°N, 16°E) to calculate the GW flux fields from 2008 to 2011. A similar yearly pattern was seen across all the observation years with the momentum fluxes ranging from $10\text{m}^2/\text{s}^2$ to $-10\text{m}^2/\text{s}^2$. The units used here are another common method for representing the momentum flux which is simply the flux as defined in equation (2.41) scaled by the density $(u'w', v'w')$.

Another meteor radar located at a low latitude station in India (8.5°N, 76.9°E) between June 2004 and May 2007 calculated the GW momentum fluxes for a composite year (*Antonita et al.*, 2008). The calculated monthly mean momentum fluxes for this composite year
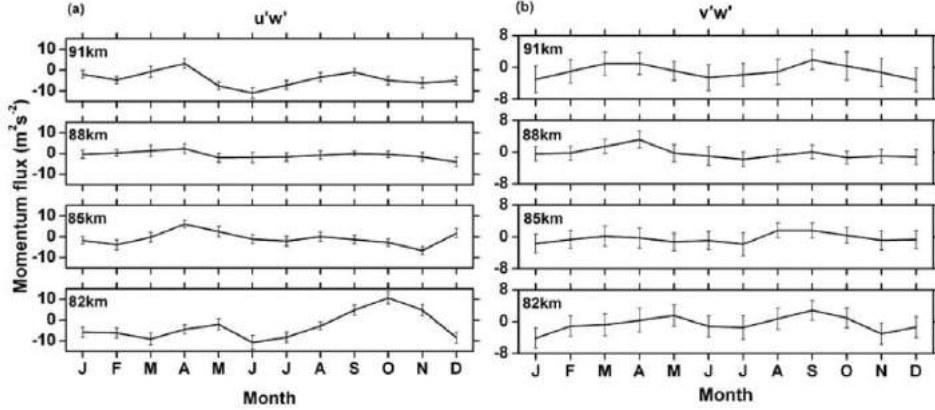
Figure 2.9: Monthly GW momentum flux estimates for a composite year from a meteor radar located in India (8.5°N, 76.9°E) from June 2004 to May 2007 (*Antonita et al.*, 2008).

are shown in Fig. 2.9. The $u'w'$ is shown to vary from -10m^2/s^2 to 10m^2/s^2 similar to the fluxes from Saura while $v'w'$ is about half that of the zonal direction. There is also a semiannual oscillation in the magnitude of the fluxes that was also present in the results from Saura. *Andrioli et al.* (2015) used radars located at three locations at low to mid latitudes around Brazil to calculate multi-year GW momentum fluxes using a modified Hocking method (*Hocking*, 2005). As before, the year-to-year fluxes show similar patterns for each locations and can reach up to ±20m^2/s^2. Monthly mean fluxes reveal a seasonal cycle with more eastward fluxes around wintertime and more westward in the summer. There was also another semiannual oscillation observed in the meridional fluxes similar to other sites.

Airglow imagers may also be used to estimate GW momentum fluxes but instead of using an average over many waves they are able to give the flux of single wave events in the MLT region. For the night of November 19, 1999, *Suzuki et al.* (2007) used an OH airglow imager to estimate the fluxes of all observed wave events. The average flux in the zonal direction was 2.8m^2/s^2 and -3.0m^2/s^2 in the meridional. These were all smaller scale waves with periods of 10-25 minutes and horizontal wavelengths of 30-90 km.

Typically, other instruments such as meteor radars and LIDARs are used to support airglow imager measurements. The imager cannot observe some atmospheric properties such as density and is limited to a single altitude so these other observational techniques are used

in conjunction to form a complete picture of the GWs and their propagation background to more accurately estimate momentum fluxes. One such analysis was performed by *Espy et al.* (2004) with a Na airglow imager, a Na LIDAR and a Doppler interferometer radar wind instrument all located at Halley Station, Antarctica (75.6°S, 26.6°W). Here as with the other studies above, the monthly average momentum flux showed a seasonal dependence in both the zonal and meridional directions. In the winter months, the average zonal fluxes reached up to -6m^2/s^2 while in the summer they are around +6m^2/s^2. The seasonal variation is attributed to the seasonal dependence of the critical layer filtering in the stratosphere. Even with the wide swings in daily and monthly mean fluxes, the yearly average is relatively stable of around -4.5m^2/s^2 in the zonal direction and 0.6m^2/s^2 in the meridional.

With the background theory on the tides and GWs discussed, the interactions between these two vastly different scale atmospheric dynamics can be examined.

2.3 GW-Tidal Interactions

2.3.1 Introduction

As discussed in the previous sections, thermal tides are a global scale dynamical process forced by daily solar heating. Gravity waves, on the other hand, are local scale waves forced in the lower atmosphere by wind over orography, convection, or other tropospheric dynamics. The interaction between these small scale GWs and the large scale thermal tides is not well understood due to the variability and intermittency of GWs (*Liu et al.*, 2013; *Ortland and Alexander*, 2006). In this chapter a short review of some current theories and observations of the tidal affects on GWs and GW effects on the tides will be performed.

2.3.2 Tidal Modulation of Gravity Waves

While the main subject of this work is GW affects on the tides, there is also a reverse relationship where the tides act as a varying background for GW propagation. This will act to influence the magnitude of the GW momentum fluxes, the location of breaking and saturation altitudes among other properties. In turn this can affect how the GWs impact the tides creating a coupled system between these different dynamical processes.

A schematic representation of how the background wind with a tidal structure may influence the momentum flux of a GW passing through it is shown in Fig. 2.10 (*Fritts and Vincent*, 1987). The dashed line in both the a and b panels are an eastward propagating GW, the solid lines indicated by $\overline{u}$ are the zonal winds and are eastward in both panels a and b. The right plots represent the GW momentum flux of the wave in the left plots. The assumptions here are that the GW has become saturated below the altitudes shown in the figure and that the wave is monochromatic and linear as in the Lindzen GW theory (*Lindzen*, 1981). The wave motions are also assumed not to influence the wave environment. With these assumptions the wave motion amplitude is limited to:

$$u^{'} = \overline{u} - c, \tag{2.42}$$

where c is the GW phase speed. The GW momentum flux is found from:

$$\overline{u'w'} = -\frac{k}{2N}\left(\overline{u} - c\right)^3, \tag{2.43}$$

which means that the difference between the saturated GW phase speed and the mean winds is the largest influence on the momentum flux. For the eastward propagating GW ($\overline{u} > c$) in panel a, the decreasing zonal winds with altitude due to the tidal structure reduces the negative momentum flux while a westward propagating GW ($c > \overline{u}$) would experience an increase in positive flux. In panel b, the zonal wind structure increases with altitude
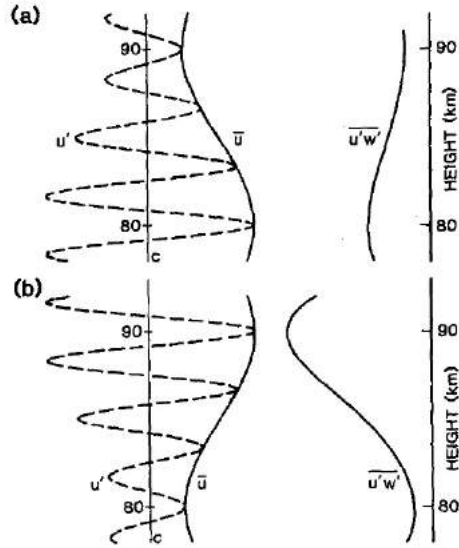
Figure 2.10: Schematic showing how the background tidal winds changes GW momentum flux (*Fritts and Vincent*, 1987).

which increases the difference between the mean wind speed and the eastward (westward) propagating GW phase speed leading to an increases (decrease) in the negative (positive) momentum flux. Above 90 km the winds again decrease sharply reducing the momentum fluxes.

Tidal affects on GW momentum fluxes have been frequently observed in many studies. *Beldon and Mitchell* (2010) used a meteor radar in Rothera Antarctica (68°S, 68°W) to measure GW momentum flux variations over three years from 2005 ro 2008. They found significant modulations of the observed GW field at periods of 12 hours in the summer and autumn months and 24 hour periods throughout the year which correlate to the diurnal and semidiurnal tides. They also discovered an in phase relationship between the hourly zonal winds and the GW variances in winter and antiphase in the summer months. This indicated that critical layer filtering plays an important role in the modulations by affecting the dominant GW propagation direction in the mesosphere.

Isler and Fritts (1996) also used a meteor radar to study the variance in GW momentum fluxes due to a variety of lower frequency wave motions (tidal, 2-day wave, planetary wave and mean winds) in the MLT region. The radar was stationed in Hawaii from October 1990 to

33

August 1992. When the diurnal tide was very strong the spectra of the GW variances showed significant modulation at both diurnal and semidiurnal periods. In addition, modulations also occurred due to the 2-day wave. The CRISTA satellite observing temperature profiles also detected modulation of GW activity by the migrating diurnal tide (*Preusse et al.*, 2001). It was concluded that the tides induced changes in the bouyancy frequency which then affected the propagating GWs.

2.3.3 Gravity Wave influences on the Tides

For the tides, a single breaking GW is unlikely to influence the tidal structure in any meaningful way; instead, many waves with a variety of scales are needed. How these much smaller waves can change the tides is a complicated issue due in part to the large scale differences between them. Figure 2.11 shows a schematic of how non-saturated breaking GWs may change the tidal amplitudes and vertical wavelengths (*Mayr et al.*, 1999). The thinner black line is the original tidal structure with the thicker line the tide after being affected by the GWs. The λ on the left side is the vertical wavelength of each tidal structure. According to this theory, the GWs will break and deposit their momentum in the direction of the background winds of which the tides are a major component. As discussed in the previous chapter, GWs will break when their intrinsic frequency is reduced to zero, otherwise the wave will pass through.

At the lower altitude near the third peak in the background winds, some GWs whose intrinsic frequency are shifted to zero will break and deposit their energy and momentum, causing the winds to accelerate towards the right. The tidal structure then changes the background wind direction above this altitude so that other GWs will not have their intrinsic frequency shifted enough and continue to propagate upward. The next maximum in the tidal winds is larger but towards the left. At this altitude, GWs propagating in this direction will begin to break accelerating the winds leftward but the tidal structure again reverses direction allowing GWs whose intrinsic frequency are still not zero to continue propagating.
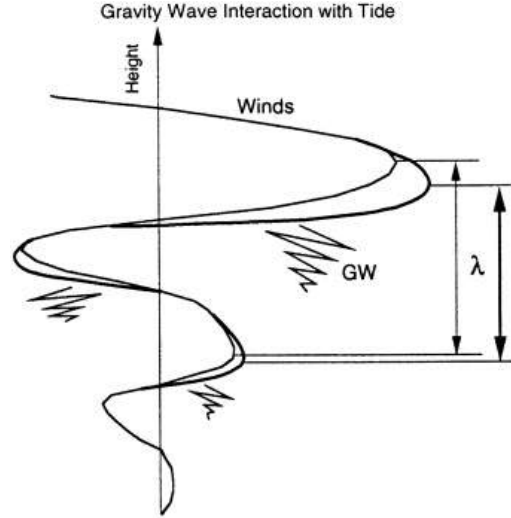
Figure 2.11: Schematic of GW-Tidal interactions showing how the tidal amplitude and vertical wavelength changes due to GWs (*Mayr et al.*, 1999).

The maxima in the tidal winds above this altitude is once again towards the right side but the wind speed is much larger. GWs which did not break at the lower, smaller peak in the winds may begin to deposit their momentum here. This causes another acceleration in the background wind direction. From the diagram, the acceleration of the winds creates new peaks in the tidal structure at lower altitudes from the non-GW affected winds effectively shortening the vertical wavelength of the tide. This also creates a delay in the phase of the tide at every altitude.

A nonlinear two-dimensional model that directly resolves GWs was used by *Liu et al.* (2008) to study the interactions between the diurnal tide and GWs. This model also found that GWs will increase the tidal amplitude while lowing the phase lines thus decreasing the vertical wavelength similar to the above explanation.

Another modeling study by *Ortland* (2005) showed that GW drag can affect the amplitude and phases structure of the migrating diurnal tide and its associated Hough modes. Instead of directly simulating the GWs, a complex damping coefficient was used to represent diffusion and GW forcing. Fig. 2.12 shows the dependence of the vertical wavenumber ($m = m_r + i * m_i$) of the (1,1), the (1,2) and the (1,3) Hough modes on the damping rates.
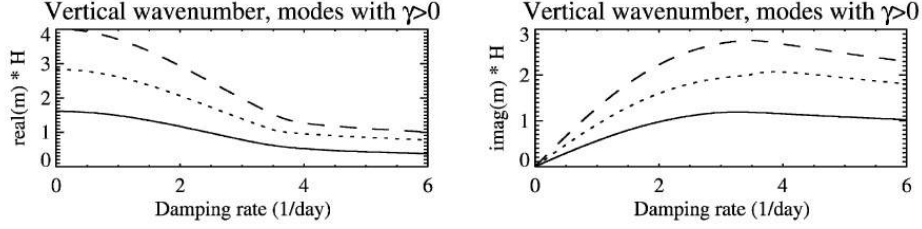
Figure 2.12: Affect of the damping rate on the real (left) and imaginary (right) components of the (1,1) mode (solid) the (1,2) (dotted) and the (1,3) (dashed) generalized Hough modes (*Ortland*, 2005).

The left plot is for the real component of the vertical wavenumber given by $m_r = 2 * \pi / \lambda$ with the right the imaginary component which gives the rate of decay of the vertical wavelength. With increased damping rates the vertical wavenumber decreases for all Hough modes corresponding to increases in the vertical wavelength. At the same time the vertical wavelength decay rates increase sharply before slowly decreasing. The exact damping rate to induce this turnover depends on the Hough mode. The difference between these results, where λ is increased, and the *Mayr et al.* (1999) explanation, where λ is decreased, is that the former did not consider GW diffusion which always leads to increased vertical tidal wavelengths and decreased tidal amplitudes.

An important property to consider when discussing GW-tide interactions is the phase difference between the two. When the phase difference is larger than 90° the GWs will tend to increase the tidal amplitudes and decrease the vertical wavelength as explained by *Mayr et al.* (1999). On the other hand, a smaller phase difference will lead to damping of the tidal amplitudes and an increase in the vertical wavelength as shown by *Ortland* (2005). The phase difference between the GWs and tides greatly depends on the source regions which is difficult to quantify as discussed in the previous chapter and GW dissipation mechanisms. Models must make many different assumptions resulting in large differences in GW affects on the tides between models.

Chapter 3

Observations of Gravity Wave - Tidal Interactions

3.1 LIDAR Observations

3.1.1 Introduction

Global circulation models are useful tools for understanding the underlying dynamical processes and interactions in the atmosphere by studying the entire structure of the dynamical features in both space and time. These models are built based upon not only the basic physics of the atmosphere but also on a multitude of observations that provide constraints, verifications and new knowledge. In this chapter, an observational analysis is performed to provide insights on the relationships between GWs and tides. Due to large differences in their temporal and spatial scales, long-term simultaneous observation of GWs and tides are not easy to obtain. There are many case studies of GWs interacting with a tidal feature (e.g. *Thayaparan et al.*, 1995; *Isler and Fritts*, 1996; *Nakamura et al.*, 1997; *She et al.*, 2004; *Williams et al.*, 2006). Due to the highly intermittent and local nature of GWs, the results of these studies vary depend on the property of waves and the local tidal perturbation. It is not clear which features occur more frequently and which features are special.

In this study, LIDAR measurements are used to address the long-term averaged effects of the gravity wave-tide interactions. Recently, *Liu et al.* (2013) used individual meteor trail wind detections from a meteor radar over Maui, Hawaii to derive the gravity wave momentum flux and their effects on the diurnal tide over a five-year period. While meteor radar can provide long-term observations, high counts of meteor detections within a short duration (1 to 2 hours, to resolve tidal variation) is needed to derive reliable momentum flux (*Vincent et al.*, 2010; *Fritts et al.*, 2012). Na Doppler LIDARs can measure wind at high spatial and temporal resolutions, making it ideal to derive the local time variation of momentum flux. On the other hand, it is very challenging to make long term 24-h continuous observations with a Na LIDAR as has been done by *She et al.* (2004).

In this work, high resolution Na LIDAR measurement of wind and temperature obtained at Starfire Optical Range (SOR, 35.0°N, 106.5°W), New Mexico from 1998 to 2000 is used to derive local time variations of gravity wave momentum flux and examine their relationship to variations of background wind associated with the diurnal tides. This LIDAR dataset was acquired at night only. Even though there is no continuous coverage, nights were selected when the diurnal tides were strong so the tidal components can be derived reliably. The goal is to examine the average gravity wave-tide relationship. A paper of this work was published in the Journal of Atmospheric and Solar-Terrestrial Physics (*Agner and Liu*, 2015).

3.1.2 Data and Method

The Na LIDAR wind and temperature observations used for this study were obtained at the Starfire Optical Range (SOR), located in the Kirkland Air Force Base near Albuquerque, NM. The LIDAR was pointed to five directions at zenith, and 10° off zenith at North, East, Zenith, South, and West in sequence, to measure line of sight wind, Na density and temperature in each direction with 90 sec integration time. The raw photon counts were accumulated at 24 m range resolution and the derived quantities have a range resolution of 480 m. The observations were made at night only, with a total of 51 nights data. Detailed

information about the instrument and data can be found in *Gardner and Liu* (2007).

For each night, the gravity wave perturbations are deduced by removing a linear trend in time within a two-hour sliding window in each of the five line of sight (LOS) observing directions in a similar way as *Acott et al.* (2011). This gives gravity wave perturbations with periods less than 2 hours, which include most significant GWs in this region (*Tang et al.*, 2002). The linear fit within the 2-hr window in the LOS directions is considered as the LOS background wind. The zonal and meridional components of the background wind are derived from the following equations,

$$
\begin{aligned}
V_Z &= w, \\
V_E &= u\sin(\theta) + w\cos(\theta), \\
V_W &= -u\sin(\theta) + w\cos(\theta), \\
V_N &= v\sin(\theta) + w\cos(\theta), \\
V_S &= -v\sin(\theta) + w\cos(\theta),
\end{aligned}
\tag{3.1}
$$

where V_Z, V_E, V_W, V_N and V_S are the LOS background winds from the linear fits, $\theta = 10°$ is the zenith angle, u and v are the zonal and meridional components of the horizontal background winds respectively, and w is the vertical wind.

Since the observations were made at night only, extracting the diurnal variation from the measurements may not be reliable, especially when the diurnal variations are weak or the semidiurnal variations are much stronger. To minimize the uncertainty due to weak tidal activity, only nights which exhibited strong diurnal tidal features were selected for the analysis so that the GW-tide interaction is more clear. The problem of extracting reliable tidal information at a particular altitude from only fractions of a day has been a long standing problem (*Crary and Forbes*, 1983). Here, the additional vertical structure afforded by the LIDAR is taken advantage of to constrain the tidal fits and derive more accurate information about each night. A similar approach was used by *Liu et al.* (2004). Selection of nights

with strong tidal features was performed with a two dimensional sinusoidal least-squares fit in time and altitude on the zonal and meridional background horizontal winds to extract the diurnal and semidiurnal amplitudes and phases. A linear combination of diurnal and semidiurnal sinusoids was used due to the relatively similar amplitudes of each tidal feature at the mid-latitudes (Li, 2009). An additional exponential growth factor was multiplied with each sinusoid to better represent the change in amplitude with altitude,

$$
\begin{aligned}
U_{fit}(z,t) = A + B * \sin(\frac{2\pi t}{24} + \frac{2\pi z}{C} + D) * e^{(E*z)} + ... \\
F * \sin(\frac{2\pi t}{12} + \frac{2\pi z}{G} + H) * e^{(I*z)},
\end{aligned}
\tag{3.2}
$$

where A is the mean, B is the diurnal amplitude, C is the diurnal vertical wavelength, D is the diurnal phase and E is the diurnal exponential growth factor. F though I are similar parameters but are for the semidiurnal component.

The selection of nights for the analysis involved setting limits on several fitted parameters. Nights which exhibited an r-square goodness of fit statistic greater than 0.3 were considered for the analysis. This limit was chosen based upon the balance between the number of nights passing this limit and a visual inspection of the quality of the fit. The diurnal tidal amplitude was required to be greater than 20m/s for the tide to be considered strong. Additionally, a night was required to have more than 10 scan profiles and more than 6 hours of data to be used. Due to differences in the number of profiles in the zonal and meridional directions on some nights, each direction was considered separately for the data binning and analysis.

An example of the two dimensional fit for October 27, 2000 is shown in Fig. 3.1. The wind data from the LIDAR for this night does not show a diurnal or semidiurnal tidal structure but a fit of the two dimensional combined diurnal and semidiurnal sinusoids represents the complex structure well. The diurnal amplitude for this night is 61m/s with a vertical wavelength of 22km while the semidiurnal amplitude is 42m/s with a vertical wavelength of 35km.

The selection process resulted in 23 nights in the zonal direction and 19 in the merid-
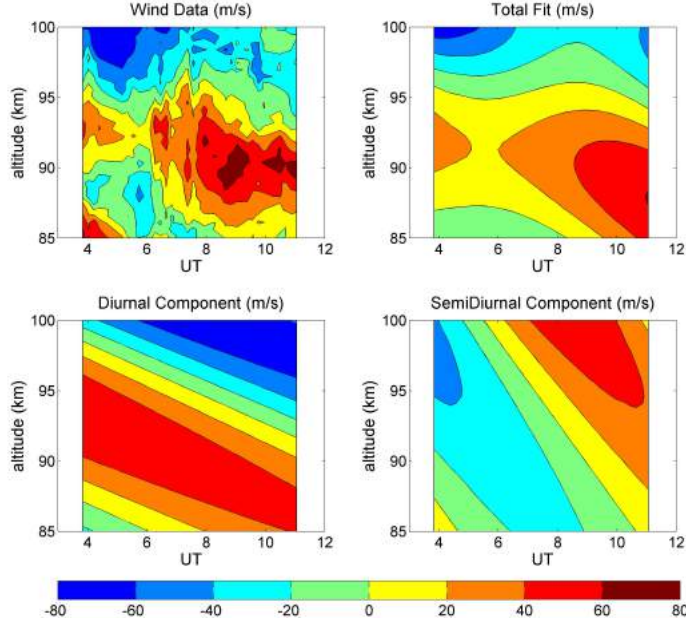
Figure 3.1: Example of the tidal fits on the zonal wind for the night of October 27 2000 in m/s. The top left plot is the raw wind data from the LIDAR, the top right plot is the total fit including both the diurnal and semidiurnal components, the bottom left plot is the diurnal component of the fit, and the bottom left plot is the semidiurnal component of the fit.

ional. The distribution of the nights through out the calendar months from 1998 to 2000 for the zonal direction is listed in Table 3.1 and for the meridional in Table 3.2. The nights roughly spreads out evenly for all calendar months in both directions, except in July when no observation was available. Only wind data is used in this analysis.

Table 3.1: Zonal Days exhibiting strong tidal features in each month

	Jan	Feb	Mar	Apr	May	Jun	Jul	Aug	Sep	Oct	Nov	Dec
1998	0	0	0	0	0	0	0	0	1	0	0	3
1999	2	1	0	1	3	0	0	1	0	2	1	1
2000	1	0	2	2	1	0	0	0	0	2	0	0

Table 3.2: Meridional Days exhibiting strong tidal features in each month

	Jan	Feb	Mar	Apr	May	Jun	Jul	Aug	Sep	Oct	Nov	Dec
1998	0	0	0	0	0	1	0	0	1	0	0	2
1999	1	1	0	0	2	0	0	1	1	1	1	1
2000	1	0	2	2	0	0	0	0	0	1	0	0

3.1.3 Background Wind, Momentum Flux and Gravity Wave Forcing

The next step is to calculate the composite momentum flux for a phase aligned composite night. The horizontal wind perturbations at the same tidal phase (not same local time) determined from the fit, were grouped together. This is because the tidal phase has daily and seasonal variabilities (*Lu et al.*, 2011), and this compositing method gives a proper relationship between gravity wave perturbations and the diurnal tide. The tidal phase at 90 km obtained from the tidal fit is used for this compositing process. Zonal and meridional wind perturbations are grouped based on diurnal tide phases of zonal and meridional wind, respectively. The vertical flux of horizontal momentum at every phase hour was then calculated with the dual-beam method (*Vincent and Reid*, 1983)

$$
\begin{aligned}
\overline{u'w'} &= \frac{\overline{V_E'^2} - \overline{V_W'^2}}{4\sin\theta\cos\theta}, \\
\overline{v'w'} &= \frac{\overline{V_N'^2} - \overline{V_S'^2}}{4\sin\theta\cos\theta},
\end{aligned}
\tag{3.3}
$$

where the primes denote wave perturbed quantities. The gravity wave forcing on the horizontal wind was calculated as the vertical convergence of momentum flux

$$
\begin{aligned}
U_{acc} &= -\frac{1}{\rho}\frac{d}{dz}\left(\overline{\rho u'w'}\right) = -\frac{d\overline{u'w'}}{dz} + \frac{\overline{u'w'}}{H}, \\
V_{acc} &= -\frac{1}{\rho}\frac{d}{dz}\left(\overline{\rho v'w'}\right) = -\frac{d\overline{v'w'}}{dz} + \frac{\overline{v'w'}}{H},
\end{aligned}
\tag{3.4}
$$

where H is the scale height of the atmospheric density, ρ, calculated using the average temperature at each altitude and phase hour. The composite diurnal phase aligned background wind, momentum flux and forcing were then fitted with a mean plus 24-hr sinusoidal function at each altitude to obtain their diurnal components.

The effects of gravity wave forcing on the amplitude and phase of the diurnal tide is quantified with the Equivalent Rayleigh Friction (ERF) calculated at each altitude. The ERF was introduced by *Forbes et al.* (1991) and were used in many studies of gravity wave forcing on the diurnal tides (e.g. *McLandress*, 2002; *Chang et al.*, 2011; *Lu et al.*, 2012; *Liu et al.*, 2013). The ERF is defined as

$$\gamma = -\frac{1}{\hat{u}}\frac{d\hat{u}}{dt} = -\frac{\hat{F}}{\hat{u}}, \tag{3.5}$$

where $\hat{u}$ is the complex amplitude of the tide and $d\hat{u}/dt = \hat{F}$ is the complex amplitude of the time tendency due to gravity wave forcing. γ is a complex quantity whose real part describes the change in amplitude of the tide and the imaginary part describes the change in phase due to the forcing. To calculate the ERF, the complex amplitudes $\hat{u} = u_0 e^{-i\phi}$ and $\hat{F} = F_0 e^{-i\psi}$ are obtained from the composite night fits, which gives the amplitudes u_0 and F_0 and phases ϕ and ψ of the tidal wind and gravity wave forcing, respectively.

The complex amplitude of the tide in (3.5) refers to the original tidal amplitude in the absence of gravity wave forcing. From the observation, only the tidal amplitude affected by the GWs can be measured. To compensate for this, γ was modified as follows (*Liu et al.*, 2013),

$$\gamma_{\mathrm{mod}} = \frac{\gamma}{1 - i\gamma/\omega}, \tag{3.6}$$

where $\omega = 2\pi/24$ hr is the angular frequency of the diurnal tide. Using this modified form of ERF the change in tidal amplitude due to GWs is then

$$\frac{du_0}{dt} = -u_0 \mathrm{Re}(\gamma_{\mathrm{mod}}), \tag{3.7}$$
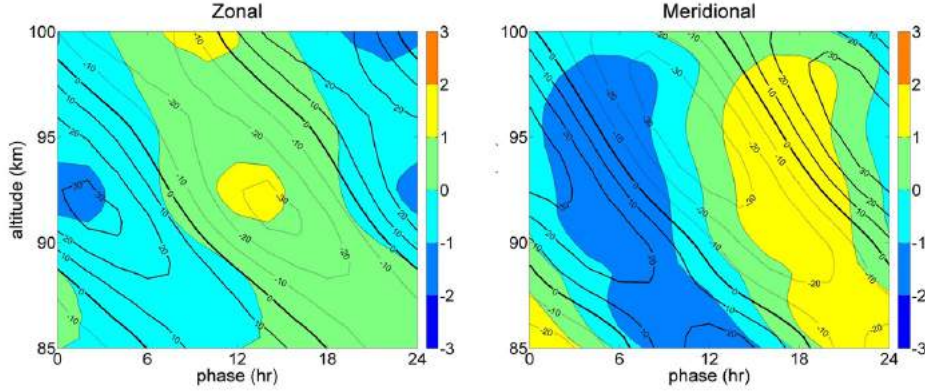
Figure 3.2: Diurnal variation of the background wind (contour, m/s) and gravity wave momentum flux (color, m^2/s^2)

and the change in tidal phase is

$$\frac{d\phi}{dt} = \mathrm{Im}(\gamma_{\mathrm{mod}}). \tag{3.8}$$

3.1.4 Results

The diurnal fits at each altitude of the phase aligned composite day momentum flux (colors) and the tidal winds (contours) are shown in Fig. 3.2. The momentum flux contours in both the zonal and meridional directions range from -3 to 3 m^2/s^2 with the tidal wind contours from -30 to 30 m/s. The zonal and meridional momentum fluxes shows a downward tilt below 90km matching the tidal wind, indicating some modulation by the diurnal tide. Above 90km, the diurnal component of the momentum flux is approximately constant in phase while the diurnal tide retains the downward tilt suggesting a weaker tidal modulation of the diurnal component of the momentum flux in the phase aligned composite day.

Fig. 3.3 shows the phase aligned composite day forcing due to GWs in both the zonal and meridional directions, again superimposed with the diurnal variation of the background wind. The magnitude of the diurnal component of the zonal forcing ranges from -20 to 20 m/s/day and is nearly double that in the meridional direction. The zonal direction shows the forcing to be out of phase between 88 and 98 km implying that the GWs change the amplitude of the diurnal tide at these altitudes with little change in the phase. The partial
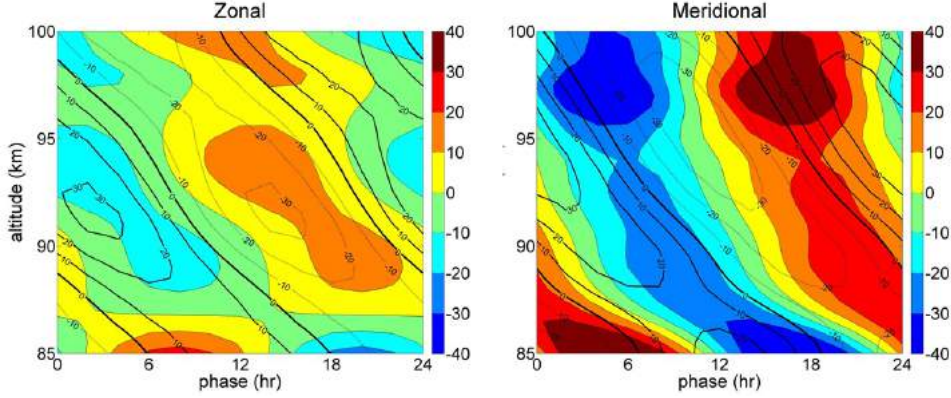
Figure 3.3: Diurnal variation of the background wind (contour, m/s) and the gravity wave forcing (color, m/s/day)

offsets above and below imply a greater effect on the tidal phase. In the meridional direction, the forcing is out of phase below 90 km with an approximately 90° offset above.

The change in phase with altitude for the tidal wind, the momentum flux and the gravity wave forcing is shown in Fig. 3.4 with the left plot showing the zonal phases and the center plot the meridional phases. The error bars are derived from the propagated error for each term. The relative phase difference, defined as the forcing phase minus the tidal phase, is shown in the right plot in Fig. 3.4 for the zonal and meridional directions with the green shaded indicating the areas between 6 hrs and 18 hrs phase difference. The relative phase difference between the zonal tidal wind and the zonal GW forcing at SOR is roughly 12 hours between 88 km and 97 km (within the shaded region)and less above and below. In the meridional direction, the relative phase difference between the GW forcing and the tidal wind is of similar magnitude to the zonal direction and is inside the shaded region below 95 km and outside above.

Fig. 3.5 shows the rates of change of the diurnal tidal amplitude and phase due to GWs forcing calculated from the ERF (equations: (3.7) and (3.8)) with the associated error bars again derived from propagated errors. The rate of change of the diurnal tide amplitude in the zonal direction has large variations with the forcing acting to damp the tide between 87 km and 97 km and enhance it otherwise ranging from -20 to 20 m/s/day. In the meridional
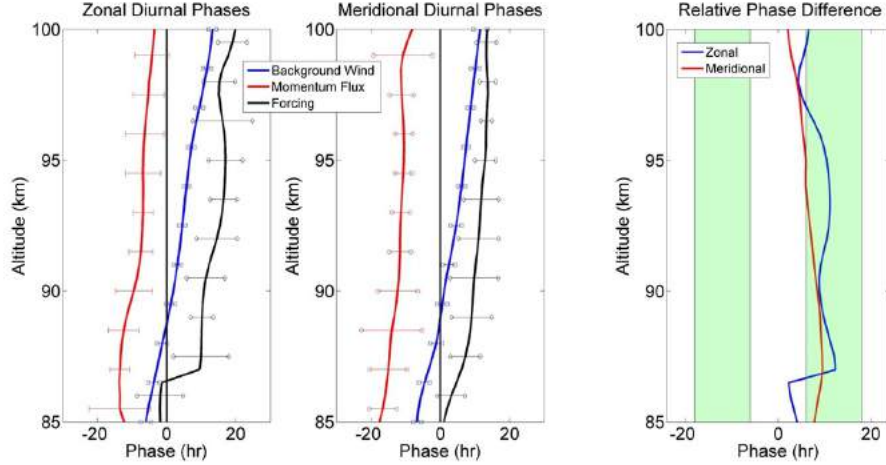
Figure 3.4: The left two plots are the phase variation with altitude for the background wind (blue), momentum flux (red) and gravity wave forcing (black) in the zonal (left) and meridional (center) directions. The right plot is the phase difference with altitude between the wind and the forcing in the zonal and meridional directions. The shading represents areas where the phase difference is between 6 and 18 hours.

direction, the GW forcing damps the meridional component of the tide below 93 km and enhancing it above. The magnitude of the change in meridional tidal amplitude reaches maximums in the upper and lower altitudes that is nearly double that of the zonal direction but the larger error bars make it possible that the magnitude of the amplitude change is similar to the zonal direction.

A remarkably similar altitude dependence of the zonal tide amplitude rate of change is reflected at solstice conditions from the DW1 projection of GWs in the *Watanabe and Miyahara* (2009) GCM study. This model did not use a gravity wave parameterization scheme but instead directly resolved larger scale GWs. At equinox conditions the DW1 projection of GWs would always enhance the DW1 tidal amplitudes in the model. Only GWs with period less than 2 hours are considered here for the composite day using local diurnal variations which may include other diurnal modes. This suggests that locally, small scales waves can have similar effects on the diurnal tidal variations as large scale DW1 projections of GWs do on the DW1 component.

The gravity wave forcing also acts to delay the zonal and meridional tidal phase at all

46
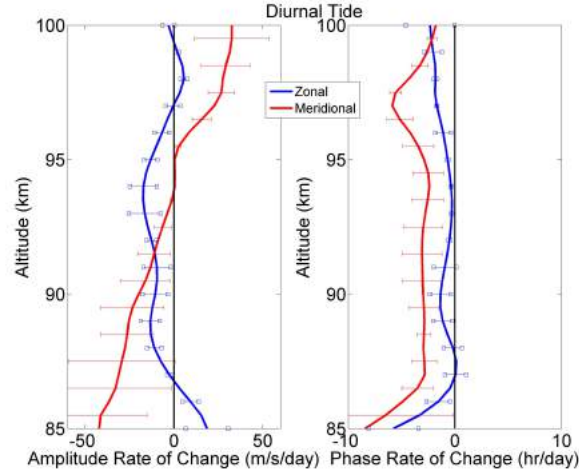
Figure 3.5: The altitudinal dependence of the rate of change of the diurnal amplitude and phase due to GWs

altitudes, pulling the phase lines down and shortening its local vertical wavelength. The magnitude of the phase change is similar at all altitudes except near 86 km and 97 km. This is consistent with the Lindzen and Hines parameterization schemes but is very different from the *Liu et al.* (2013) observations which showed an increase in the phase of the diurnal tide at most altitudes. The *Watanabe and Miyahara* (2009) GCM shows the zonal phase of the tide delayed at all altitudes as consistent with the parameterization schemes and the current observations.

3.1.5 Discussion and Conclusion

The relationship between high frequency GWs and the diurnal tide has been analyzed from two years of Na LIDAR observation at SOR. The diurnal component of the gravity wave momentum flux shows strong modulation by the diurnal tide in the zonal and meridional directions. The amplitude of the diurnal tide is either damped or amplified by GWs depending on the altitude. *Ortland and Alexander* (2006) used a mechanistic tidal model with a gravity wave parameterization scheme to show that the change in diurnal tidal amplitude depends on the phase difference between the gravity wave forcing and the tidal winds. When the gravity wave forcing is more than 90° out of phase with the tide it will act to

increase the tidal amplitude, when the forcing is less than 90° out of phase with the tide, the tidal amplitude will be decreased. This behavior can be seen in the current results when comparing the relative phase differences with altitude in Fig. 3.4 with the tidal amplitude change in Fig. 3.5.

The phase of the zonal diurnal tide at SOR is delayed leading to a local shortening of the vertical tidal wavelength consistent with previous model results. *Ortland and Alexander* (2006) also showed that the phase of GW forcing always leads that of the tide, resulting in a positive phase difference in agreement with our results.

Using the TIMED satellite, *Lieberman et al.* (2010) estimated the effects of GWs on the migrating diurnal tide in the 80 to 100 km region by estimating a residual from the momentum equations after subtracting the other large scale terms from the measurements. The residual from the zonal momentum equation was found to lead the zonal wind by 90° while the residual from the meridional equation was 180° out of phase. This is similar to our current results with the phase difference in the meridional direction generally greater than the zonal and the gravity wave forcing leading the diurnal wind.

Ortland and Alexander (2006) also showed the gravity wave forcing leading the wind in their model results.The magnitude of the phase difference was highly dependent on the gravity wave source spectrum which can effect the gravity wave breaking altitudes and subsequently, the tidal forcing dependence on altitude. Gravity wave parameterization schemes are typically tuned to match observed zonal mean winds. Each scheme makes different assumptions about gravity wave filtering and breaking processes. Comparisons between observational data and model results with different schemes can help tune the model source spectra to produce tidal amplitudes that are consistent with observations.

The issue of the discrepancy in the gravity wave tidal interactions between parameterization schemes is a complex problem due to the altitudinal and directional dependence of the interactions. Further observational studies from other sites are needed to acquire a more complete understanding . The gravity wave effects on the semidiurnal tide was also analyzed

but no significant relation was found. This could be due to a weaker semidiurnal signature in the available nights of data or larger uncertainties.

3.2 Meteor Radar Observations

3.2.1 Introduction

The second set of observational data used to study the gravity wave tidal interactions is from the Andes LIDAR Observatory (ALO) locates at Cerro Pachn, Chile (30°S, 70°W). There are several instruments located at this site including another Na LIDAR, an all sky imager and a meteor radar. The LIDAR at this facility began observations in mid 2014 but the beam steering was not functional at the time so horizontal winds were not available. The LIDAR was later upgraded and horizontal wind observations were available in early 2015 with several one to two week campaigns performed. There was not enough observations available at the time of this writing to perform an analysis similar to the SOR data in the previous section.

The meteor radar at this location has observational data ranging from September 2009 to August 2014 as summarized in Table 3.3 with a total of 1460 days of operation. While a smaller number of observations are required to calculate the mean winds with meteor radars, gravity wave momentum flux estimates require significantly more meteor detections. According to a simulation study by *Vincent et al.* (2010), only about 10 meteor per hour are needed to estimate the mean hourly winds but observations in excess of a month are required to obtain gravity wave momentum flux with reasonable accuracy. The large number of observational days here are far greater than this and should provide low uncertainties for the calculated momentum fluxes.

Another advantage of performing the analysis using the meteor radar is that the results can be directly compared to a similar study by *Liu et al.* (2013) which used the same meteor radar when it was stationed in Maui Hawaii along with the previous SOR LIDAR results.

This provides two major points of comparison. First, the GW-Tide interactions at different locations can be examined since the meteor radars at both ALO and Maui are the same instrument and a similar analysis method will be used. Second, any instrument bias on the GW-Tide interactions can be deduced. A meteor radar observes the entire sky and averages both the winds and GWs across it above the instrument. A LIDAR on the other hand observes a smaller section of the sky and is capable of detecting individual GWs. How this changes the results is an important question in future observational studies of this issue.

Table 3.3: Number of meteor radar observations at the ALO

	Jan	Feb	Mar	Apr	May	Jun	Jul	Aug	Sep	Oct	Nov	Dec
2009	0	0	0	0	0	0	0	0	16	31	30	13
2010	17	19	29	30	31	30	27	28	30	14	30	31
2011	31	27	28	26	30	19	27	15	27	28	26	0
2012	16	22	31	28	31	30	31	31	30	31	29	30
2013	21	28	31	26	31	20	20	31	30	31	14	31
2014	31	28	21	0	1	0	9	24	0	0	0	0
Total	116	124	140	110	124	99	114	129	133	137	129	105

3.2.2 Data and Method

The meteor radar currently stationed at the ALO was previously located in Maui Hawaii between 2002 and 2007. It is a SKiYMET radar (*Hocking et al.*, 2001) operating at 40.92 MHz. A single transmitter antenna is used to send out radio pulses with an average power of 170W These pulses are then reflected back to the ground from any meteors entering the upper atmosphere. An array of five receiver antennas on the ground detect the radar echoes. The receivers are oriented with four of the antennas in a cross pattern and the fifth one directly in the center of the cross. One set of receivers are 1.5 wavelengths from the center with the other two being 2 wavelengths away. Radar returns are sampled every 13.3 μs (*Franke et al.*, 2005). For each detected meteor trail, its position in the sky by a zenith and azimuth angle, its dopplar shift (used to calculate wind speeds) and its range are recorded. The mean zonal, u, and meridional, v, winds are estimated with a fit which minimizes the

weighted residual,

$$\chi^2 = \sum_i \frac{v_r{}^i - u\sin(\theta^i)\cos(\phi^i) - v\sin(\theta^i)\sin(\phi^i)}{\sigma^i}, \tag{3.9}$$

where $v_r{}^i$ is the line of sight velocity for the ith meteor, θ^i is its zenith angle and ϕ^i its azimuth angle. The σ^i term is a weighting function for each meteor that depends on the RMS uncertainties in distance and zenith angle. To calculate the mean winds the function is minimized using all meteor detections within a vertical and time bin. The mean winds are typically calculated every hour at a 1 km vertical resolution from 80 km to 100 km. For each meteor detection, the difference from the mean wind is calculated and stored along with the detection angles and height.

In a similar manner as the LIDAR analysis in Section 3.1 the winds and perturbations from the mean will be composited into a single diurnal phase aligned day using all available data to account for the day-to-day change in diurnal phase. Due to the orientation of the radar antennas, the detections are more sensitive in the North-South direction than the East-West directions. Fig. 3.6 shows the azimuthal distribution of all meteor detections at ALO from September 2009 to May 2015. Due to the increased sensitivity in the meridional direction, the phase of the meridional component of the tide will be used as the reference tidal phase.

The reference tidal phase for a day is calculated at 90km with a five day window around the day of interest. The phase is found by performing a least squares sinusoidal fit on the mean meridional winds. After the reference phase for the day is found the day is split into 12 bins each two hours wide. Each time bin is assigned a phase bin based on the phase of that days diurnal tide. The mean zonal and meridional winds, each meteors wind perturbations and their detection angles and heights are binned into the appropriate composite day phase bin. The mean winds in each phase and altitude bin are averaged to create the composite days background winds.

To calculate the gravity wave momentum flux, the Hocking method from *Hocking* (2005)
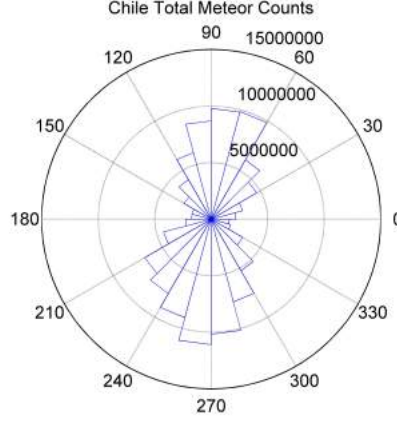
Figure 3.6: Azimuthal distribution of all meteor detections from September 2009 to May 2015 in 15° increments

is used. First it is assumed that the deviation of each meteor trails horizontal wind estimate from the mean winds are due to GWs. In this method the function,

$$\Delta = \sum ((v'_{rad})^2 - (v'_{radm})^2)^2, \tag{3.10}$$

is minimized where the sum is over all meteor detections within a bin. The quantity v'_{rad} is the difference between the radial velocity of the mean winds, v_{rad}, at a detection location and the measured radial velocity, v_{radm}. The second term on the right side of the equation, v'_{radm}, is the radial velocity pertubations from the mean winds defined as

$$v'_{radm} = u' \sin(\theta) \cos(\phi) + v' \sin(\theta) \cos(\phi) + w' \cos(\theta), \tag{3.11}$$

where u' is the zonal perturbation from the mean zonal wind, v' is the meridional perturbation from the mean meridional wind and w' is the vertical perturbation from the mean vertical

wind and is zero for this analysis. Expanding equation (3.10) yields

$$\Delta = \sum [(v'_{rad})^2 - (u'^2 \sin^2(\theta) \cos^2(\phi) + v'^2 \sin^2(\theta) \sin^2(\phi) + ...$$

$$w'^2 \cos^2(\theta) + 2u'v' \sin^2(\theta) \cos(\phi) \sin(\phi) + 2u'w' \sin(\theta) \cos(\theta) \cos(\phi) + ... \qquad (3.12)$$

$$2v'w' \sin(\theta) \cos(\theta) \sin(\phi))]^2,$$

This equation can then differentiated with respect to the u'^2, v'^2, w'^2, $u'v'$, $u'w'$ and $v'w'$ to obtain a set of six equations which can be solved for the six parameters. The quantities of greatest interest here are $u'w'$ and $v'w'$ which are the vertical momentum fluxes in the zonal and meridional directions respectively. Since the perturbations from the mean winds are assumed to be due to GWs, these are the gravity wave momentum fluxes.

For this analysis a vertical bin size of 3 km that is slid every 0.5 km at every phase bin is used to calculate the GW momentum fluxes. Not every meteor detection is used due to some larger errors that may skew the results. To effectively filter out atmospheric dynamics which may not be from GWs, only meteor trail detections with estimated horizontal wind velocities less than 30m/s will be included. In addition, any meteor detections with horizontal velocity errors less than 2m/s are used. To avoid further measurement errors from the instrument, only meteors with a zenith angle between 15° and 50° are considered.

The momentum flux is then smoothed with a 4 km sliding hamming window to bring out the large scale effects of GWs on the diurnal tide. The forcing due to GWs is calculated from the momentum flux as before with the LIDAR analysis. The forcing is also smoothed but with a 8 km hamming window. The remaining analysis is the same as before with a diurnal fit at every altitude, the calculation of the modified ERF and subsequently the rate of change of the diurnal amplitude and phase due to GW forcing.
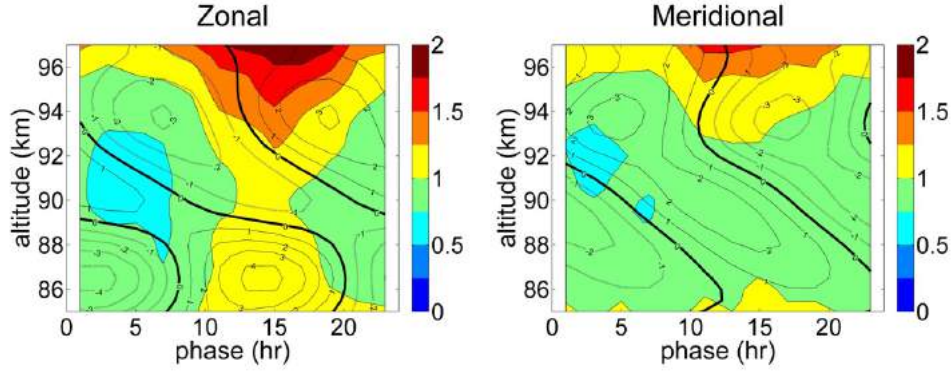
Figure 3.7: The diurnal component of the gravity wave momentum flux (contours, m^2/s^2) and the uncertainties (colors, m^2/s^2) in the zonal (Left) and meridional (Right) directions.

3.2.3 ALO Results

To begin, the diurnal component of the gravity wave momentum flux (contours) and the non-diurnal momentum flux uncertainties are shown in Fig. 3.7. The uncertainties were calculated with a bootstrap method which repeats the momentum flux calculation described in the previous section a specified number of times (100 times here) using a random sampling of horizontal wind detections. The standard deviation of the resultant momentum fluxes give the estimate of the uncertainty. From the figures, the uncertainty in the zonal direction is higher in the middle part of the altitude range than in the meridional direction. This is most likely because the data was binned according to the phase of the meridional component of the diurnal variations. While the phase in the zonal and meridional directions should be similar, other dynamical features may phase shift one component more than other resulting in a misalignment between the components. While the uncertainties are higher in certain sections, they are still reasonably small for most of the altitude range only reaching up to about $1.1 m^2/s/day$ around 90 km. The higher and lower altitudes also have larger uncertainties due to the fewer number of meteor detections and their higher errors. The maximum diurnal component of the momentum flux is around $3 m^2/s/day$ in both directions with uncertainties mostly around $0.8 m^2/s/day$.

Fig. 3.8 shows the diurnal component of the gravity wave momentum flux in colors and

54
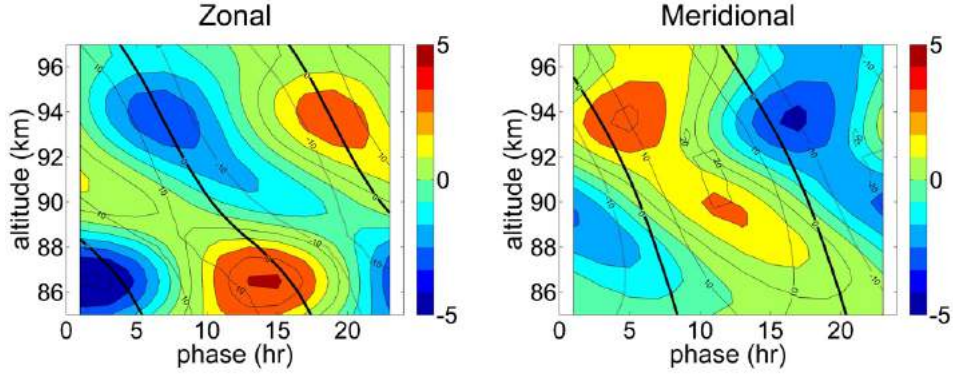
Figure 3.8: The diurnal component of the gravity wave momentum flux (colors, m^2/s^2) and wind (contours, m/s) in the zonal (Left) and meridional (Right) directions.

the diurnal component of the background winds in the contours in the zonal and meridional directions. In the zonal direction, the momentum flux has a 180° phase shift at 90 km. The phase of the tidal winds change slowly with altitude and do not have any sudden shifts. In general the tidal winds and the gravity wave momentum flux are 90° out of phase at most altitudes. In the meridional direction there is not a large phase shift in the momentum flux as in the zonal direction with the tidal winds acting in a similar manner. In both directions, the momentum flux due to GWs shows a downward tilt at some altitudes but not at others. A downward tilt similar to the tidal winds would indicate modulation by the tides on the GWs. This is shown above 90 km in the zonal direction and below 92 km in the meridional with more constant phase at the other altitudes. The difference between directions may be due to higher errors in the zonal direction at some phase bins as discussed above. The lower altitudes in the meridional direction are more reliable due to the lower uncertainties and this area shows clear tidal modulation of the GW momentum flux. Since this is from a 5-year composite day the modulation must be a consistant feature at this location.

The diurnal component of the GW forcing is shown in colored contours in Fig. 3.9 with the diurnal component of the winds in contours in both the zonal and meridional directions. The magnitude of the forcings range from -70 to 70m/s/day in the zonal direction and from -60 to 60m/s/day in the meridional. In the zonal direction, the forcing is 90° out of phase
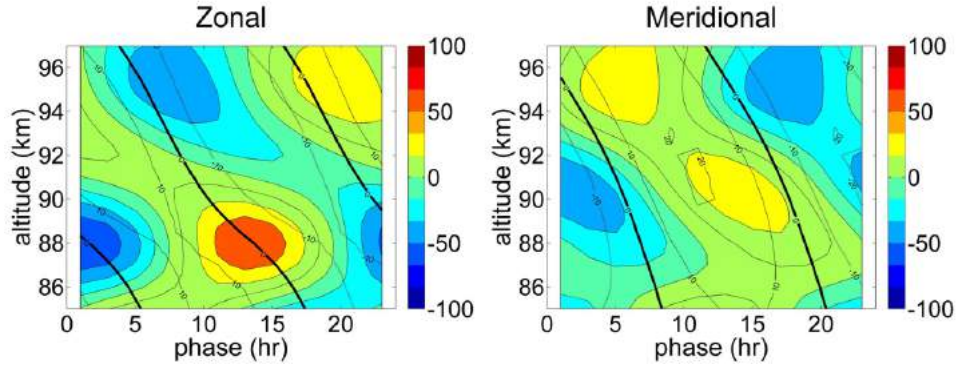
Figure 3.9: The diurnal component of the gravity wave forcing (colors, m/s/day) and wind (contours, m/s) in the zonal (Left) and meridional (Right) directions.

with the wind below 91 km and nearly in phase above. In the meridional direction the forcing is almost always in phase with the winds.

The rates of change of the diurnal tidal winds amplitude and phase in the zonal and meridional directions is shown in Fig. 3.10. The horizontal bars every kilometer are the error bars calculated from the propagated errors and the confidence intervals from the fits. The errors are small enough at most altitudes to give assurance of the sign of the rate of change. The higher altitudes have the largest uncertainties due to the decreased number of meteors and some larger errors especially in the zonal direction due to the binning being performed based on the meridional tide. The GWs over ALO are shown to almost always increase the amplitude of the diurnal variations in both directions with a small amount of damping of the zonal component around 90 km. The magnitude of the amplitude rate of change ranges from nearly zero to around 50m/s/day. The phase of the tidal variations are mostly increased below 93 km and is both increased and decreased above. To put these results into a larger context, the next section will perform a comparative analysis between these ALO results, the previous SOR results and other work from Maui, Hawaii.

Figure 3.10: The altitudinal dependence of the rate of change of the diurnal amplitude and phase due to GWs

3.2.4   Location and Instrument Comparisons

The interaction between GWs and tides is a difficult subject due to the large spacial and temporal differences between the waves. Observations are an important tool for better understanding these interactions but there must be some consideration for the different scales and dynamical features that each type of instrument observes. This comparative analysis will use observations from a meteor radar at the Andes LIDAR Observatory at -30° latitude, the same meteor radar when it was stationed at Maui, Hawaii at +20° latitude and the LIDAR at the Starfire Optical Range at +30° latitude.

First, the results from Maui and ALO will be analyzed since both the analysis method and the instrument itself are the same. Fig. 3.11 shows the results from *Liu et al.* (2013) which also constructed a 5-year diurnal phase aligned composite day to study how GWs affect the tidal amplitudes and phases. The amplitude of the zonal component of the diurnal variations was mostly enhanced by the GWs with a small 5 km region being damped. The

meridional component was damped below 90 km and enhanced above. The amplitude rates of change range from -20m/s/day up to 80m/s/day. Similar vertical structures in these rate curves are seen at ALO. The zonal component is positive at lower altitudes, becomes negative in a small region the becomes positive again rapidly growing larger. The meridional direction on the other hand shows some differences at the lower altitudes with the amplitude rate at ALO always being positive while at Maui it switches from being negative to positive with increasing altitude. The magnitude of the rates of change are also much smaller at ALO compared to Maui. The rate of change of the diurnal phases show larger differences between the sites. At Maui, the phase in both directions is almost always increased whereas at ALO, the phases are generally increased below 92 km and mixed above.

Even though the same instrument and analysis method was used at both sites some differences are expected due to the different latitudes, surrounding orography and average weather conditions. While there are some in the magnitude of the amplitude rates of change, the vertical structures are very similar especially in the zonal direction. This implies that on average, GWs have a consistent effect on the amplitude of the diurnal variations even when the locations are quite different.

On the other hand, the rates of change of the diurnal phases show many differences especially at higher altitudes. This indicates that the relative phase difference between GWs and the diurnal variations are not the same at these locations. The ALO is surrounded by the Andes mountains chain and the South American land mass compared to Maui which is surrounded by the Pacific ocean with a few high mountains from the Hawaiian islands. The convective and frontal GW sources can also be quite different at each location. These different source regions can provide large differences in the phase of GWs when launched. As a result, the average phase of the GWs which affect the tides could explain the discrepancies.

To study how different instruments observe the interactions between the GWs and tides the results from the SOR LIDAR and the meteor radar at ALO and Maui which will be compared. The rates of change of the diurnal amplitude and phases calculated from the
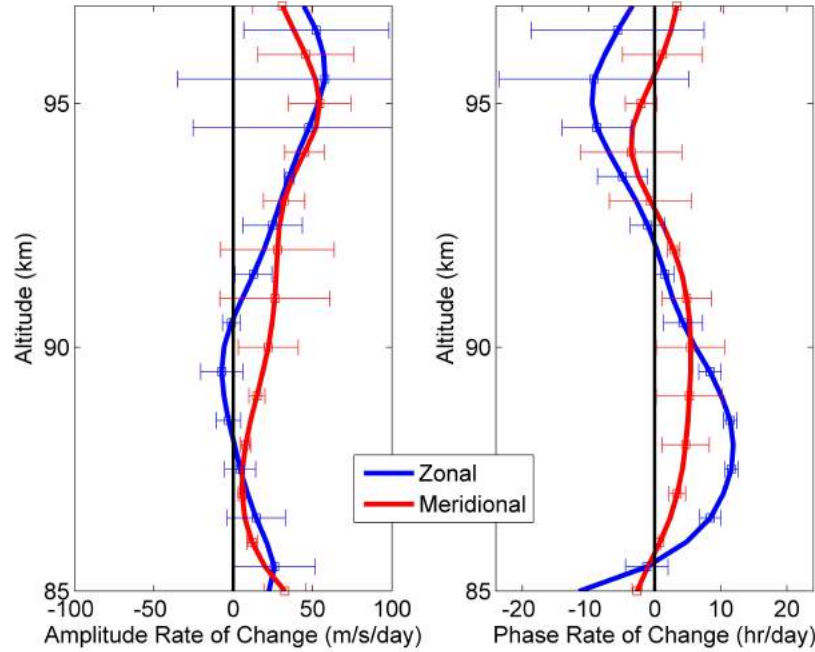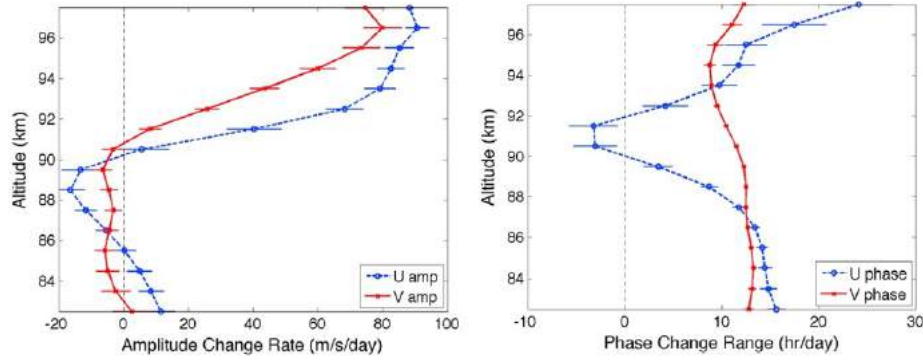
Figure 3.11: The altitudinal dependence of the rate of change of the diurnal amplitude and phase due to GWs using the meteor radar at Maui *Liu et al.* (2013).

SOR LIDAR data is shown in Fig. 3.5 while the same is also shown in Fig. 3.10 for the ALO meteor radar. In the zonal direction at SOR, the GWs dampen the tidal amplitude for most of the altitude range except near the top and bottom where it is enhanced. This is completely opposite in what the meteor radar at ALO and Maui found. In the meridional direction, the tidal amplitude is dampened below 95 km and enhanced above at SOR and Maui whereas it is always enhanced at ALO. The SOR rate of change of the diurnal amplitude is more similar to the Maui results than at ALO. For the change of phase with altitude, the LIDAR at SOR found that the GWs always decrease the tidal phase. At ALO, it is both increased and decreased but the meteor radar at Maui found that it was mostly increased.

A major point of difference between the results from the instruments is magnitude of the calculated GW momentum fluxes and the GW forcing. The momentum fluxes from the SOR LIDAR are $\pm 3 \mathrm{m}^2/\mathrm{s}^2$ while it is $\pm 5 \mathrm{m}^2/\mathrm{s}^2$ in the ALO radar results. Similarly, the LIDAR shows GW forcing to be $\pm 40 \mathrm{m/s/day}$ while the radar estimates up to $\pm 100 \mathrm{m/s/day}$. A possible reason for the large inconsistency is the observation times of each instrument. The LIDAR is only able to operate at night while the meteor radar can detect meteor trails 24 hours a day. For a more direct comparison between the instruments the same analysis method described for the ALO radar observations is applied again but instead only using meteors detected during the night hours defined as between 5 and 16 UT for the ALO
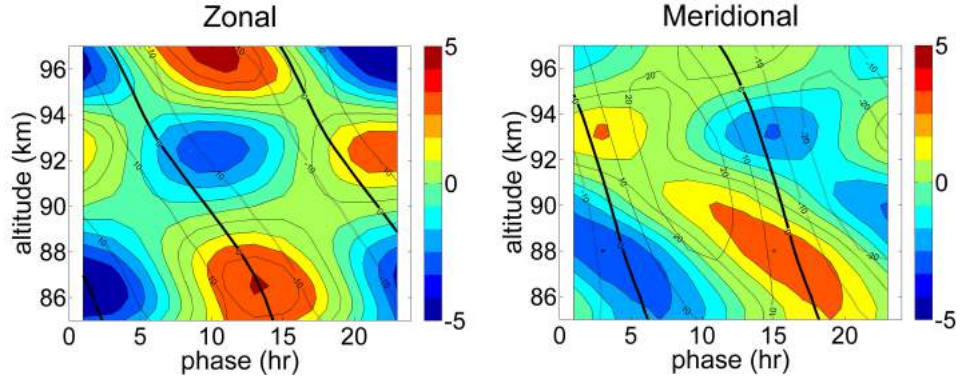
Figure 3.12: The diurnal component of the gravity wave momentum flux (colors, m^2/s^2) and wind (contours, m/s) in the zonal (Left) and meridional (Right) directions only using meteors detected at night.
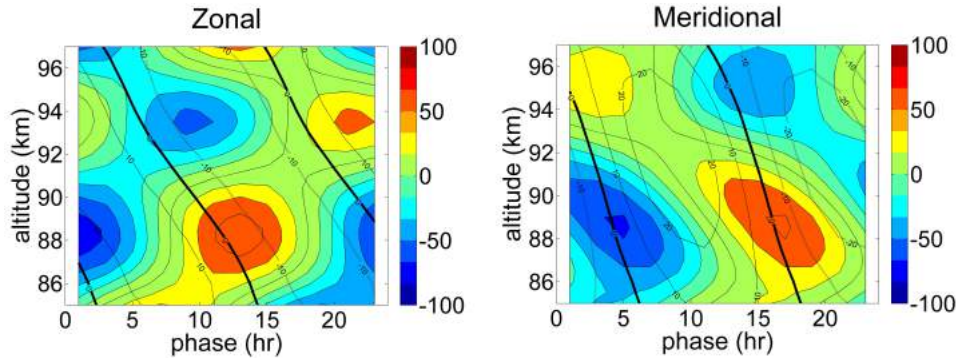
Figure 3.13: The diurnal component of the gravity wave forcing (colors, m^2/s^2) and wind (contours, m/s) in the zonal (Left) and meridional (Right) directions only using meteors detected at night.

site. Fig. 3.12 shows the diurnal wind and GW momentum flux results in the zonal and meridional directions for a single composite day using nightly meteor detections. The results are very similar to the previous estimates using 24 hour detections in terms of magnitudes but the structure of the diurnal variations is different above 90 km. This is due to the fewer number of detections leading to larger errors in the momentum flux estimates. The meridional direction is also more similar than the zonal due to smaller error bars because of the previously discussed bias in meteor detection direction.

Fig. 3.13 shows the diurnal component of the wind and GW forcing using nighttime meteor detections. Like the diurnal GW momentum fluxes, the nighttime GW forcing have very similar magnitudes to the all day forcings with some structural differences due to the

larger error bars. Since the nightly GW fluxes and forcings are similar in magnitude to the all day estimates, the differences between the LIDAR and meteor radar results are not due to any differences in the daily variations of gravity wave activity.

To understand why these results can be so different even when both instruments only consider nightly data, it is useful to compare how each instrument operates and what they are observing. A meteor radar detects incoming meteors and the trails that they leave behind. They do not enter the atmosphere uniformly and are very intermittent in both time and space. When they do enter the atmosphere the altitude at which a meteor burns up and leaves a trail depends on the size of the meteor and the atmospheric density which is also not uniform. Larger meteors are able to penetrate deeper than smaller ones. The trails from the meteors are detectable for some time after it is dissipated and the doppler shifting of the trail is used to estimate the instantaneous winds at the detection locations. One of the challenges with this instrument is that there no way to control the rate at which meteors enter the atmosphere or where they dissipate. In addition, the instantaneous wind at a meteor detection may contain a summation of any number of dynamical features such as GWs, tides, planetary waves, or turbulence that may skew the wind velocities. As a result, only the mean winds can be reliably calculated by performing an all sky fit using all detections within relatively large time and altitude bins.

A LIDAR operates in a very different manner observing a much smaller section of the sky. A LIDAR first fires a high powered laser pulse at a specific frequency into the atmosphere. The SOR LIDAR is set to the resonance frequency of sodium (Na). When the laser encounters a Na atom, some of the energy is absorbed by the atom and the electrons are put in an excited state. After a spontaneous amount of time the atom relaxes and the energy is emitted into the atmosphere from the atom in a random direction. Some of the reemitted energy is directed back towards the LIDAR facility where it is observed with a telescope. The dopplar shifting of the reemitted photons as well as the intensity give estimates of the sodium density and the wind velocities. Unlike the meteor radar, the time and location of

the observations are controlled from the instrument. The LIDAR estimates the winds at a specific location in the upper atmosphere with a relatively high time cadence of a couple of minutes. The major challenge for this type of instrument is that it is difficult to operate for long periods of time due to its complexity and it only observes a single location or small section of the sky if the laser is turnable. When observing a smaller area it may be difficult to distinguish large scale features since they may blend with each other. Smaller scale features in an area adjacent to the observations could also alter the winds in unexpected ways.

In summary, the meteor radar uses an all sky average to calculate the winds while the LIDAR directly observes a small section of the sky. For these gravity wave momentum flux calculations, the meteor radar uses all perturbations from the mean across the entire sky over five years to find an average flux. In contrast the LIDAR calculates perturbations on specific days from individual GWs and uses the average to find the mean momentum flux within the observation area.

In the zonal direction when including all perturbations from the mean and a large amount of averaging from the meteor radar the GWs tend to increases the tidal amplitudes except around 90 km. The phase is either increased or decreased depending on the location and altitude. When only short period waves are considered in a small section of the sky using a much smaller time average from the LIDAR the waves tend to dampen the tidal amplitude and decrease its phase. For the meridional component, the tidal amplitude is either enhanced or damped below 90 km depending on the location and is enhanced above in the radar observations. The tidal phase is generally increased. On the other hand the tidal amplitude and phase are both decreased when only short period waves are considered when using the LIDAR at SOR.

Franke et al. (2005) found that the instrument bias shown here in the gravity wave interactions with the tides are not present when observing only the background winds. This comparison study used the meteor radar in Maui and a Na LIDAR to simultaneously observe the horizontal winds in July 2002 October 2003 and November 2003. The two data sets

were directly compared by binning both observations into 1 hour, 4 km bins. There were no statistically significant differences found between the observations. The calculated horizontal winds were not exactly equal and any differences were found to be from the observable wave scales for each instrument. The meteor radar cannot resolve wave scales smaller than around 200 km while the LIDAR is sensitive to most horizontal scales.

Since the calculated winds from each instrument do not show a bias, any difference in the GW effects on the tide must be due to the calculated momentum fluxes which is related to the resolvable wave scales and the amount of averaging performed. The differences in diurnal amplitude rates between the LIDAR and the meteor radar implies that the mean GWs effects from larger wave scales in the the meteor radar analysis tend to enhance the local tidal amplitude while only smaller scale waves from the LIDAR act to dampen it. The change in phase is dependent on the location of the observations which may be due to the average phase of the gravity wave sources.

3.2.5   Conclusions

Over five years of observations from a meteor radar was used to calculate gravity wave effects on the diurnal variations above the Andes LIDAR Observatory. It was shown that on average, the amplitude of the diurnal tide was mostly increased between 85 and 97 km in both the zonal and meridional directions. The phase was both increased or decreased depending on the altitude.

The results were compared to previous GW-Tidal interaction studies at Maui Hawaii, which used the same meteor radar, and a LIDAR at the Starfire Optical Range in New Mexico. The two meteor radar observations gave very similar rate of diurnal tide amplitude change but the changes in diurnal phase were more different indicating the relative phase between the tides and GWs are not the same. This may be due to differences in the gravity wave source regions around the two locations.

The SOR LIDAR shows the GWs mostly damping the tidal amplitude in contrast to the

meteor radar results which showed a large amount of tidal enhancement. The diurnal phase was also mostly decreased in the LIDAR data while in the Maui meteor radar observations the phase was mostly increased due to the average phase of site specific GW sources. The GW-Tide interactions observed with a meteor radar requires a large amount of averaging across the entire sky from larger gravity wave scales whereas the interactions from the LIDAR are only from smaller short period GWs in a small section of the sky over the instrument site using a few tens of days. This analysis shows that care must be taken to consider exactly what kind of wave scales and the amount of averaging an instrument performs when drawing conclusions about GWs.

The differences in gravity wave scale effects on the tides introduces complexities to the GW-Tidal interaction issue. GW parameterization schemes in GCM's must include some sort of mechanism to account for this to improve the accuracy of the tides. More observations are also needed to create a global profile of the average GW phase around the globe. This would greatly improve the phase of the tides in these models.

Chapter 4

GCM analysis of Tidal Mode GW interactions

4.1 Introduction

In this chapter, the eCMAM and the SD-WACCM GCMs are used to analyze the effect that parameterized GW drag has on the DW1 tide. These models were chosen for this analysis due to the GW parameterization schemes that each employ having opposite affects on the tidal amplitudes. This makes it possible to study how the assumptions in each scheme affects the tide. Both models also use reanalysis data to nudge the dynamical fields in the lower atmosphere towards observations making their background results as close as possible given the differences between models. Each model is also readily available. The SD-WACCM was downloaded from the University Corporation for Atmopsheric Research (UCAR) and run on a local cluster located at Embry-Riddle Aeronautical University. The eCMAM results are all freely available for download from the Canadian Centre for Climate Modeling and Analysis (CCCma) website. Here, the DW1 tides and momentum terms in both models are examined to ascertain how the assumptions in the Lindzen and Hines parameterization schemes effect the tidal amplitudes in the MLT region. An important reason for including GW effects with parameterization schemes in GCM's is to create a realistic zonal mean wind

structure but their interactions with the tides are typically not considered during the tuning process. This study will provide a stringent examination of how each scheme describes GW-tidal interactions. While there are certainly many other parameterization interaction processes that may be examined, this one is not well understood and is a challenging problem because of the large scale differences and is therefore picked to study. Much of this work is currently in press to the Journal of Geophysical Research: Atmospheres.

4.2   Global Circulation Model Descriptions

In most general circulation models (GCMs), the effect of gravity waves are parameterized due to computational constraints. While the zonal mean structure can be simulated reasonably well with a variety of parameterization methods, modeling works have shown notable differences in GW-tide interactions based upon different GW parameterization methods. For example, GCMs which use the Lindzen type (*Lindzen*, 1981) parameterization (e.g. Whole Atmosphere Community Climate Model) tend to suppress the diurnal tidal amplitude (*England et al.*, 2006; *McLandress*, 1998). while those that use the Hines Doppler Spread Parameterization (e.g. Canadian Middle Atmosphere Model) tend to increase the diurnal tidal amplitude (*McLandress*, 1998; *Meyer*, 1999). In order to avoid the dependence on gravity wave parameterization methods in the study of GW-tide interactions, *Watanabe and Miyahara* (2009) used the Japanese Atmospheric General circulation model for Upper Atmosphere Research (JAGUAR) to directly simulate both gravity waves and tides. Their results show that gravity waves can either amplify or suppress the tidal wind depending on the season. Even though JAGUAR does not parameterize gravity waves, it still needs parameterizations for the turbulence associated with gravity wave dissipation. The model is also still limited by the resolution, which cannot resolve small scale gravity waves. The following subsections describe the eCMAM and the SD-WACCM models used for this dissertation as well as the GW parameterization schemes each use.

4.2.1 The extended Canadian Middle Atmosphere Model

The eCMAM is a spectral GCM with a T32 spectral truncation resolution equating to a grid of about 5.6° in longitude and 5.5° in latitude. In a spectral model the calculations are performed in phase space with all the calculated fields converted into a series of basis functions, spherical harmonics in this case. The T32 resolution indicates the infinite series representing the fields are truncated after 32 terms. The model is an extended version of CMAM ranging from the surface to about 210 km with 87 vertical layers. The vertical resolution ranges from around 0.5 km in the troposphere to several kilometers in the mesosphere lower themosphere region. The model is nudged using the ERA Interim reanalysis data by relaxing the dynamic variables in spectral space only to horizontal scales less than T21. The nudging tendency has the form $-(X - X_R)/\tau_0$ where X and X_R are the spectral vorticity, divergence or temperature coefficient for the model and reanalysis data respectively and τ_0 is the relaxation time scale of 24 hrs (*McLandress et al.*, 2013). The tides are generated self-consistently within the model but the GWs are parameterized using the Hines Doppler Spread scheme. GW sources are separated into orographic and non-orographic sources. The eCMAM data available from the Canadian Centre for Climate Modeling and Analysis website is at a 6-hr output frequency. Model year 2006 was chosen for this investigation to better compare with SD-WACCM.

The non extended version of CMAM, with a model top around 80 km, was used by *McLandress et al.* (2013) to study the impacts of parameterized orographic and nonorographic GW drag on the zonal mean circulation during two large sudden stratospheric warmings. In the months leading up to the warming the orographic GW drag was found to influence the circulation more while the nonorographic was found to have a larger impact after. The model was also shown to be in remarkably good agreement with the MLS satellite temperatures zonal winds and CO measurements. *Gan et al.* (2014) used the extended version to investigate the climatologies of the diurnal tides. The seasonal variations in the DW1, DW2 and DS0

tidal modes all compared well with observations from the SABER satellite with the DE3 showing some discrepancies. The cold summer mesopause was also found to be about 10 to 20K colder in the model.

4.2.2 The Whole Atmosphere Community Climate Model

The SD-WACCM is a finite element GCM of the atmosphere ranging from the ground to the lower thermosphere incorporating dynamics, chemistry and radiation. It is an optional set of the Community Atmosphere Model (CAM) which is a component of the NCAR Community Earth System Model (CESM). The specified dynamics subset uses NASA GMAO (GEOS5.1) reanalysis data (*Rienecker et al.*, 2008) to nudge the temperature, horizontal winds and surface pressure by 1% at every timestep below 50 km. From 40 km to 50 km the nudging is linearly reduced such that the model is free running above (*Kunz et al.*, 2011). The model was run at Embry-Riddle Aeronautical University for model years 2005 to 2007 at a horizontal resolution of 2.5° in longitude and 1.9° in latitude with 88 pressure levels from the ground to about 140 km altitude. The vertical resolution in the troposphere is about 0.2 km, 1.1 km in the stratosphere and around 2 km above. The tides in the model are also generated self-consistently while the GWs are parameterized using a modified Lindzen parameterization scheme. The GWs sources here are separated into orographic, convective and frontogenesis sources (*Richter et al.*, 2010). Previous versions of WACCM specified the location and magnitude of GW sources. Beginning with WACCM4, GW source locations and amplitudes depend on dynamical features in the troposphere such as heating depth and surface winds. To match with the available eCMAM results, the SD-WACCM output was taken at a 6-hr time cadence. The 2006 model year was chosen to investigate primarily due to the availability of the reanalysis data for this model version.

The structure of the diurnal tide in WACCM was studied by *Chang et al.* (2008) and compared to the Global Scale Wave Model (GSWM) and a meteor radar above Kauai, Hawaii. A general agreement in the large scale structures and seasonal variability of the

tide betweeen the two models and the radarwas found. A maximum response was found at equinox with a minimum at solstice. The diurnal variations in WACCM were also larger than the radar results due to the superposition of several tidal modes in the model. A new version of the WACCM with data assimilation was compared with SABER and COSMIC satellite observations by *Pedatella et al.* (2016). The short term DE3 tidal variability (10-20 days) in WACCM was found to be in good agreement with both satellite observations. *Davis et al.* (2013) compared meteor radar results from Ascension Island to both the WACCM and eCMAM. As noted before, the diurnal tidal amplitudes were overestimated in eCMAM and underestimated in WACCM but the semidiurnal amplitudes were very similar to the radar results. The vertical wavelengths of the diurnal tide were also generally in good agreement although eCMAM predicted shorter wavelengths in winter while WACCM predicted longer wavelengths in many months.

4.2.3   Gravity Wave Parameterizations

Due to current computational constraints most GCMs are run at resolutions too course to resolve smaller scale features like GWs. While the large scale thermal tides are directly resolved, GWs must be parameterized to include their effects. Without GWs, the models would be missing a key component that is required for a realistic atmosphere. A variety of schemes to parameterize GWs have been developed each with their own assumptions about GW sources and dissipation mechanisms. These parameterization schemes are typically tuned to replicate the zonal mean structure of the winds without major considerations for other dynamics such as the tides. There have been several schemes developed for GW parameterization each with their own specific assumptions about GW sources, source spectra, amplitudes, propagation and dissipation mechanisms. Each of these schemes also have several points of commonality. For instance, all GWs are assumed to only propagate instantly and vertically until they break depositing their momentum and energy into the background flow. Each also contain tunable parameters which can scale wave drag or change the breaking

69

height. Observations are needed to constrain these tunable parameters but a current lack of global GW sources and spectra necessitate tuning the parametrization schemes to balance the models to observed climatologies. Currently there are at least eight major schemes that have been developed to varying degrees of success. The Lindzen scheme (*Lindzen*, 1981) is arguably the most well known and common with many others using it as a basis.

The Lindzen scheme, which SD-WACCM employs, assumes a finite number of waves are launched when the correct conditions are satisfied in the troposphere. The model uses trigger functions for convection, frontogenesis and orographic sources to identify when and where a GW spectrum is created (*Conley et al.*, 2012). Gravity waves are assumed to travel to the model top instantaneously with a vertical drag profile being calculated in a column above the location where the wave spectrum originated. Each waves amplitude grows with altitude independent of the other waves in the spectrum. Once a wave reaches a certain amplitude, its growth is halted and the wave is assumed to be saturated after which it produces a forcing onto the background winds. This occurs at different altitudes with each wave in the spectrum depending on the background conditions. When saturated the wave amplitude is limited but it is still assumed to propagate upward to the top of the model (*Kim et al.*, 2003). Depending on the background conditions, the wave can again provide drag at an altitude above the initial saturation altitude provided it is not critical layer filtered.

A scheme developed by *Alexander and Dunkerton* (1999) used the instability criteria from the Lindzen scheme but assumed the waves are totally dissipated rather than saturated. This allows the scheme to operate on a total spectra of waves instead of a discrete set. *Warner and McIntyre* (2001) developed a spectral analogue to the Lindzen saturation criterion and simplified the computation with a three part spectrum approximation. The Fritts and Lu scheme (*Fritts and Lu*, 1993) also operates on a spectra of waves using saturation theory and empirical constraints to describe spectrally integrated energy density and momentum flux with altitude. Recently, *Yigit et al.* (2008) formulated a parametrization scheme that accounts for different wave dissipation affects in the thermosphere such as molecular viscosity,

thermal conduction, ion friction and radiative damping in the form of Newtonian cooling. It is based on the Lindzen scheme below the mesopause.

The Hines Doppler Spread GW parametrization scheme is used in the eCMAM. Unlike the Lindzen scheme which uses trigger functions to launch GWs, a broad spectrum of waves are assumed to exist that also instantaneously propagate in a column above the source region (*Hines*, 1997). Instead of a set number of discrete waves, the scheme operates on the spectrum itself modifying it based upon the background conditions. As the GW spectrum is assumed to propagate upwards, the vertical wavenumber spectrum widens forming a tail spreading the energy out. The part of the spectrum past the cutoff vertical wavenumber in the tail is dissipated and the energy and momentum in that section assumed transferred to the background. In this scheme, only waves with small vertical wavelengths contribute a drag on the winds after which they are obliterated from the spectrum (*Hines*, 1997; *Kim et al.*, 2003). This scheme is used in other GCMs (e.g. HAMMONIA and ECHAM5) although *Klaassen* (2009) recently cast strong doubts as to the validity of its core assumptions stating that it overestimates the wavenumber spreading and momentum deposition associated with conservative wave-wave interactions. These are important issues for climate modelers to consider but it does not affect the current work because of its more narrow focus on how specific assumptions in the schemes affect the tides.

While computing power is beginning to allow for directly resolvable GWs in GCMs, parameterization schemes are still being implemented where speed is required. Numerical Weather Prediction (NWP) models are used to forecast weather conditions from a day up to a week in advance, e.g. the Navy Global Environmental Model (NAVGEM). They typically assimilate real time data from instruments aboard ships and aircraft along with radiosondes, infrared and microwave sounders, Global Navigation Satellite System Radio Occultations and satellite scatterometers (*Hogan et al.*, 2014). The data assimilation provides the current state of the lower atmosphere as an initial condition to the model. These models are run several times per day with up to date data assimilated so the forecast is as accurate as

possible. The NAVGEM for instance provides up to 180 hour forecasts 4 times a day and 16 day guidance twice a day (*Hogan et al.*, 2014). One of the most important aspects of NWP's is their speed in simulating up to a week of global weather patterns. Previously, most NWP's only extended into the stratosphere since they only needed lower atmosphere weather. This also kept the speed of the simulations at an acceptable rate. Recent understandings of the importance of whole atmosphere coupling and availability of satallite observations has led to extensions into the upper mesosphere and with it the need for GWs to balance the momentum budget (*Eckermann et al.*, 2009). Speed is still important in these extended models so running at high enough resolutions to directly resolve GWs is not feasible, thus the continuous need for a parameterization schemes.

4.3   Method

The method for deriving the DW1 tide parameters and GW affects on them are described in this section. Equations (4.1) and (4.2) are the momentum balance equations for the atmosphere in the zonal and meridonal directions respectively, where u is the zonal wind, v is the meridional wind, Φ is the geopotential, $\vec{V}$ is the horizontal wind vector, f is the coriolis parameter, λ is the latitude, a is the earth's radius and ϕ is the longitude. The first term on the right hand side in each equation is the coriolis forcing, the second term is the pressure gradient forcing, the third is the forcing due to advection while the forth is forcing due to curvature.

$$
\frac{\partial u}{\partial t} = fv - \frac{1}{a\cos\phi}\frac{\partial \Phi}{\partial \lambda} - \vec{V}\cdot\nabla u + \frac{uv}{a}\tan\phi + ...
$$
$$
F_{GW,x} + F_{Ion,x} + F_{Diffusion,x} + X,
$$
(4.1)

$$
\frac{\partial v}{\partial t} = -fu - \frac{1}{a}\frac{\partial \Phi}{\partial \phi} - \vec{V}\cdot\nabla v + \frac{u^2}{a}\tan\phi + ...
$$
$$
F_{GW,y} + F_{Ion,y} + F_{Diffusion,y} + Y,
$$
(4.2)

Where,

$$\vec{V} \cdot \nabla u = -(\frac{u}{a \cos \phi} \frac{\partial u}{\partial \lambda} + \frac{v}{a} \frac{\partial u}{\partial \phi} + w \frac{\partial u}{\partial z}), \tag{4.3}$$

$$\vec{V} \cdot \nabla v = -(\frac{u}{a \cos \phi} \frac{\partial v}{\partial \lambda} + \frac{v}{a} \frac{\partial v}{\partial \phi} + w \frac{\partial v}{\partial z}), \tag{4.4}$$

The forcing parameters on the second line of each equation are obtained directly from the model output where $F_{GW,x}$ and $F_{GW,y}$ are the zonal and meridional GW forcing, $F_{Ion,x}$ and $F_{Ion,y}$ are the ion forcing in the zonal and meridional directions, $F_{Diffusion,x}$ and $F_{Diffusion,y}$ are the forcings due to molecular diffusion in the zonal and meridonal directions and X and Y are other non-conservative forcings in the respective directions. The ion, diffusion and other non-conservative forcing terms are much smaller compared to the other terms in the momentum equations and are thus ignored for this analysis. Each term on the right hand side are calculated or obtained from model output at all grid points every 6 hours for both eCMAM and SD-WACCM.

The DW1 component of the winds and each momentum equation terms tidal mode projection are calculated with a two dimensional Fast Fourier Transform (FFT) in longitude and time at every latitude and altitude. The amplitude of the DW1 components are found by taking the absolute value of the complex amplitudes given by the 2-D FFT.

The effects that each forcing term has on the tidal winds can be quantified with the Equivalent Raleigh Friction (ERF) as in the previous chapter. Each of the terms in the momentum equation are a type of forcing so the ERF may also be used to evaluate their effects on the tide. The non-modified definition for the ERF can be used since the models can give the total global structure estimates of the tide and the forcing terms,

$$\gamma = -\frac{1}{\hat{u}} \frac{d\hat{u}}{dt} = -\frac{\hat{F}}{\hat{u}}. \tag{4.5}$$

To calculate the ERF directly, the complex amplitudes $\hat{u}$ and $\hat{F}$, obtained from the 2D

FFT's, are simply divided. The change in tidal amplitude due to GWs is

$$\frac{du}{dt} = -\text{abs}(\hat{u})\text{Re}(\gamma), \tag{4.6}$$

with the change of phase being

$$\frac{d\Psi}{dt} = \text{Im}(\gamma). \tag{4.7}$$

4.4 Results and Analysis

Two months were chosen for this analysis so that the observed differences are not seasonally dependent. For equinox conditions when the tides are strongest, the month of March was chosen and July for solstice when the tides are weaker.

4.4.1 Tidal Component Amplitudes

To begin, the magnitude of the DW1 component of the tidal winds are shown in Fig. 4.1 for the zonal direction and Fig. 4.2 for the meridional in both eCMAM and SD-WACCM for March and July. The DW1 tide in both models is stronger in March than in July which is expected from observations and other model results (*Forbes et al.*, 2008; *Oberheide et al.*, 2011; *Akmaev et al.*, 2008). Below about 70 km the tidal magnitudes are similarly small between models in both months. Above this altitude however the tidal amplitudes are quite different. The eCMAM shows the DW1 tide not only having a different structure than SD-WACCM but more than double the amplitude in each month at low to mid latitudes. The maximum amplitude in the zonal direction is 43m/s in eCMAM but only 16m/s in SD-WACCM in March. Similarly, in the meridional direction the maximum tidal amplitude is over 80m/s in eCMAM and 24m/s in SD-WACCM in March. July shows weaker amplitudes in both models with eCMAM still exhibiting approximately double the tidal magnitudes in both directions. The meridional components of the DW1 tidal amplitudes in the models in March and July is in Fig. 4.2. Note the color range differences. The amplitudes are about
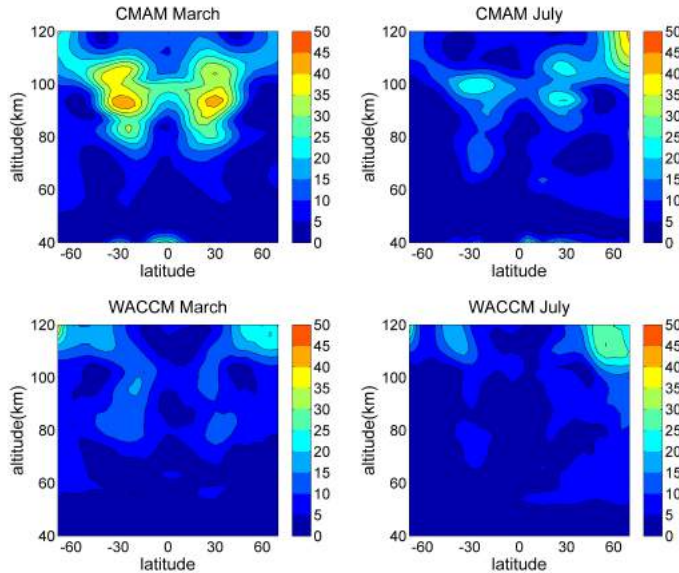
Figure 4.1: Zonal DW1 tidal wind amplitudes (m/s) in CMAM (top plots) and WACCM (bottom plots) in March (left plots) and July (right plots)

50% larger in both models. The peaks of the tidal amplitudes are also at similar latitudes and altitudes.

Previous satellite observations show the DW1 tidal amplitudes to be between the magnitudes of each model. The Wind Imaging Interferometer (WINDII) aboard the Upper-Atmosphere Research Satellite (UARS) for example found the diurnal amplitudes in the zonal direction reaching up to 35m/s and 60m/s in the meridional in March of 1993 (*Yudin et al.*, 1997). *Huang et al.* (2006) used wind data from the High Resolution Doppler Imager (HRDI) on the UARS satellite and the TIMED Doppler Interferometer (TIDI) on the Thermosphere-Ionosphere-Mesosphere-Energetics and Dynamics (TIMED) satellite to study the DW1 amplitudes in the meridional direction. Using a 4 year average of spring equinox, the HRDI tidal amplitudes were around 60m/s while the TIDI instrument recorded amplitudes around 40m/s. The DW1 tides in eCMAM are larger than both studies using the two different sattelites while SD-WACCM is smaller than both.

The percent difference in tidal amplitudes between models in each month is shown in Fig. 4.3. Here the percent difference is defined as the difference between tidal amplitudes
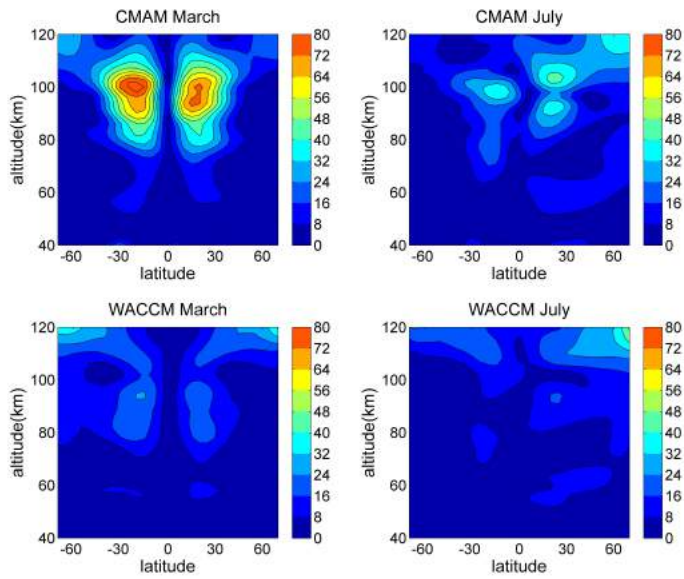
Figure 4.2: Meridional DW1 tidal wind amplitudes (m/s) in CMAM (top plots) and WACCM (bottom plots) in March (left plots) and July (right plots)
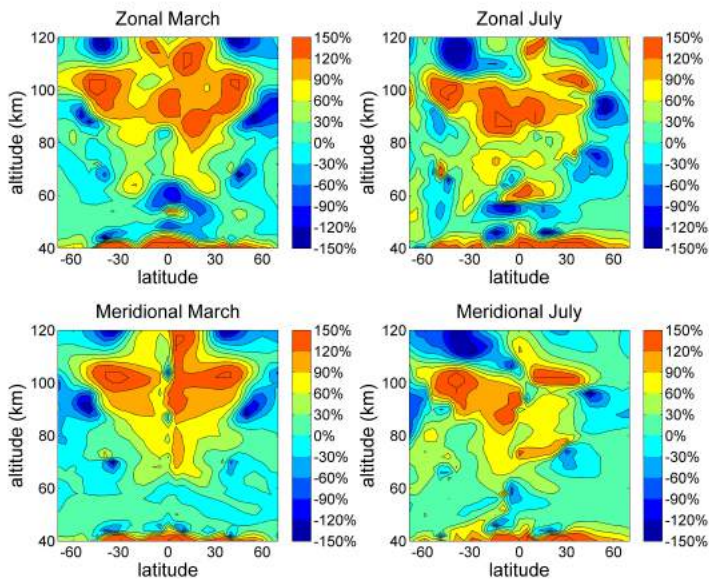

Figure 4.3: Percent difference in DW1 tidal wind amplitudes between models in the zonal (top plots) and meridional (bottom plots) directions in March (left plots) and July (right plots)

divided by the average all multiplied by 100. A positive percent difference indicates the DW1 tide in eCMAM is larger while negative indicates SD-WACCM is larger. From the figures, the percent difference does not change very much between months even with some slight shifting of the peaks. This indicates the mechanism responsible for the difference in tidal amplitudes does not have a strong seasonal dependence in either direction. A seasonal dependence would imply the tidal differences may be due to some dynamical feature present in one of the models that greatly effects the tides. Since this is not present the mechanism must be due to some property or parameterization that is constant throughout the year in each model.

4.4.2   Tidal Component of Gravity Wave Effects on the Tidal Winds

Here the tidal projection of GW forcing from the parameterization schemes in each model is examined. Fig. 4.4 shows the rate of change of the zonal DW1 tidal winds due to the zonal GW forcing with the GW forcing in colors and the DW1 tidal wind amplitude in the contours. The left plot is in eCMAM and the right SD-WACCM with the left showing march and July on the right. Overall, the DW1 component of GW forcing in both models and months tends to decrease the tidal amplitude when forcing is present. For the summer equinox in eCMAM, the tidal winds are decreased by over 30m/s/day at the higher latitudes where the tide is weaker. At low to mid-latitudes where the tides are strongest, the GW's effects on the tide are near 0. On the other hand, the GW forcing in SD-WACCM has a larger drag effect on the tide at middle latitudes by inducing a dampening effect of around 30m/s/day. Both models have the GW forcing creating a large drag on the tide at higher latitudes and altitudes with SD-WACCM being larger. The effect on the tide is smaller at solstice. The higher latitudes and altitudes still show strong damping by the GWs, but is only at the northern pole in eCMAM and some weaker effects at middle latitudes around 80 km. This is again away from the peaks in the DW1 amplitude. SD-WACCM similarly shows weaker changes in tidal amplitudes compared to equinox at all latitudes and altitudes. The northern pole like
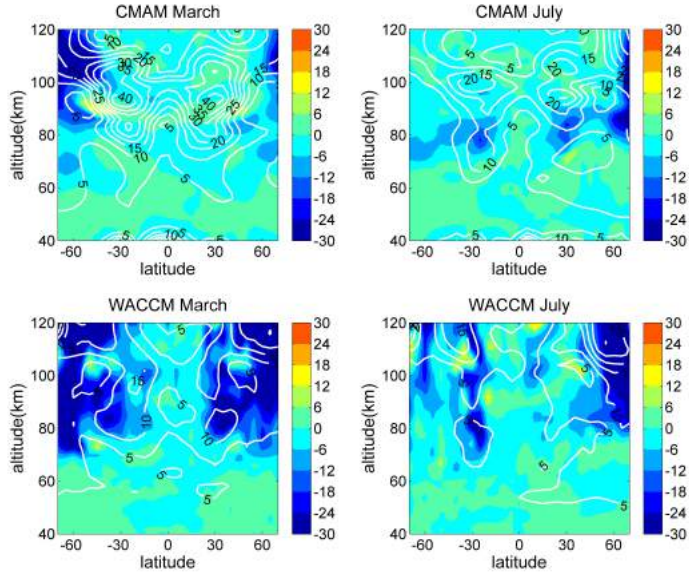
77

Figure 4.4: Zonal DW1 wind amplitude change rate (m/s/day) (colors) due to DW1 projection of GW forcing and DW1 tidal winds (contours). The tidal contours are in increments of 5 m/s. The left plots are for March, the right for July, the top plots are for CMAM and the bottom are WACCM.

eCMAM is the largest region of damping but some negative rates of amplitude change also occur at the southern pole. The GWs in eCMAM do not have a large effect on DW1 when it is largest. The damping is either at higher latitudes or lower in altitude. In SD-WACCM on the other hand, larger GW damping does occur both where the tide is strongest and at the higher latitudes like in eCMAM. The results in the meridional direction are very similar and are shown in Appendix A.

The tides are a global feature of the atmosphere and are affected by many different mechanisms. A simple method to test how the GW parameterization schemes affect the tides would be to remove them from the model and compare the results to the model with the schemes intact. This is unfortunately not feasible because many other components are tuned within the models assuming GWs exist providing a forcing on the background winds. Removing such an important piece would lead to numerical instabilities. Instead we must attempt to isolate GW affects on the tide by finding locations where they are dominant over the other terms in the momentum equation. Fig. 4.5 shows the amplitude rate of

change of the zonal DW1 tide due to each term in the momentum equation at 35° latitude in March. Here the forcing due to GWs is a major cause of changing the DW1 amplitude in SD-WACCM but not in eCMAM. The DW1 component of GWs in eCMAM does not have large amplitudes at the mid to lower latitudes where the tide is strongest so their effects on the tidal winds here are limited. The larger GW forcing where the tides are strongest in SD-WACCM on the other hand are at locations where the GWs can greatly affect the tidal amplitudes compared to the other terms in the momentum equation. Gravity waves provide a damping rate on the DW1 tides of between 25 and 50m/s/day in the 80 to 100 km region. This damping is mostly balanced by both the coriolis and pressure gradient forcing in SD-WACCM. In eCMAM, the GW forcing is much smaller so the balancing of the momentum equation is done with the pressure gradient and/or the advective forcing against the coriolis forcing. At latitudes where the GW forcing is stronger in eCMAM, the pressure gradient serves as the major balancing to the GWs. In both models the classical terms are the largest balancing force for the DW1 tide when GW forcing is stronger. While it is possible for shear and convective instabilities to affect the tidal amplitudes similar to breaking GWs (*She et al.*, 2004; *Li*, 2009; *Yue et al.*, 2010), there is not a mechanism in either model to include these affects.

Recently, *Agner and Liu* (2015) used a LIDAR at the Starfire Optical Range (35.0°N, 106.5°W) to study the effects of short period (less than 2hr) GWs on the diurnal variations over 24 nights from 1998 to 2000. These small scale GWs induced strong damping on the zonal component of the tides between 87 km and 97 km and below 95 km in the meridional direction. Other altitudes showed some enhancing of the tidal amplitudes. Similarly, a meteor radar was used by *Liu et al.* (2013) to also study the effects of GWs on the diurnal variations at Maui Hawaii (20.7°N, 156.3°W). These observations showed that GWs both dampen and enhance the tidal amplitude with a dependence on month and altitude. In a five year composite day GWs damped the tides between 86 and 90 km in the zonal direction and between 84 and 91 km in the meridional. Between 90 and 97 km, the tidal amplitudes
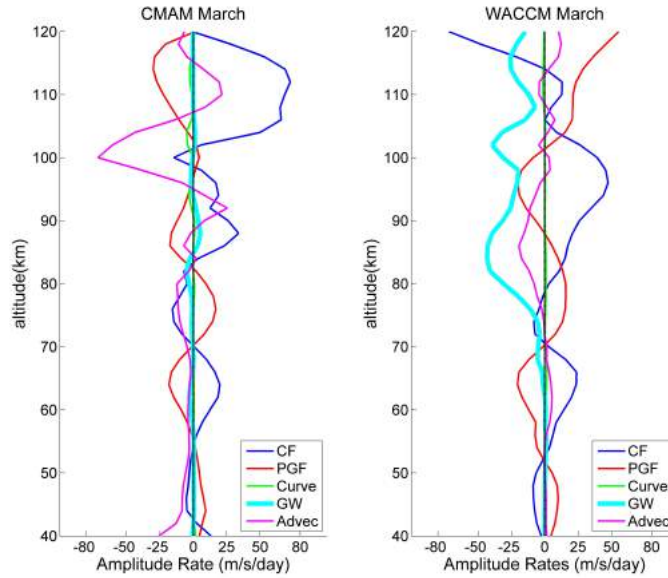
Figure 4.5: Amplitude rate of change of the DW1 zonal tidal winds (m/s/day) due to each term in the momentum equation in March at 35° latitude

were enhanced up to 80 m/s/day in both directions. It should be noted that both of these observations are using single sites to study the diurnal variations which include other tidal modes besides DW1. While this is not a direct comparison, the DW1 tide is very large at the low to mid latitudes especially around the Maui site and should represent the majority of the diurnal variations there. The large positive amplitude change by GWs is not shown in either model which always provides a drag on the tides.

A large factor in how the tidal amplitudes are changed by the GW forcing is the relative phase difference between them. The phase of the tide is affected more by the GW forcing when the phase difference is near 90 or 270 degrees. The effect on the tidal amplitude is greatest when the phase difference is near 0 or 180 degrees (*Ortland and Alexander*, 2006). Fig. 4.6 shows the mean relative phase difference between the zonal DW1 tidal winds and the DW1 projection of the zonal GW forcing. The mean phase was taken between ±45° and ±10° where the DW1 tides are strongest. On average, the phase difference in eCMAM is near 90° between 80 and 110 km affecting the phase of the tide more than the amplitude. In SD-WACCM, it is closer to 180° which changes the tidal amplitude more than the phase.
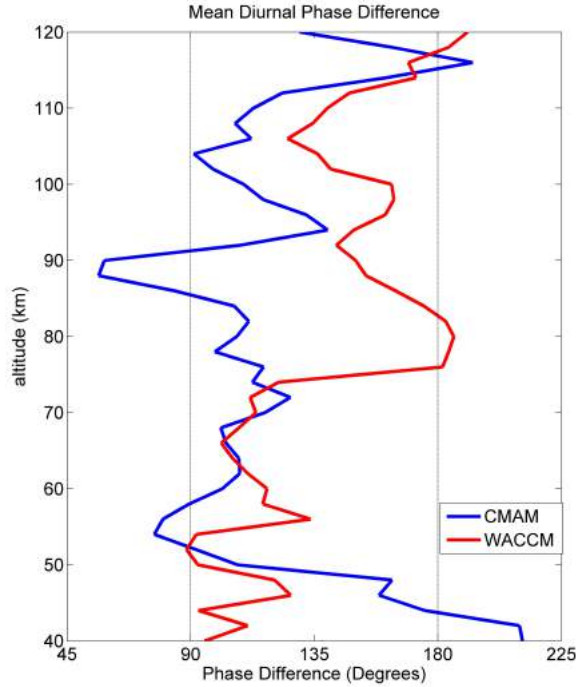
Figure 4.6: Mean phase difference between the zonal DW1 tidal winds and the diurnal projection of the GW Forcing in the zonal direction between $\pm 45°$ and $\pm 10°$ latitude

This at least partially explains why the amplitude of the tides are decreased much more than in eCMAM at the low to mid latitudes. From 50 km to 75 km the relative phase differences in the two models are similarly closer to $90°$ but the GW forcing is much weaker here so it has minimal effects on the tides in the MLT region.

4.4.3 Non-Tidal Winds and GW Forcing

The DW1 projection of GW forcing using the Lindzen parameterization scheme in SD-WACCM has been shown to produce a larger drag on the DW1 tides than the Hines scheme in eCMAM where the tides are stronger. The question now turns to why this occurs. Here the raw winds and GW forcing are analyzed to determine which assumptions in the parameterization schemes create these dissimilar effects on the tides. The zonal components are shown in this section with the meridional in Appendix A due to similarities in results.

The zonal monthly mean winds and GW forcing are shown in Fig. 4.7 for March at
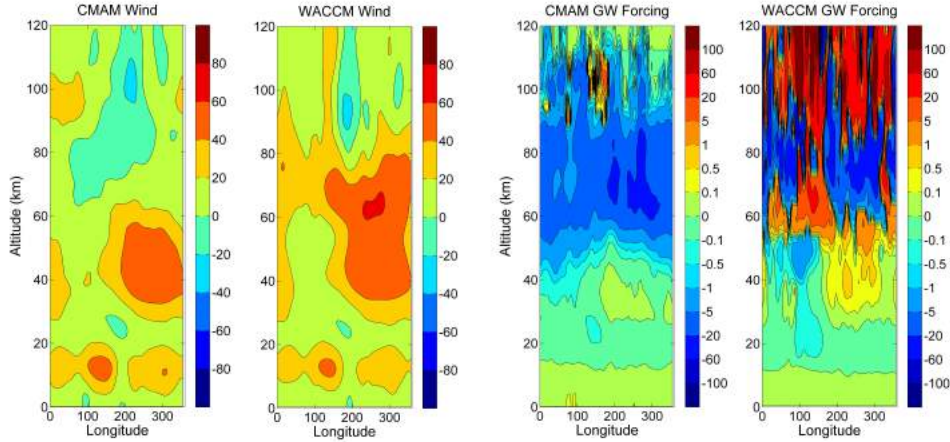
81

Figure 4.7: Monthly mean zonal wind (m/s) (left plots) and GW forcing (m/s/day) (right plots) in CMAM (first and third plots) and WACCM (second and fourth plots) at 35° latitude in March. An uneven color scale is used to show smaller scale variations in the GW forcing.

35° latitude. The left plots show the winds for eCMAM and SD-WACCM while the right plots show the smoothed GW forcing. Below 60 km, the monthly mean winds in the zonal direction are very similar in both models at altitudes where the GW forcing is weaker. Above 60 km however, the winds show large differences between models most markedly between 60 and 80 km where the mean winds are almost 70m/s larger in SD-WACCM. The GW forcing in eCMAM is far weaker than SD-WACCM at all altitudes. Below 50 km, the forcing due to GWs shows similar magnitudes in the models with SD-WACCM being slightly stronger. This region does not show any significant difference in the mean winds. At these lower altitudes the forcing from GWs is much smaller compared to the MLT region and does not provide enough acceleration on the winds to affect them in a meaningful way.

Moving on to the upper altitudes, the mean GW forcing in eCMAM is strongest between 60 and 90 km and between 150° and 360° longitude reaching -35 m/s/day. This is also the region where the mean winds are most different to SD-WACCM. The mean GW forcing in SD-WACCM not only has positive and negative regions but is also much larger and occurs at all altitudes above 70 km. Between 70 and 90 km much of it is negative similar to eCMAM but all altitudes above 90 km shows very strong forcings that are both positive and negative.

Fig. 4.8 is the same plots as Fig. 4.7 but for solstice conditions in the month of July
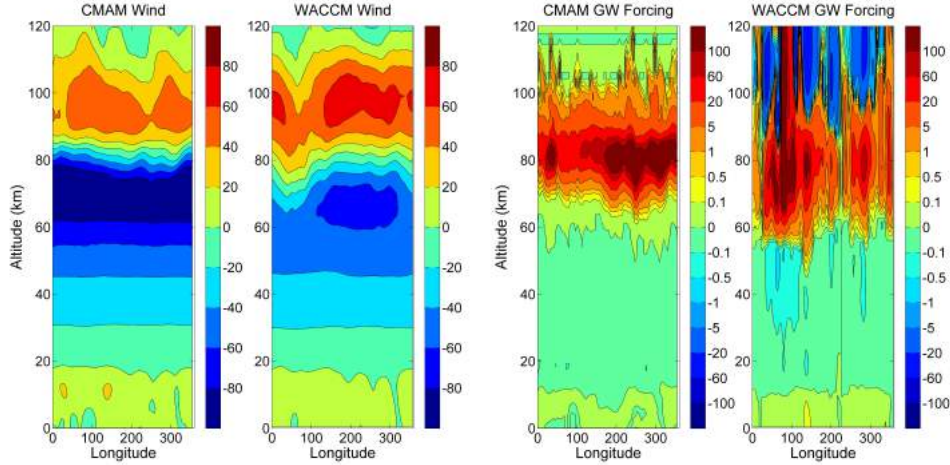
Figure 4.8: Monthly mean zonal wind (m/s) (left plots) and GW forcing (m/s/day) (right plots) in CMAM (first and third plots) and WACCM (second and fourth plots) at 35° latitude in July. An uneven color scale is used to show smaller scale variations in the GW forcing.

instead of March equinox. Here the mean winds in the zonal direction shows strong westward flows in the mesosphere indicative of the summer time mesospheric jets (*Burks and Leovy*, 1986; *Sato et al.*, 2009). The jet is stronger and reaches higher altitudes in eCMAM. A reversal in mean zonal wind direction occurs around 80 km with SD-WACCM being slightly stronger above. While there are some differences in the altitude of the reversal and the magnitude of the jets, both models have relatively similar mean winds. The mean GW forcing is also quite similar with strong positive forcing between 70 and 100 km.

From these results, in regions where the GW forcing is weak in both models the mean winds are very similar. On the other hand, altitudes where the GW forcing becomes strong and is very different between models the mean winds show many differences. When the mean GW forcing is similar, the mean winds are also comparable This suggests that the GW forcing from the parameterization schemes is at least partially responsible for the differences in the mean background winds between the two models.

Looking deeper into the relationship between the winds and GW forcings, Fig. 4.9 shows the longitude-time plots of the zonal winds in eCMAM and SD-WACCM at -25° latitude and 95 km altitude at March equinox. This is a location where the DW1 tides are relatively
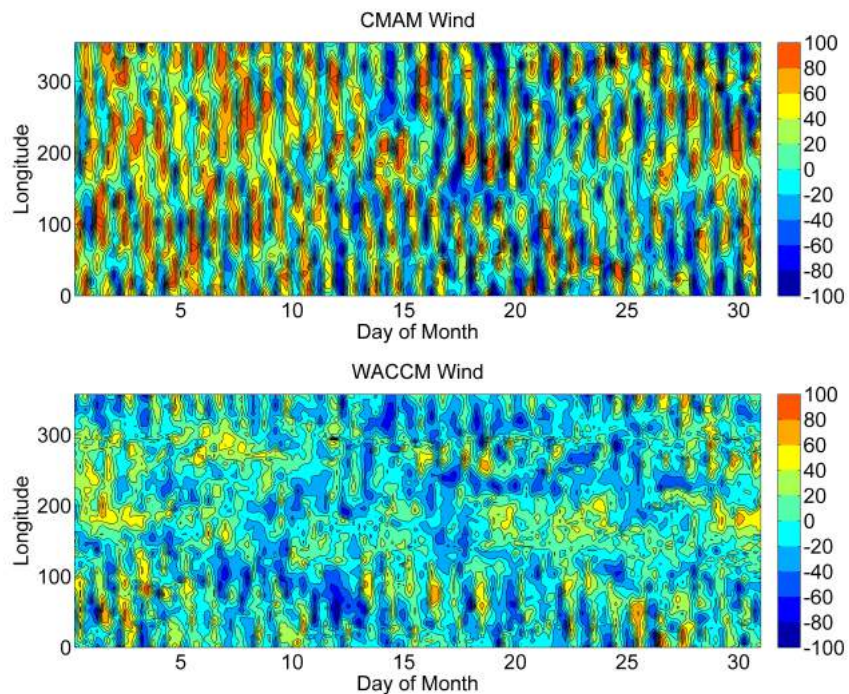
Figure 4.9: Zonal wind (m/s) in CMAM (top) and WACCM (bottom) at -25° latitude and 95km in March

strong in both models as seen in Fig. 4.1. The most striking feature in eCMAM is the strong diurnal variations seen throughout the month across all longitudes. While these variations are also observed in SD-WACCM they are not as clearly structured and are nearly non-existent around 200° longitude. The strength of the diurnal variations are consistent with the amplitudes shown in Fig. 4.1. Fig. 4.10 shows the zonal winds for July at 30° latitude and 95km where the DW1 tide is relatively strong. The diurnal variations in eCMAM are not as pronounced as they were at equinox but they are still present throughout the month. The winds are mostly positive indicating the amplitude of the tidal variations are smaller as predicted by the FFT analysis in the previous section. In SD-WACCM, the diurnal variations are more structured at the mid latitudes compared to March and like eCMAM, are mostly positive.

The longitude-time cross section of the GW forcing in eCMAM (top) and SD-WACCM (bottom) at 35° latitude and 84 km altitude is shown in Fig. 4.11. A different location was
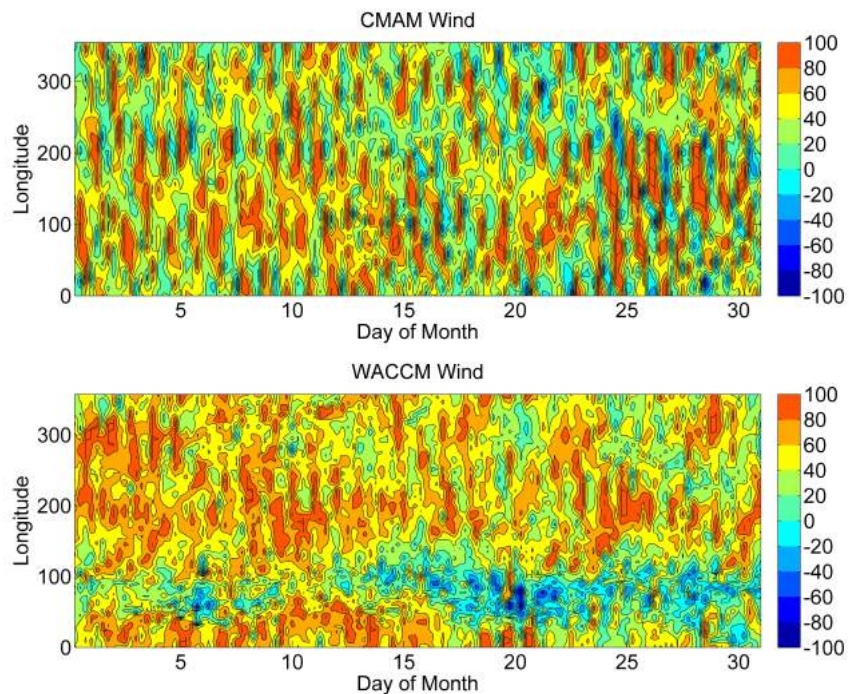
Figure 4.10: Zonal wind (m/s) in CMAM (top) and WACCM (bottom) at 30° latitude and 95km in July

chosen to analyze here because the GW forcing in eCMAM is very weak at lower latitudes. To more effectively show the key features of each parameterization scheme, a location with stronger GW forcing in both models is shown. Similar to the winds, the GW forcing in eCMAM exhibits strong diurnal variations indicating the parameterization scheme allows a high degree of modulation of the GWs by the diurnal tides. Diurnal variations in the GW forcing in SD-WACCM on the other hand are not as clear. The GW forcing has distinct patterns moving eastward with time at this latitude. To explain this it should be noted that the forcing due to GWs is calculated in a column directly above the GW source. The forcing profile with altitude is calculated immediately assuming the propagation time for the waves is instantaneous. A major source of GWs in SD-WACCM are fronts. The patterns in the GW forcing seen in the MLT region are moving fronts in the troposphere triggering the parameterization scheme.

The GW forcing in July at 30° latitude and 80km is shown in Fig. 4.12. The forcing in
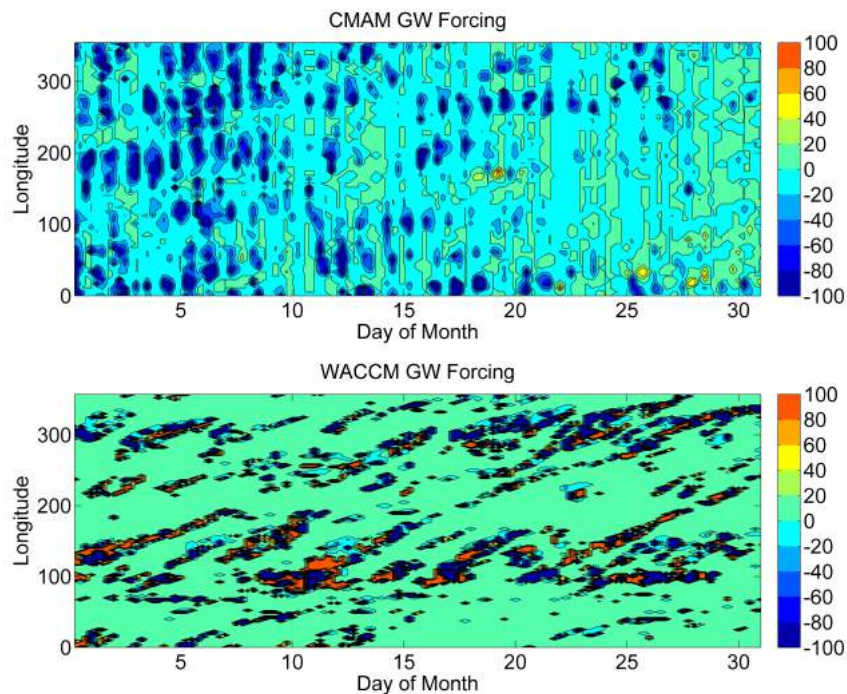
Figure 4.11: Zonal GW forcing (m/s/day) in CMAM (top) and WACCM (bottom) at 35°
latitude and 84km in March

eCMAM is much stronger as seen in the monthly and zonal mean plots. Here the modulation
by the tidal winds are not as strong as in equinox but is still present matching the less
structured winds from Fig. 4.9. In SD-WACCM the diagonal stripes of GW forcing with
time are absent at solstice conditions and instead the forcing mostly remains around a single
longitude after it begins. Since this is the summer season in the northern hemisphere,
convective storms are a common occurrence at the low to mid latitudes. They do not travel
as far as fronts or last as long, hence the patterns in the GW forcing are due to the storm
systems triggering the convective sources for the GWs.

While the Hines scheme in the eCMAM also calculates a forcing profile in a column above
the source region, the entire spectrum changes depending on the background conditions
whereas it is static in the Lindzen scheme. The Hines scheme assumes only the part of
the GW spectrum with smaller vertical wavelengths produces a forcing on the background
winds. As the GW forcing profile is calculated in the column above the source region, the
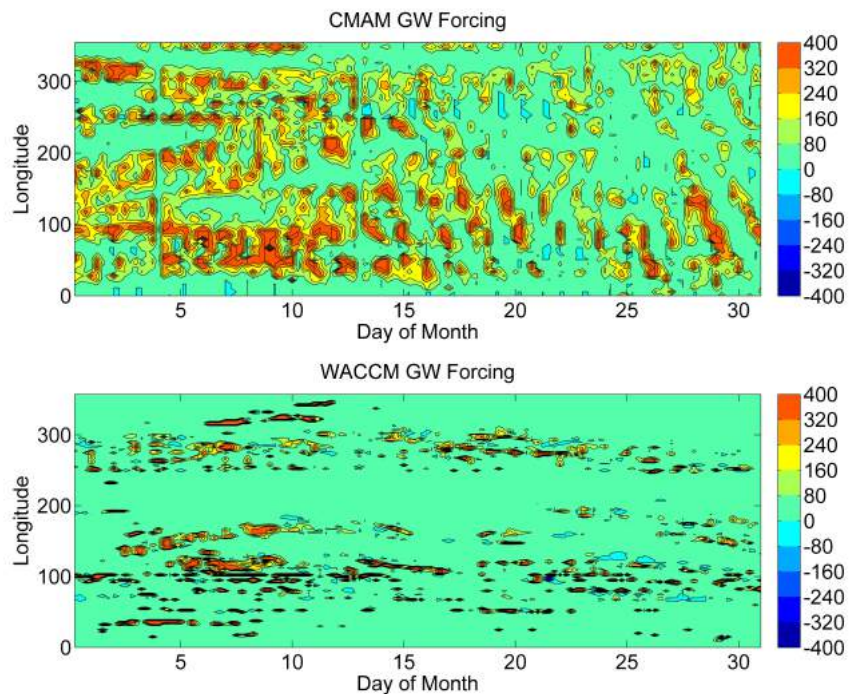
Figure 4.12: Zonal GW forcing (m/s/day) in CMAM (top) and WACCM (bottom) at 30°
latitude and 80km in July

winds shift the wave spectrum into the smaller scales which produce the forcing, creating the

observed modulation. The stark difference in GW forcing is mainly because the spectrum

is allowed to change in the Hines scheme but is static in the Lindzen scheme as they are

assumed to propagate upwards.

The different wave dissipation mechanisms may also explain these differences and how

they affect the DW1 tide. Each wave launched in the Lindzen scheme from the source region

travels to the model top as seen in the longitude-time cross section and the monthly mean GW

forcing. The waves become saturated at various altitudes depending on the wave parameters

and background conditions but still exist within the model. They can still deposit more

momentum and energy into the background above the breaking level. Since all waves exist

at the upper altitudes the GW forcing tends to be very large which over damps the winds

and DW1 tidal amplitudes compared to observations. While wave saturation is an accepted

theory for wave dissipation, not all waves may undergo this process. Some smaller scale

87

waves would be completely absorbed into the background flow or be obliterated in wave-wave interactions. With the Hines scheme, only small scale waves produce the forcing and are obliterated from the spectrum after they deposit their energy and momentum. None of these waves undergo saturation. The acceleration on the winds by these smaller scale waves which do not continue to propagate after their breaking altitude is not enough to constrain the DW1 tides when compared to observations. The Lindzen and the Hines scheme assumes the waves producing the forcing are either all saturated or all obliterated, respectively. It is more likely that a combination of saturation and obliteration occurs.

4.5   Summary and Conclusions

The interaction between GWs and the tides is not well understood due to the differences in wave scales, frequencies and the intermittency of GWs. GCM's must use parameterization schemes to include the effects of the relatively smaller scale GWs. The schemes are tuned to reproduce the mean wind structure without consideration of other atmospheric features such as the thermal tides. Each GW parameterization scheme inherently includes many assumptions about how GWs affect the atmosphere. It has been shown here and in previous studies that the Lindzen scheme produces more drag on the tides than the Hines Doppler Spread scheme. The Hines scheme also only creates significant drag at upper latitudes where the DW1 tides is weaker. The Lindzen scheme on the other hand produces strong forcing at the mid to high latitudes including where the tide is strongest.

The GW schemes in each model change the mean monthly winds at altitudes where the GW forcing is strongest. The winds below are very similar in the models but each scheme causes differences in the mean winds above 60 km. A longitude-time cross section reveals the GW forcing is highly modulated by the tidal winds in eCMAM but not in SD-WACCM. In SD-WACCM, the time and location of the GW forcing depends on the source in the troposphere whereas in eCMAM it depends on the winds near the forcing altitude. Only

smaller scale GWs are assumed to deposit momentum and energy into the background in the Hines scheme after which they are obliterated. The winds change the GW spectrum creating the modulation of the GW forcing that is on average around 90° out of phase with the winds. This changes the tidal phase more than the amplitude and in conjunction with the forcing coming only from smaller scale waves explains the larger DW1 tides in eCMAM and other models which use the Hines scheme. In the Lindzen scheme all waves in a static spectrum are assumed to be saturated after their breaking level. Depending on the background conditions the same wave could again deposit more momentum into the flow above the breaking altitudes. The forcing from the GWs is also nearly 180° out of phase with the winds which creates changes in the tidal amplitudes more than the phase. Combined with the larger accelerations, the Lindzen scheme has a tendency to overdamp the tidal amplitudes. This analysis shows that when only small scale waves are obliterated to create the GW forcing, the tidal amplitudes are not sufficiently damped but are overdamped when all waves are assumed to be saturated.

The issue of GW interactions with the tides seems to be greatly affected by GW dissipation mechanisms. Observations and high resolution modeling studies can give valuable information on how GWs deposit their momentum into the background winds. This can lead to modification of current parameterization schemes or development of new ones which include better assumptions about GW dissipation thus improving tidal amplitude predictions in GCM's.

Chapter 5

GCM Analysis of Local Time Diurnal Variations - GW Interactions

5.1 Introduction

Chapter 3 analyzed the GW-Tidal interactions from two ground based observational data sets while Chapter 4 used GCM's to study the interactions on a global scale. In this chapter, the GW effects on the tides are analyzed in eCMAM and WACCM again but on a local time scale instead of a global scale. Most observations methods except satellites view a single location above the earths surface and cannot determine the global structure of the tides and their interactions with GWs. In fact, the diurnal variations an instrument observes are typically a superposition of several diurnal tidal modes and not just DW1. The summation of modes above a single location depend on the latitude, determining which modes are strongest, and phase of the tides. Two different diurnal tides which are in phase with each other would look to the instrument to be a single large amplitude tide whereas the two modes out of phase would have a much smaller amplitudes. Any combination between in phase and out of phase may occur and in addition many more than two modes may be present further skewing the calculated diurnal amplitude.

Using the GCM's from Chapter 4, a global picture of GW parameterization effects on the

local time (LT) diurnal variations (wind variations above a single location) can be established. This can also reveal which tidal mode winds and GW forcing projections are most responsible for the diurnal variations.

5.2   Method

To analyze the local time effects on the tide by GWs a diurnal phase aligned composite day was first constructed for each month in the 2006 model year in both models. Due to the changing phase of the diurnal variations at a single location, the various forcing terms from equations (4.1) and (4.2) need to be binned with the phase of the diurnal component of the winds. This was done by first calculating the phase of the diurnal variations at 90 km altitude for each longitude, latitude, and every 6 hours using a 1D FFT with a 5 day sliding window. Twelve phase bins between 0 and 2π radians were chosen as a balance between the number of data points within each bin and the degrees of freedom for the diurnal fit. The calculated phase is matched to the closest phase bin and the winds and momentum equation terms are then stored in the appropriate phase aligned variable. All data points within each bin is then averaged to compute the composite day for each month.

Due to the intermittent nature of the gravity wave forcing in WACCM and to remove smaller variations not related to the larger scale diurnal tides, the diurnal phase aligned variables are horizontally smoothed with a running mean in a two dimensional hamming window. For each longitude, latitude, altitude and phase bin an average within $10°$ in longitude and latitude is calculated and assigned to each grid point for each momentum equation term and wind. Next, the complex amplitude of the diurnal component for the composite day is calculated with a 1D FFT at every longitude, latitude and altitude. To more accurately compare specific locations within each model an interpolation was performed in longitude, latitude and altitude. The interpolated grid has a horizontal spacing of $5°$ and 2 km in altitude from 40 km to 130 km.

5.3 Results

5.3.1 Horizontal Structure of Local Time Diurnal Variations and Diurnal GW Forcing

The horizontal structure of the LT diurnal amplitudes of a composite day at 90 km is shown in Fig. 5.1 for eCMAM and SD-WACCM in March and July. At equinox conditions the LT diurnal variations are very strong at the low to mid latitudes in eCMAM. The locations of maximum amplitudes occur in two bands symmetric about the equator. From the zonal DW1 tidal amplitudes in Fig. 4.1, these are also the latitudes where the DW1 tide tends to be the strongest. This is not seen at all in SD-WACCM. Instead the LT variations do not have any sort of coherent structure across the globe at this altitude and have a large amplitude region around -30° latitude and 75° longitude. A few other locations show larger amplitudes but are in seemingly random locations. The overall magnitudes are also much smaller than in eCMAM. At solstice, eCMAM looses much of the diurnal variations horizontal structure although it is still weakly present. SD-WACCM once again only has a few areas of strong dirunal amplitudes. The LT diurnal variations are much weaker in both models compared to equinox similar to the DW1 tide.

The LT diurnal variations at 90 km in the meridional direction is shown in Fig. 5.2. Like the zonal components, there are two distinct bands of larger amplitude diurnal variations around ±20° latitude in eCMAM which is also where the meridional component of DW1 is strong. SD-WACCM shows a similar but much weaker and less coherent structure unlike the zonal direction. This is most likely due to the larger DW1 amplitudes in the meridional direction influencing the LT variations more. At solstice SD-WACCM looses all traces of the horizontal structure while it is still weakly present in eCMAM similar to the zonal direction.

With the global structure of the LT diurnal wind variations found, the amplitudes of the LT diurnal projection of GW forcing can be analyzed to determine how it affects the local
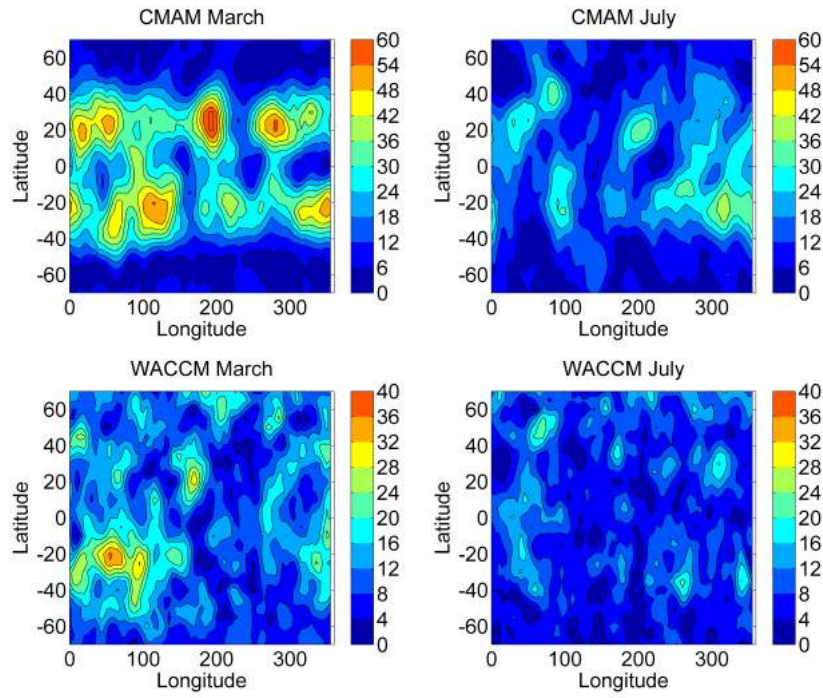
Figure 5.1: Local time zonal wind diurnal amplitudes of a diurnal phase aligned composite day for the month of March at 90km.
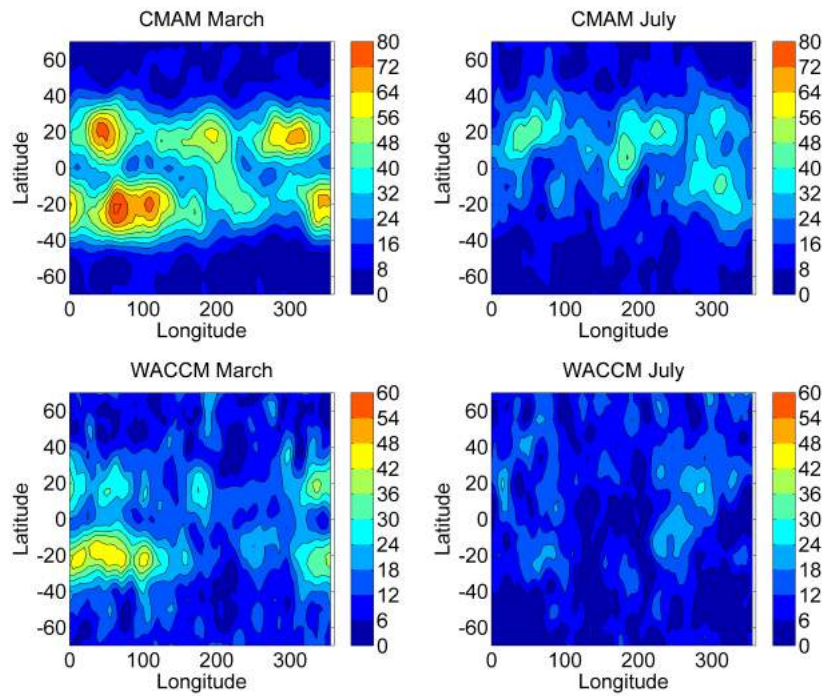

Figure 5.2: Same as Fig. 5.1 but in the meridional direction

93

diurnal winds. The LT amplitudes of the diurnal projection of zonal GW forcing is shown in Figure 5.3 for eCMAM and SD-WACCM at 90 km in March and July. The forcing in eCMAM has a noticeable seasonal dependence with the vast majority of the forcings at the southern pole for the March equinox and more mixed but with much of it at the northern pole in July. While not shown here, the LT diurnal forcings are concentrated at the northern pole for the September equinox and more mixed at the December solstice. Compared to the diurnal variations in the zonal winds, the largest regions of diurnal GW forcing are at completely different locations in March . This severely limits the the effects that GWs can have on the tidal winds. In July, there are some areas of correlated amplitudes but most of the largest are at higher latitudes with the diurnal winds being stronger at lower latitudes.

A similar situation appears in SD-WACCM even with the large differences in GW forcing. Here, the largest diurnal forcing amplitudes are at higher latitudes away from the poles and are present in both hemispheres. It does not have as strong of a seasonal dependence as in eCMAM but the forcing is overall weaker at solstice. Since the largest diurnal variation amplitudes in the wind are located at different locations across the globe, large diurnal GW forcing coincides with some of these maxima. This causes the GW forcing in SD-WACCM to change the amplitude of the LT tidal winds more effectively than in eCMAM.

Fig. 5.4 is similar to Fig. 5.3 but in the meridional direction. Overall the diurnal GW forcing is very similar to the zonal direction with the forcings in eCMAM being much larger and SD-WACCM being similar. One consequence of the similarity in GW forcing in SD-WACCM is that the meridional wind amplitudes are mostly located at lower latitudes and thus are not as affected by the GWs as in the zonal direction. All other conclusions are the same in the meridional direction.

It should be noted that the figures for the LT diurnal GW variations can be used as an estimate of the GW affects on the tides as was done here. The Equivalent Rayleigh Friction can be calculated at all grid points in the model between the LT winds and GW forcing, but the locations of largest changes in tidal winds will be the same as the locations of largest
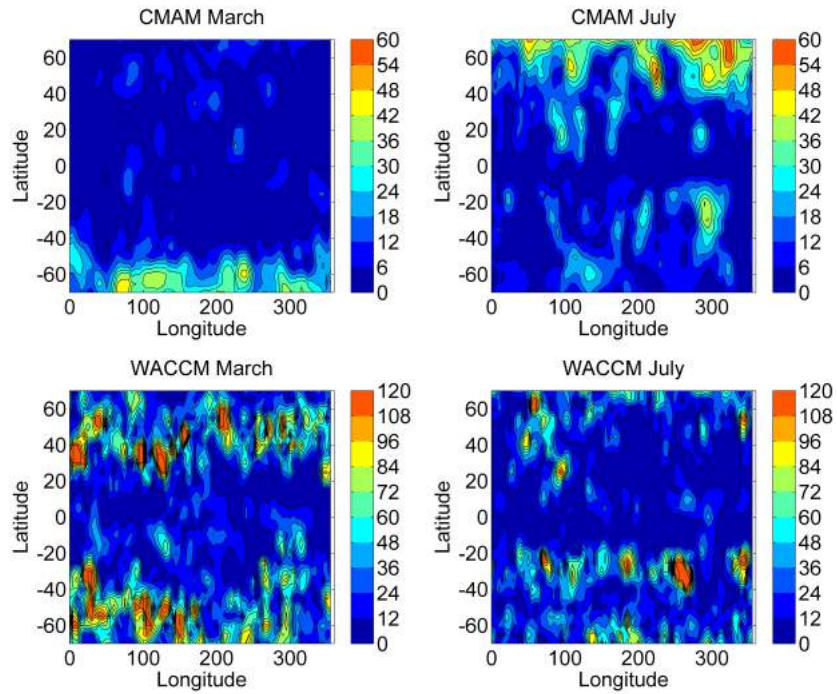
Figure 5.3: Local time zonal GW diurnal amplitudes of a diurnal phase aligned composite day for the month of March at 90km.
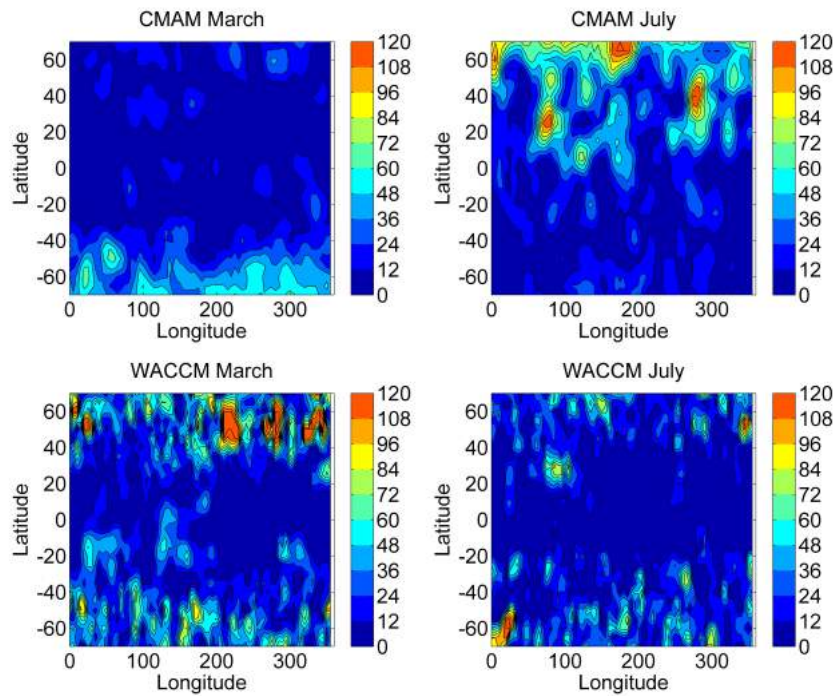

Figure 5.4: Local time meridional wind diurnal amplitudes of a diurnal phase aligned composite day for the month of March at 90km.

GW forcing. This is because smaller forcings do not have large enough amplitudes to affect the tidal winds.

5.3.2 Tidal Mode Contributions to Local Time Diurnal Variations: Winds

As described previously, the LT diurnal variations are a summation of one or more tidal modes above a particular location. It is not possible to separate these modes in observations but with GCM's a global picture may be obtained and the tidal modes most responsible for the LT variations determined. To do this, a zonal mean of the LT amplitudes is compared to the amplitudes of several thermal tide modes. This is shown in Fig. 5.5 with the top left plot being the zonal mean of the LT amplitudes at all altitudes and the others being westward diurnal tidal amplitudes with zonal wavenumbers 1-5. The eastward diurnal tidal amplitudes with zonal wavenumber 1-5 are shown in Fig. 5.6. These are for the zonal component of the winds in March in eCMAM. The meridional component is in the appendix along with the zonal and meridional components for July since the results are very similar.

According to the figures, the zonal mean of the LT diurnal amplitudes in March can reach up to 40 m/s at the mid latitudes around 90 km and is significant above and at the poles. Comparing this to the amplitudes of each tidal mode in both the eastward and westward directions it can be seen that the DW1 tidal structure is very similar. This means that the DW1 tide is most responsible for the LT diurnal variations. This explains the strong bands of LT amplitudes around $\pm 20°$ latitude in eCMAM in Fig. 5.1. The DW1 tides is strongest in this region of the globe and is the major component of the LT variations. The DW2 and DW3 tidal modes are the next strongest and seem to contribute at the equator but are dwarfed by DW1 at mid latitudes. The only section not explained by this tidal mode is the region above 100 km at the low to mid latitudes where DW1 is weak but the zonal mean LT variations are relatively strong. The only tidal mode to contribute to this region is the DE3 tide but it is only about 10 m/s and does not reach the 25-35 m/s seen in the zonal mean
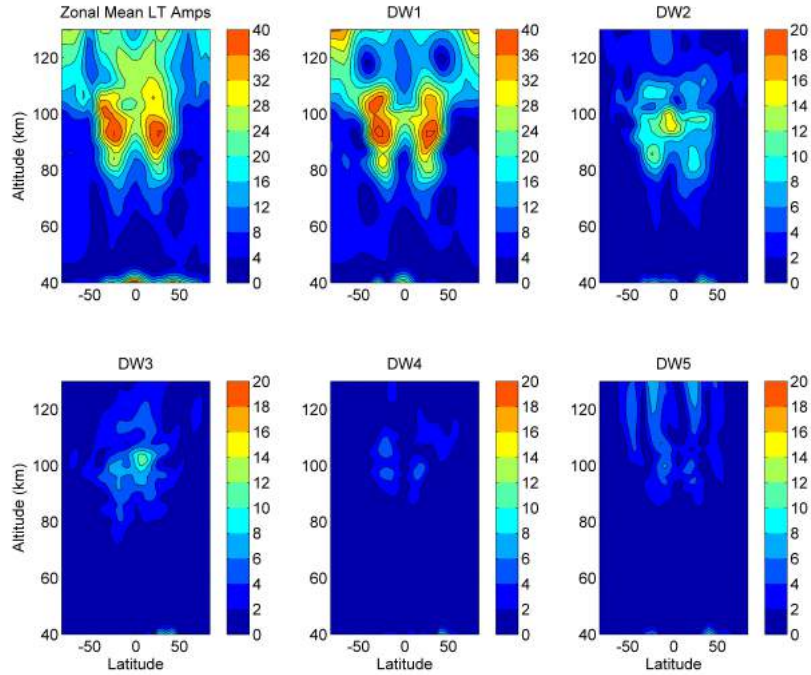
Figure 5.5: Zonal mean of the local time zonal wind diurnal amplitudes (top left) and the amplitudes of westward diurnal tide modes with wavenumbers 1-5 for March in eCMAM

amplitudes. The other tidal modes shown here are much weaker and do not contribute very much to the LT diurnal variations in eCMAM.

To help explain why the zonal mean LT diurnal variations near the equator above 100 km are stronger than any tidal mode, the horizontal structure of the LT wind amplitudes at 110 km is shown in Fig. 5.7. The thick black lines are guidelines for patterns in the amplitude peaks and is discussed below. At this altitude, there is a large region of diurnal variation amplitudes between 250° to 300° longitude and -20° and +40° latitude that is causing the larger zonal mean values. When tidal modes interact with each other the resultant horizontal structure can have one or more regions of maximum or minimum amplitudes that do not exactly match any of the tides. Aside from the largest region of amplitudes mentioned before, there are some other peaks at the mid to lower latitudes that also contribute to the large zonal mean values. Looking across longitudes, the peaks tend to occur in three main bands, shown by the thick black guidelines, indicating a wave with a zonal wavenumber of 3. While
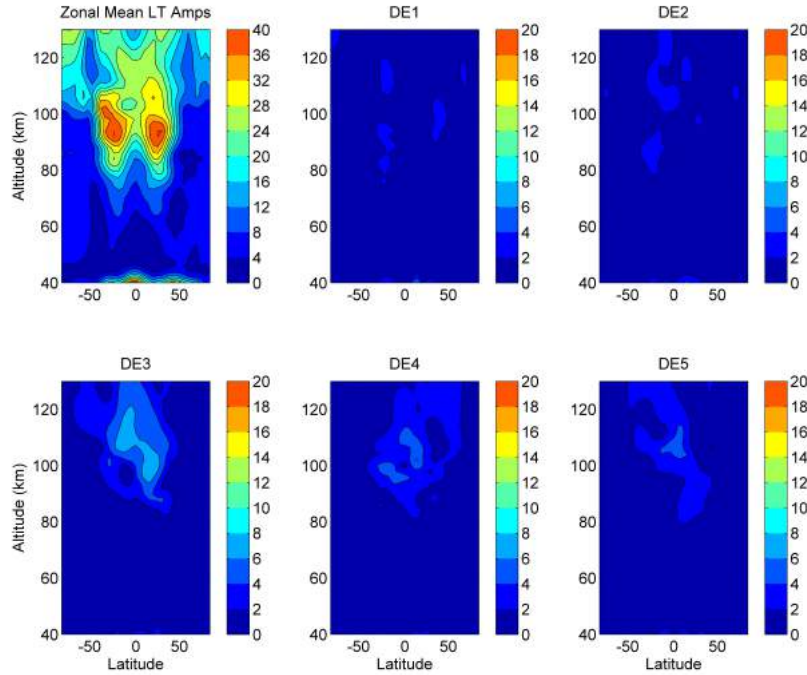
Figure 5.6: Zonal mean of the local time zonal wind diurnal amplitudes (top left) and the amplitudes of eastward diurnal tide modes with wavenumbers 1-5 for March in eCMAM

other modes may be modifying the horizontal structure of the LT variations causing the larger peaks and increasing the zonal mean, the DE3 tide is the largest contributor.

In Fig. 5.8, the zonal mean of the LT diurnal variations is shown in the top left plot and the amplitudes of the diurnal westward tides with wavenumbers 1-5 is in the remaining plots for March in SD-WACCM. The same is shown in Fig. 5.9 but for the eastward diurnal tidal modes. Similar to eCMAM the DW1 mode is the largest contributor to the LT variations but is not as dominant here. The DW2, DE3 and DE4 modes are also large contributors but not the DW3 as in eCMAM. At the southern mid latitudes between 80 and 100 km, the DW1 amplitudes do not especially match the zonal mean LT amplitudes but are much closer when also considering the DW2 tides. Since the GWs tend to suppress the DW1 amplitudes more in SD-WACCM, other tidal modes are able to exert larger influences on the local diurnal variations.
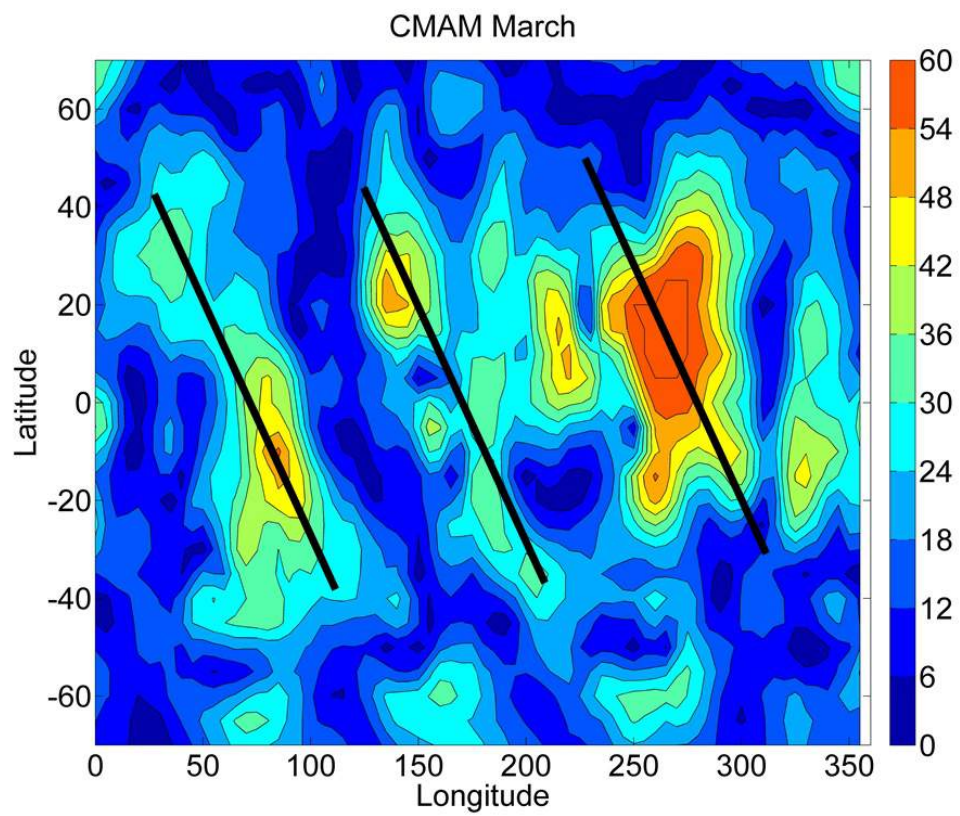
Figure 5.7: Local time zonal wind diurnal amplitudes of a diurnal phase aligned composite day for the month of March at 110km.
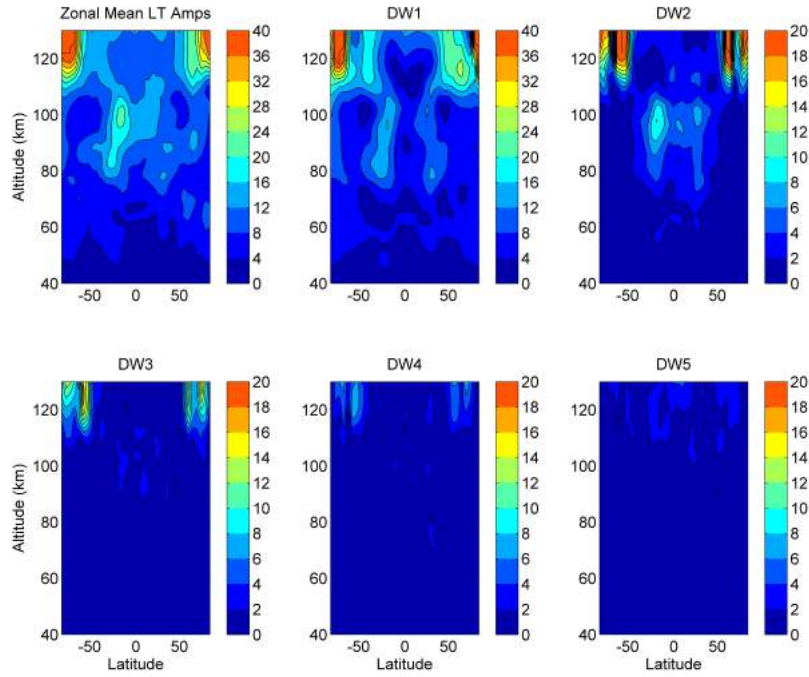
Figure 5.8: Zonal mean of the local time zonal wind diurnal amplitudes (top left) and the amplitudes of westward diurnal tide modes with wavenumbers 1-5 for March in WACCM
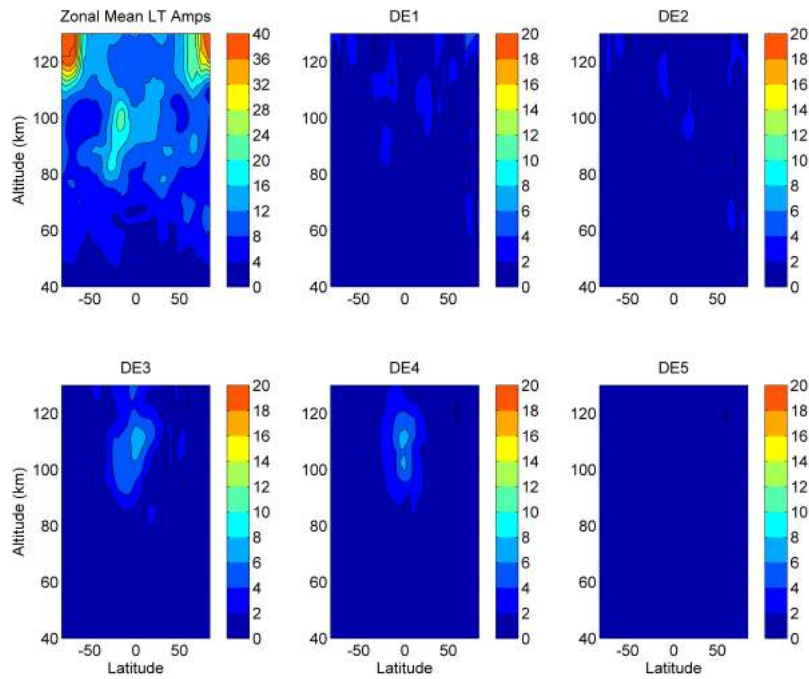

Figure 5.9: Zonal mean of the local time zonal wind diurnal amplitudes (top left) and the amplitudes of eastward diurnal tide modes with wavenumbers 1-5 for March in WACCM

5.3.3 Tidal Mode Contributions to Local Time Diurnal Variations: GW Forcing

With the contributions of tidal mode winds to the diurnal LT wind variations determined, the same can be found for the GWs in each model. Fig. 5.10 shows the zonal mean of the LT diurnal projection amplitudes of GW forcing in the top left plot while the five others show the tidal projections amplitudes for the westward tidal modes in eCMAM for the month of March. The eastward modes are shown in Fig. 5.11. The vast majority of the LT diurnal GW amplitudes are located at the southern pole between 80 km and 120 km. Some weaker GW forcing is also located at the northern pole and at some lower latitudes. This is reversed at the September equinox. The same situation occurs in the DW1 GW projections similar to the winds indicating the DW1 projections are again the dominant component to the LT variations. The other tidal mode projections are also located at the poles but are drowned out by DW1. While GWs in eCMAM are highly modulated by the tide, as shown in chapter 4, the magnitude of the diurnal component is much larger where DW1 is somewhat weaker. This is because the majority of the non-tidal projections of GW forcing is located at the poles and is much weaker where the tides are stronger as seen in Fig. 5.12 which shows the monthly mean of the GW forcing for March in eCMAM.

The zonal mean GW LT diurnal variation amplitudes are shown in the top left plot of Fig. 5.13 in March for SD-WACCM. The westward tidal projection amplitudes of the GW forcing are in the remaining plots with the eastward tidal projections in Fig. 5.14. Once again the DW1 component accounts for a large amount of the LT variations but here the other tidal components are also significant. While not as strong as DW1, nearly all the other tidal projections shown here reach comparable amplitudes. The zonal mean LT GW amplitudes are quite large at mid to higher latitudes which is not explained by a single tidal mode. Instead all of the GW projections onto the tidal modes contribute to the local diurnal variations. This is in direct contrast to the tidal projections of GW forcing in eCMAM.
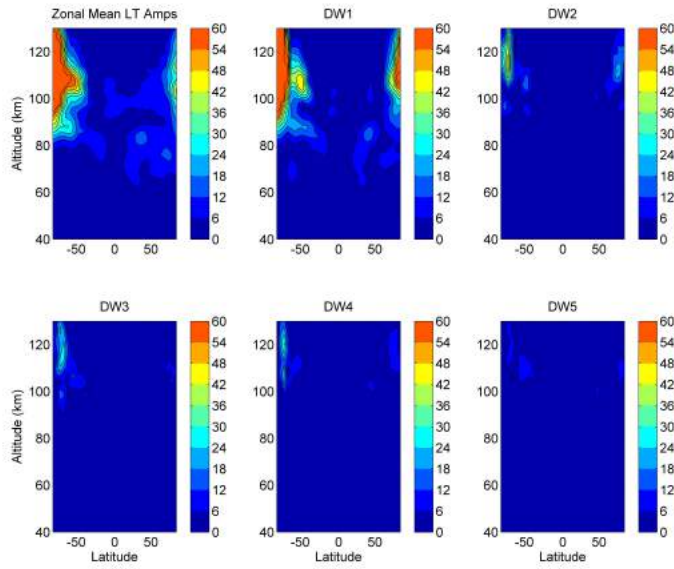
Figure 5.10: Zonal mean of the local time zonal GW diurnal amplitudes (top left) and the amplitudes of westward diurnal tide mode projections with wavenumbers 1-5 for March in eCMAM
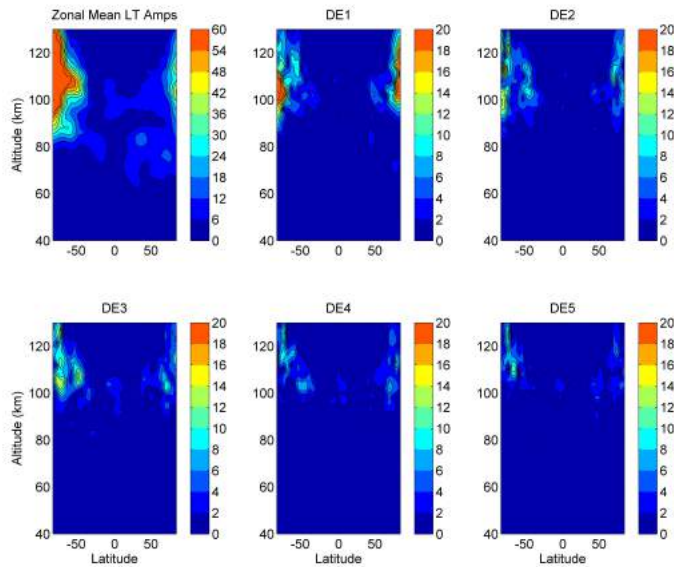

Figure 5.11: Zonal mean of the local time zonal GW diurnal amplitudes (top left) and the amplitudes of eastward diurnal tide mode projections with wavenumbers 1-5 for March in eCMAM
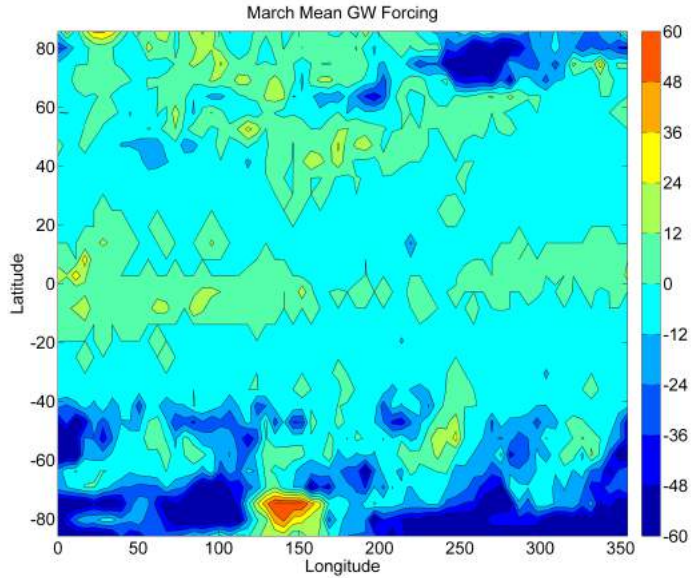
Figure 5.12: Monthly mean GW forcing at 110 km for March in eCMAM.

To explain why this happens in SD-WACCM and not in eCMAM it is useful to recall how the GW forcing is calculated in each parameterization scheme. In the Hines scheme used by eCMAM, a spectrum of GWs is always present in the atmosphere. At each altitude and horizontal location, the spectrum is recalculated based upon the background wind conditions and waves with a large wavenumber are obliterated from the spectrum depositing their momentum and energy into the background. This creates a high amount of modulation by the winds and because the DW1 tide is so dominant, a large amount of modulation by the DW1 tide. This also appears in the LT diurnal variations as seen above.

In the Lindzen scheme used by SD-WACCM, the location of GW forcing depends on the source region in the troposphere having almost nothing to do with the winds in the mesosphere or thermosphere. If the conditions do not activate the GW trigger functions, there is no GW forcing at all in the altitudes above. When calculating the diurnal projections for the winds and GW forcing, a Fourier transform was used which uses a summation of sines to calculate wave amplitudes and phases. Due to the GW forcing locations not being modulated by the background winds, of which the tides are a major feature, the GWs do
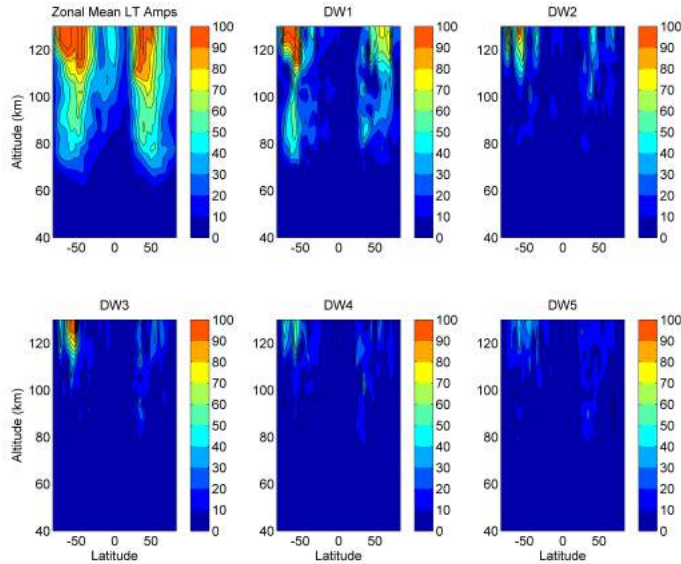
103

Figure 5.13: Zonal mean of the local time zonal GW diurnal amplitudes (top left) and the amplitudes of westward diurnal tide mode projections with wavenumbers 1-5 for March in WACCM

not have a strong tidal component projection. Instead the GW forcing is in effect spread out across all wave frequencies and wavenumbers. Due to this effect most tidal modes will be damped by the GWs, not just the largest amplitude ones like in eCMAM.

5.4 Conclusion

A major difficulty in relating observations with GCM's tidal results is that the observational data from a single ground based location cannot separate out tidal modes from the resultant diurnal variations. A model on the other hand can give the entire wind structure of the atmosphere allowing for deconstruction into individual modes. In this chapter the local diurnal variations and the global tidal modes in the eCMAM and SD-WACCM GCMs are calculated. By comparing the zonal mean LT variations with the tidal mode amplitudes the contribution of each mode to the local wind fluctuations was determined. The DW1 tidal mode is the most dominant in both models and is overpowering all other tidal modes in eCMAM. The DW1 tide is still the strongest contributor in SD-WACCM but since the
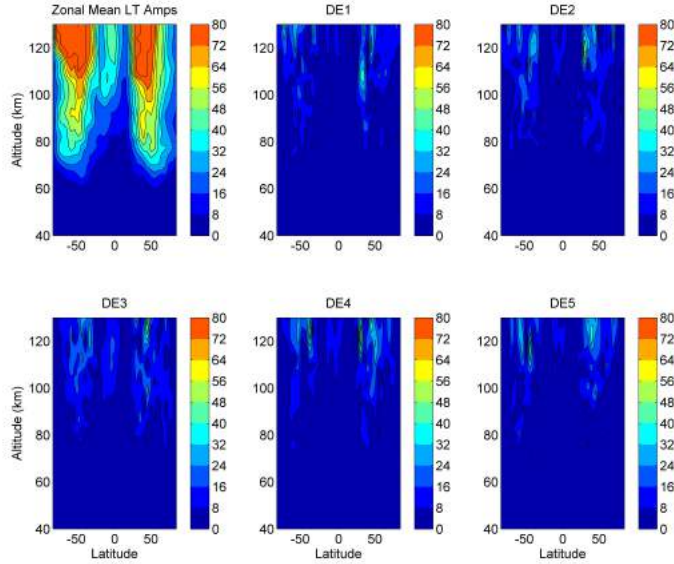
Figure 5.14: Zonal mean of the local time zonal wind diurnal amplitudes (top left) and the amplitudes of eastward diurnal tide mode projections with wavenumbers 1-5 for March in WACCM

GWs tend to suppress it more than in eCMAM, other modes such as the DW2 and DE3 tides become larger contributors to the LT variations.

For the GWs, the DW1 projection is by far the strongest contributor to the LT variation projections in eCMAM. This is because the Hines scheme allows for a high degree of modulation of the GWs by the background winds and thus the tides. Since the DW1 tidal winds are so dominant, the largest most influential tidal mode projection is the DW1 projection. A very different situation occurs in SD-WACCM. In the Lindzen scheme used by this model, the time and location of GW forcing is only dependent on the tropospheric sources and not the winds at mesospheric and tropospheric heights. This does not allow for the GW forcing to be modulated very much by the tides resulting in a spreading of the GW energy across many tidal modes. The other tidal modes in SD-WACCM undergo larger damping compared to eCMAM by the GWs because of this difference in paramterization schemes.

Chapter 6

Summary and Conclusions

GWs and tides are two important dynamical features of the atmosphere transporting momentum and energy thus creating a coupling process from the lower to the upper atmosphere. They also interact with various other atmospheric dynamics including each other. In this dissertation, assumptions used in GW parameterization schemes and their effects on the tides are investigated. Observations of GW-tide interactions from a LIDAR and a meteor radar are also analyzed, providing information to better constrain these parameterization schemes.

Observations of the GW-tide interactions are presented in chapter 3. A LIDAR stationed at the Starfire Optical Range and a meteor radar in Chile were used to calculate the background winds, the GW momentum fluxes, and the GW forcing on the diurnal variations in the winds. The LIDAR found strong modulations of the momentum fluxes by the diurnal variations in both the zonal and meridonal directions. The GWs either damped or amplified the tidal amplitudes depending on the phase difference between the tides and the GW forcing. The phase of the tide is delayed at all altitudes in both directions. These results compare well with models which do not use parameterization schemes. The Chile meteor radar also observed GW momentum flux modulations by the diurnal variations. From this instrument, the GWs mostly increased the amplitudes of the diurnal variations and either delayed or advanced its phase which is in contrast to the LIDAR results but very similar

to previous meteor radar results. It has been noted that the background winds calculated with LIDARs and meteor radars are very similar indicating the differences here are mainly from the derivation of GW momentum fluxes and forcings. The dissimilarities are due to the amount of averaging the radar has to use compared to the LIDAR and the observable areas available to each. The LIDAR only detects densities, temperatures and winds in a small section of sky overhead and can directly observe shorter period GWs. Meteor radars require all-sky averaging over many weeks to obtain reliable estimates of GW momentum fluxes which include both large and small scale wave variations.

Chapter 4 analyzes the affects of parameterization schemes on the DW1 tide in two separate GCMs each containing different schemes for parametrizing GWs. The eCMAM which uses the Hines Dopplar Spread scheme (*Hines*, 1997) and the SD-WACCM which uses a modified Lindzen scheme (*Conley et al.*, 2012) are used. The DW1 tidal amplitudes in the eCMAM model were found to be over double the amplitudes in the SD-WACCM in both the zonal and meridional directions and across seasons indicating the mechanism causing the differences is inherent in the models and not a dynamical process. The DW1 projection of the GW forcing calculated from the parameterization schemes is shown to mostly occur at higher latitudes away from the peaks in the DW1 tide in the eCMAM. The GW forcing peaks in SD-WACCM on the other hand were found to be at both higher and mid latitudes near where the tide is stronger. Both schemes almost always damped the tides while observations showed a mix of damping and enhancements. Since the tides are a major component of the winds, the GW affects on the non-tidal winds are also investigated. It is shown that GW forcing in the Hines scheme is only strong in certain latitude ranges and is severely modulated by the diurnal variations in the winds. This behavior is due to the assumption that only smaller scale waves break after which they are obliterated from the GW spectrum. In addition, the background winds change the spectrum as it is assumed to propagate creating a high degree of modulation in the GW forcing while also making it 90° out of phase from the tide on average. This does not create enough damping to properly

constrain the tides. The GW forcing from the Lindzen scheme does not show a large amount of modulation because the time and location of the forcing only depends on tropospheric sources. The forcing is also much larger and over a much larger range of altitudes because all waves in this scheme are assumed to become saturated. The larger accelerations from the GWs creates more substantial damping of the winds.

Chapter 5 focuses on GW-tidal interactions on a local time instead of a global scale in the GCMs. The local GW forcing in eCMAM has a strong seasonal dependence with the vast majority of the diurnal projections of GW forcing at the winter pole at equinox away from the largest diurnal variations limiting their affect. This seasonal dependence is not as strong in SD-WACCM with the forcings concentrated in both hemispheres around the mid latitudes at locations where the diurnal variations peak damping them. One advantage of using GCMs is that they can give a global picture of the local time variations in the winds. This is compared against the tidal mode amplitudes to determine which tidal modes contribute most to the local diurnal variations. The DW1 mode in the winds was found to be the largest contributor in both models and is dominant in eCMAM. The Hines GW parameterization scheme does not dampen the DW1 tide enough causing it to overpower all other tidal modes. In SD-WACCM, DW1 is over damped such that other modes are of comparable amplitudes allowing their contributions to the local diurnal variations to become larger. The DW1 projection of GW forcing in eCMAM is again dominant over other tidal mode projections due to the significant modulation by the DW1 winds. This is very different in SD-WACCM where most tidal modes have large contributions to the local time diurnal GW forcing variations. The reason this occurs is that the time and location of GW forcing in SD-WACCM depends on tropospheric sources and are not highly modulated by the tidal winds.

6.1   Future Work

Extensions to this investigation can occur in two major areas. The first is more observations of the GW-tidal interactions. While there has been previous studies on this subject, including the one here, consistent and reliable observations are lacking. These are crucial in furthering our understanding of this important process. The second area for furthering this work is in modifying GW parameterization schemes in GCMs. While computational constraints to directly simulating GWs in these models are becoming less relevant, parameterization schemes are still needed in the foreseeable future. One way to possibly recreate more realistic tidal modes in eCMAM is to increase the cutoff frequency in the Hines parameterization scheme so that larger scale waves can also force the background winds. In the Lindzen scheme, the phase speed spectrum can be either widened or narrowed reducing the overall forcing. The main challenge here would be maintaining internal model consistency with these modifications.

The next major step in improving all GW parameterization schemes would be to include horizontal propagation of the waves into the schemes. Recently, *Ribstein et al.* (2015) studied GW-tidal interactions in a linear tidal model using 4-D ray tracing for the GWs finding that the single column approximations currently used in parameterization schemes significantly overestimate GW fluxes leading to underestimated tidal amplitudes. These ray tracing techniques may be applied into future parameterization schemes to more accurately reproduce the tides.
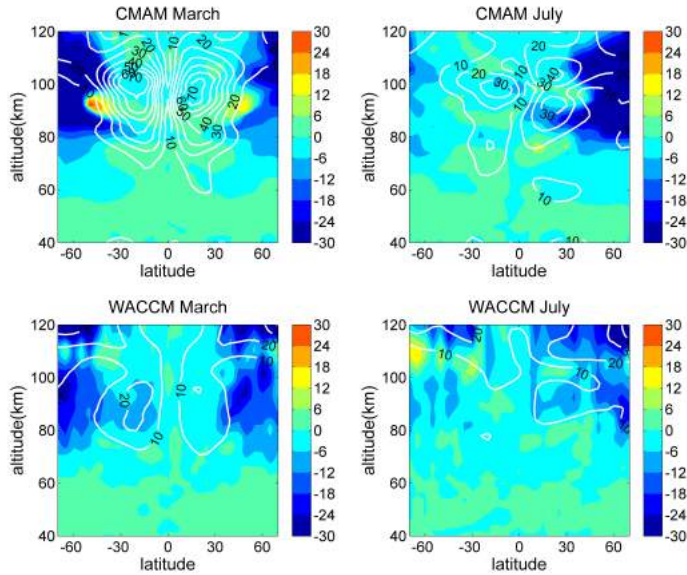
Appendix A

Chapter 4 Supplemental Figures

Figure A.1: Meridional DW1 wind amplitude change rate (m/s/day) (colors) due to DW1 projection of GW forcing and DW1 tidal winds (contours). The tidal contours are in increments of 10 m/s. The left plots are for March, the right for July, the top plots are for CMAM and the bottom are WACCM.
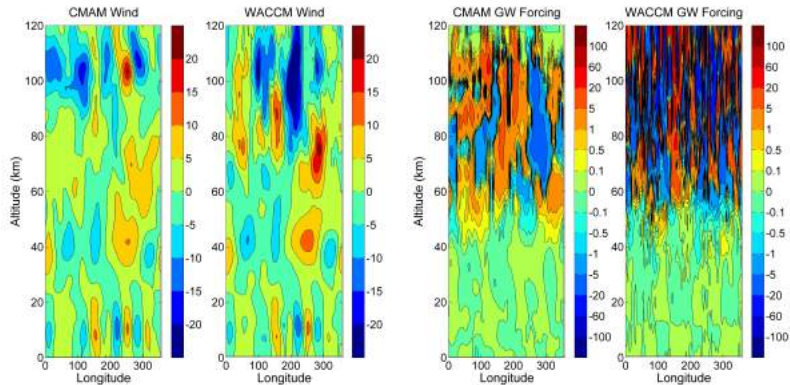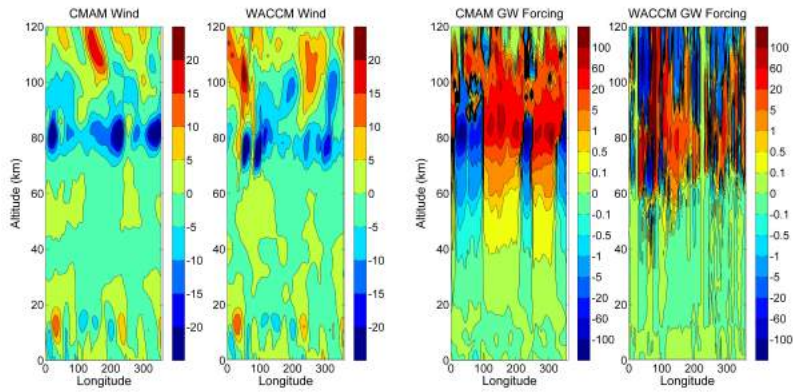

Figure A.2: Monthly mean meridional wind (m/s) (left plots) and GW forcing (m/s/day) (right plots) in CMAM (first and third plots) and WACCM (second and fourth plots) at 35° latitude in March. An uneven color scale is used to show smaller scale variations in the GW forcing.

Figure A.3: Monthly mean Meridional wind (m/s) (left plots) and GW forcing (m/s/day) (right plots) in CMAM (first and third plots) and WACCM (second and fourth plots) at 35° latitude in July. An uneven color scale is used to show smaller scale variations in the GW forcing.
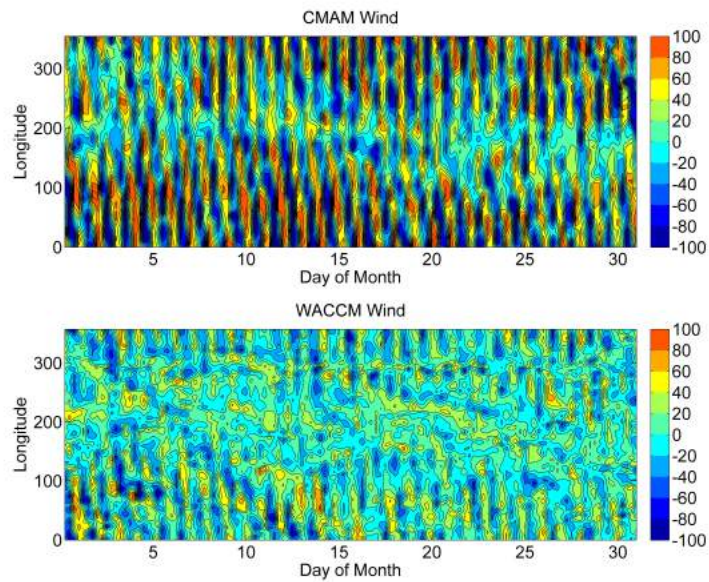
Figure A.4: Meridional wind (m/s) in CMAM (top) and WACCM (bottom) at -25° latitude and 92km in March
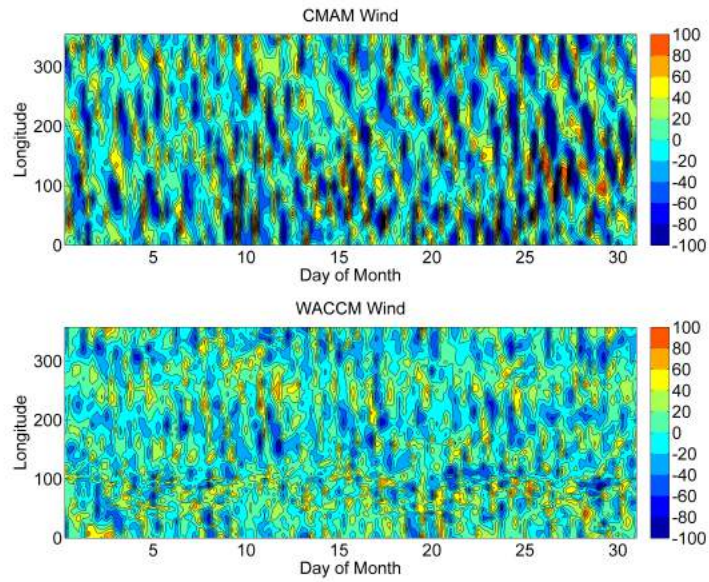
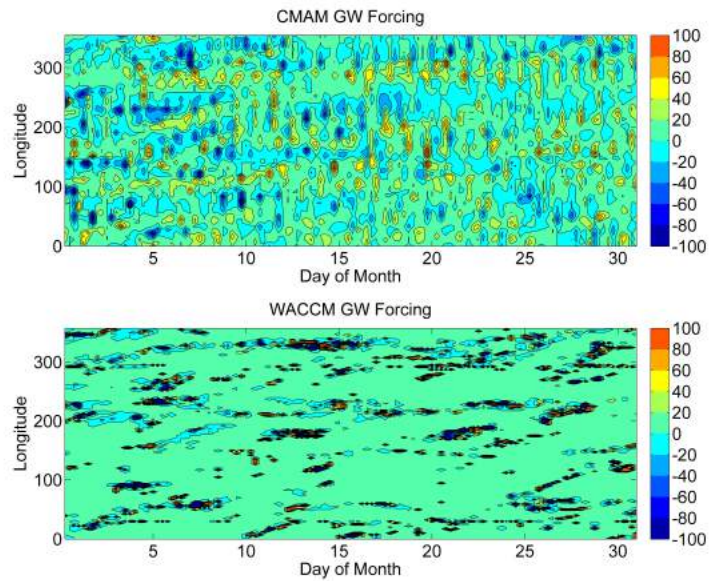Figure A.5: Meridional wind (m/s) in CMAM (top) and WACCM (bottom) at 30° latitude and 95km in July

Figure A.6: Meridional GW forcing (m/s/day) in CMAM (top) and WACCM (bottom) at -30° latitude and 80km in March
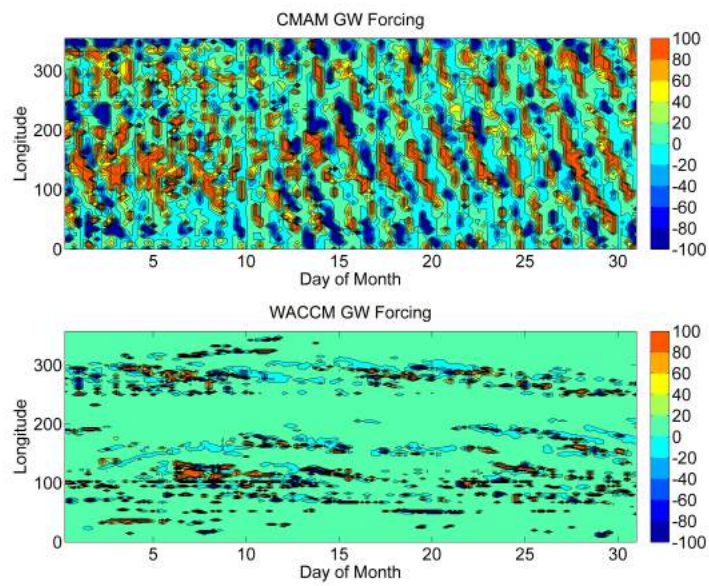
Figure A.7: Meridional GW forcing (m/s/day) in CMAM (top) and WACCM (bottom) at 30° latitude and 85km in July

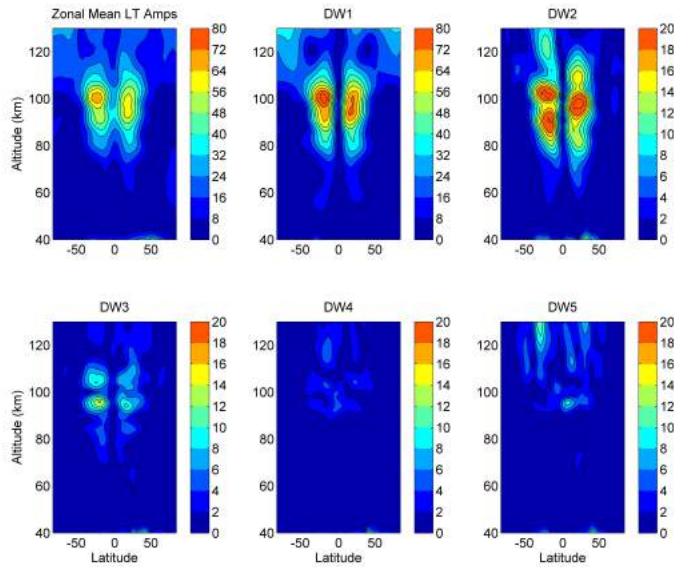# Appendix B

Chapter 6 Supplemental Figures

Figure B.1: Zonal mean of the local time meridional wind diurnal amplitudes (top left) and the amplitudes of westward diurnal tide modes with wavenumbers 1-5 for March in eCMAM
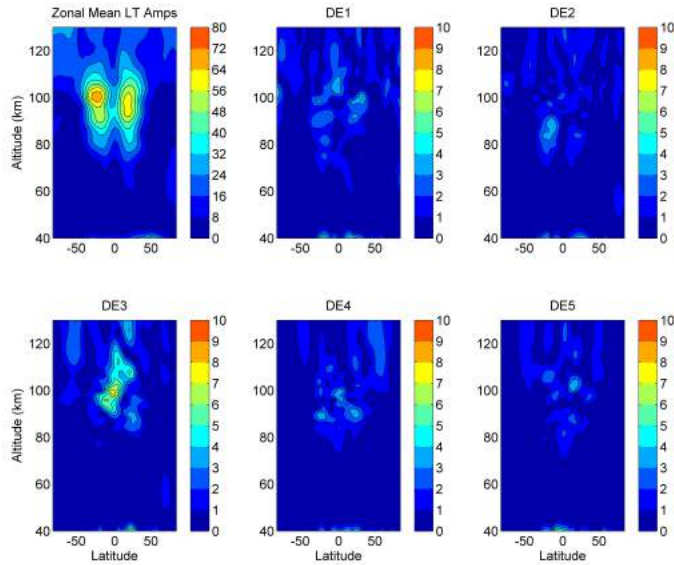

Figure B.2: Zonal mean of the local time meridional wind diurnal amplitudes (top left) and the amplitudes of eastward diurnal tide modes with wavenumbers 1-5 for March in eCMAM
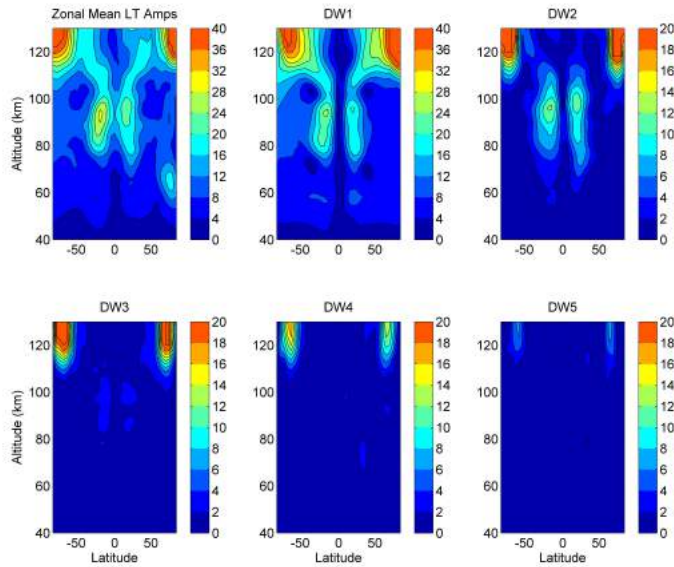
Figure B.3: Zonal mean of the local time meridional wind diurnal amplitudes (top left) and the amplitudes of westward diurnal tide modes with wavenumbers 1-5 for March in WACCM
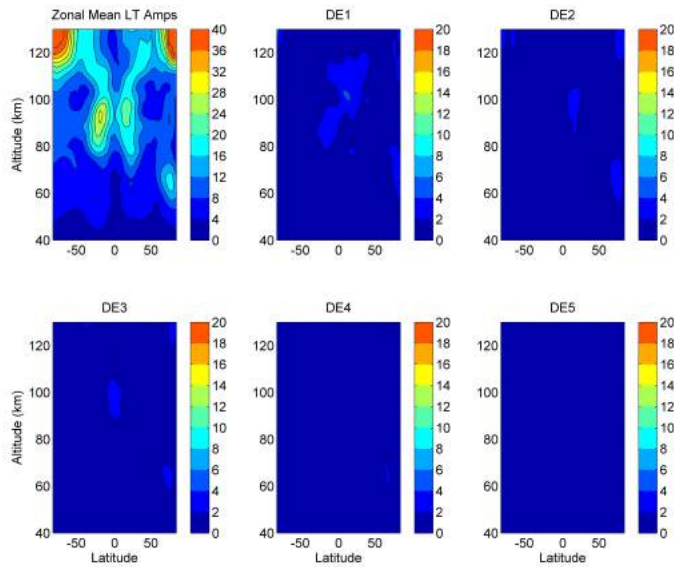

Figure B.4: Zonal mean of the local time meridional wind diurnal amplitudes (top left) and the amplitudes of eastward diurnal tide modes with wavenumbers 1-5 for March in WACCM
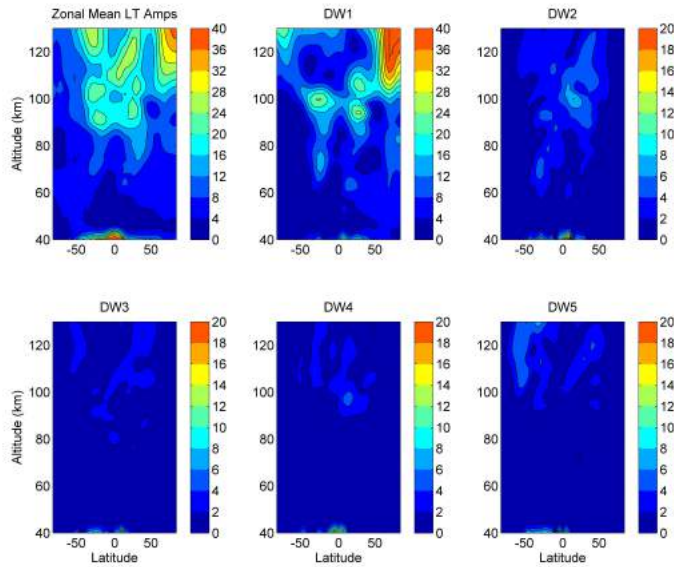
Figure B.5: Zonal mean of the local time zonal wind diurnal amplitudes (top left) and the amplitudes of westward diurnal tide modes with wavenumbers 1-5 for July in eCMAM
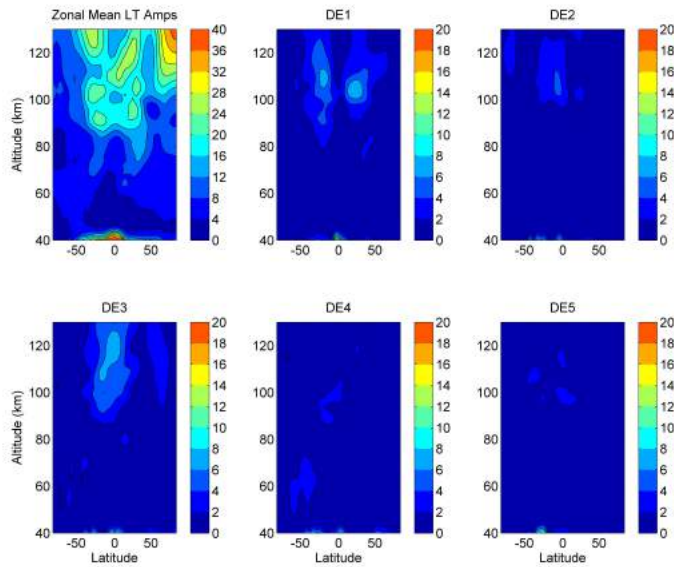

Figure B.6: Zonal mean of the local time zonal wind diurnal amplitudes (top left) and the amplitudes of eastward diurnal tide modes with wavenumbers 1-5 for July in eCMAM

Figure B.7: Zonal mean of the local time zonal wind diurnal amplitudes (top left) and the amplitudes of westward diurnal tide modes with wavenumbers 1-5 for July in WACCM
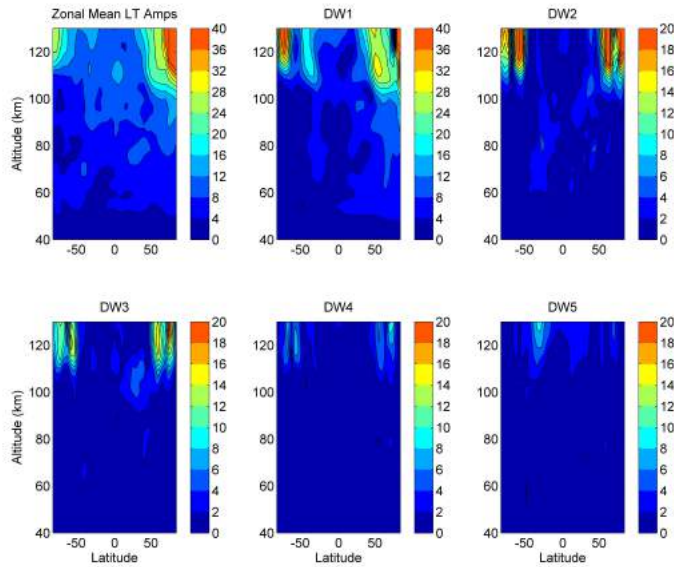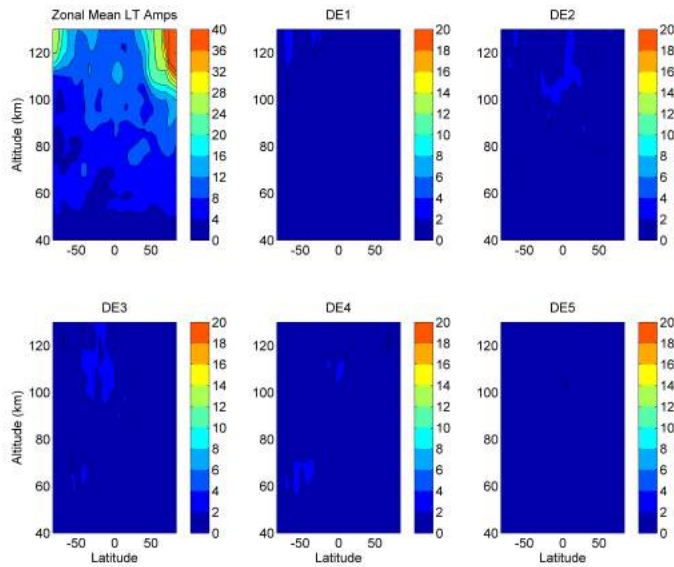

Figure B.8: Zonal mean of the local time zonal wind diurnal amplitudes (top left) and the amplitudes of eastward diurnal tide modes with wavenumbers 1-5 for July in WACCM

Figure B.9: Zonal mean of the local time meridional wind diurnal amplitudes (top left) and the amplitudes of westward diurnal tide modes with wavenumbers 1-5 for July in eCMAM

Figure B.10: Zonal mean of the local time meridional wind diurnal amplitudes (top left) and the amplitudes of eastward diurnal tide modes with wavenumbers 1-5 for July in eCMAM
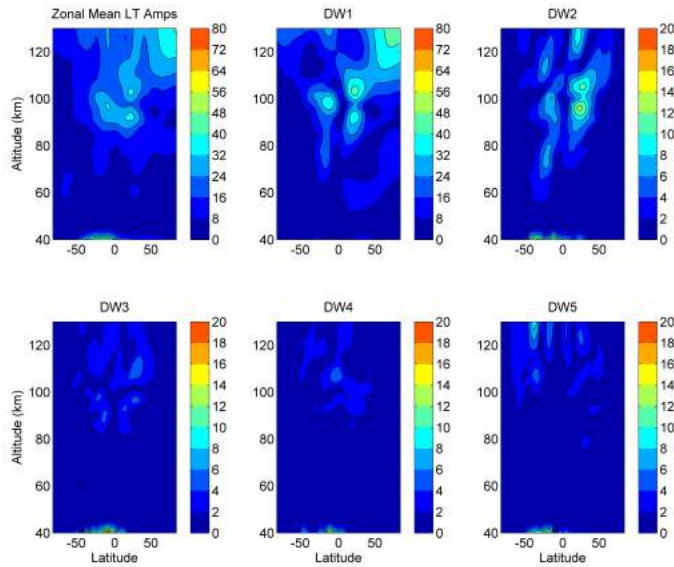
Figure B.11: Zonal mean of the local time meridional wind diurnal amplitudes (top left) and the amplitudes of westward diurnal tide modes with wavenumbers 1-5 for July in WACCM
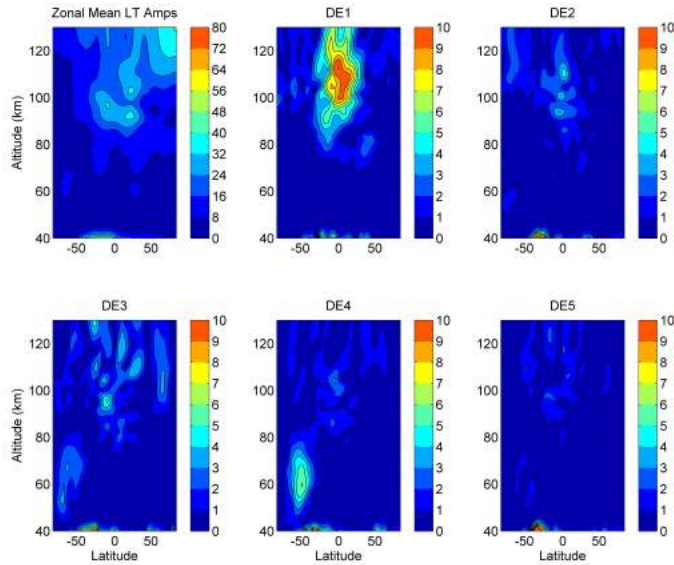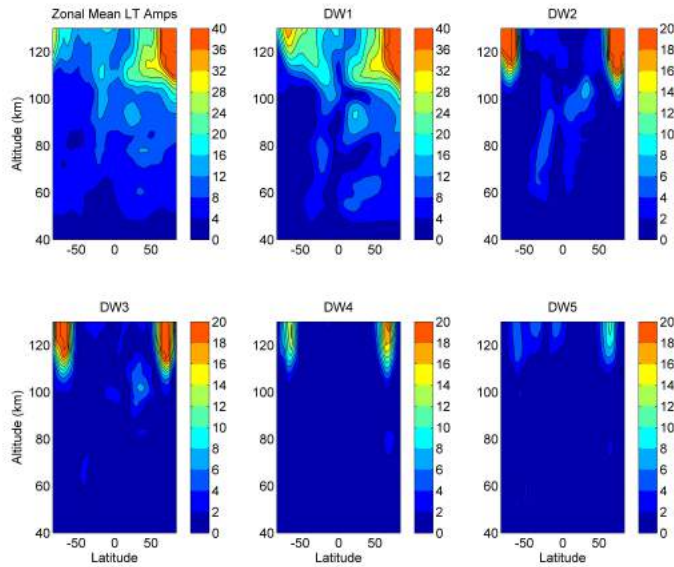

Figure B.12: Zonal mean of the local time meridional wind diurnal amplitudes (top left) and the amplitudes of eastward diurnal tide modes with wavenumbers 1-5 for July in WACCM

Figure B.13: Zonal mean of the local time meridional GW diurnal amplitudes (top left) and the amplitudes of westward diurnal tide mode projections with wavenumbers 1-5 for March in eCMAM

Figure B.14: Zonal mean of the local time meridional GW diurnal amplitudes (top left) and the amplitudes of eastward diurnal tide mode projections with wavenumbers 1-5 for March in eCMAM

Figure B.15: Zonal mean of the local time meridional GW diurnal amplitudes (top left) and the amplitudes of westward diurnal tide mode projections with wavenumbers 1-5 for March in WACCM
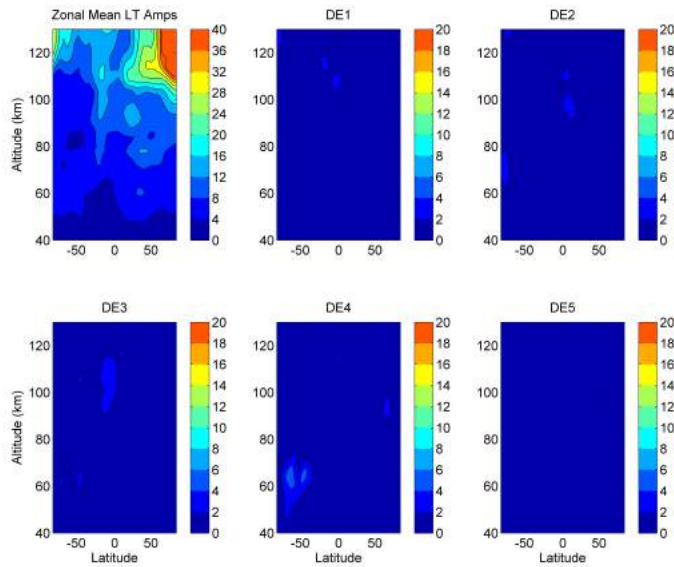

Figure B.16: Zonal mean of the local time meridional GW diurnal amplitudes (top left) and the amplitudes of eastward diurnal tide mode projections with wavenumbers 1-5 for March in WACCM
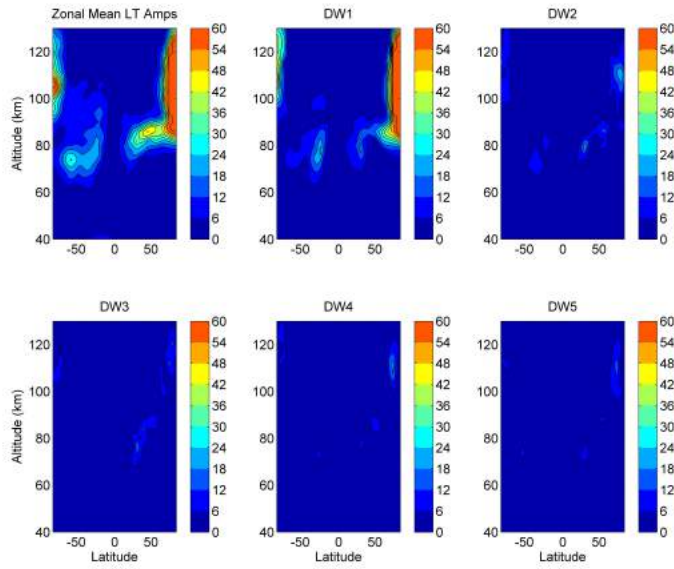
Figure B.17: Zonal mean of the local time zonal GW diurnal amplitudes (top left) and the amplitudes of westward diurnal tide mode projections with wavenumbers 1-5 for July in eCMAM
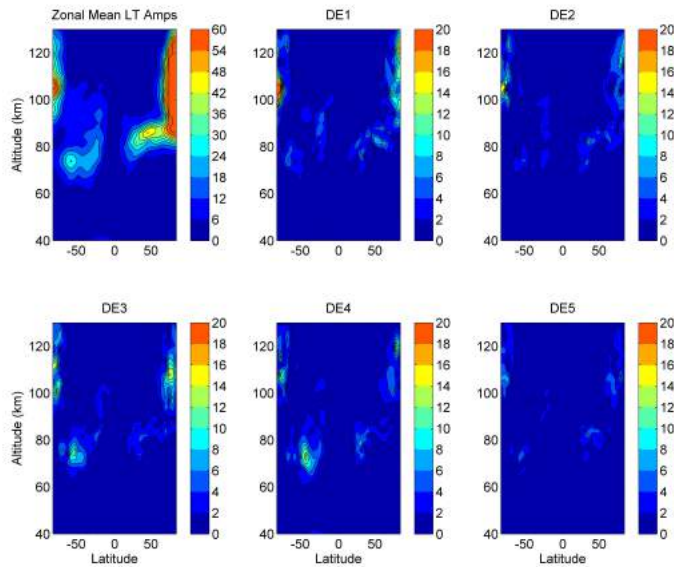
Figure B.18: Zonal mean of the local time zonal GW diurnal amplitudes (top left) and the amplitudes of eastward diurnal tide mode projections with wavenumbers 1-5 for July in eCMAM
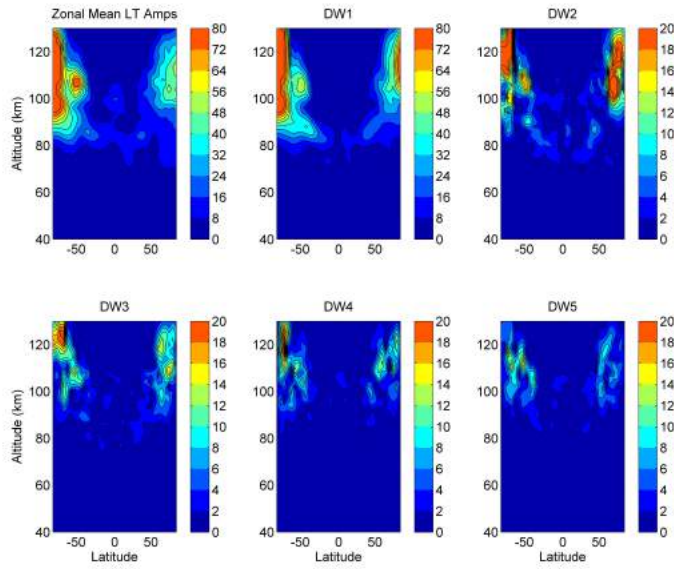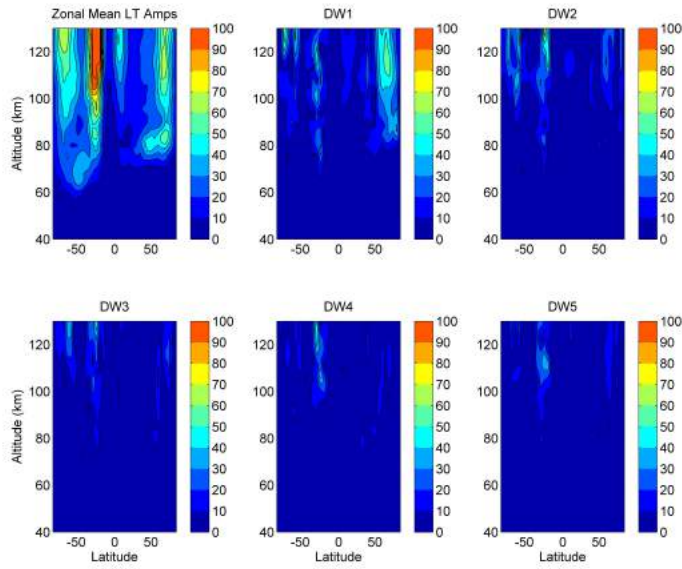
Figure B.19: Zonal mean of the local time zonal GW diurnal amplitudes (top left) and the amplitudes of westward diurnal tide mode projections with wavenumbers 1-5 for July in WACCM
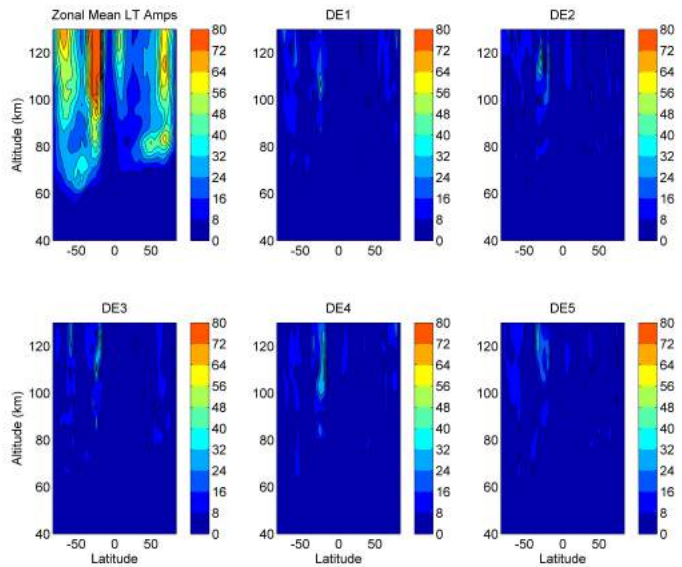
Figure B.20: Zonal mean of the local time zonal GW diurnal amplitudes (top left) and the amplitudes of eastward diurnal tide mode projections with wavenumbers 1-5 for July in WACCM
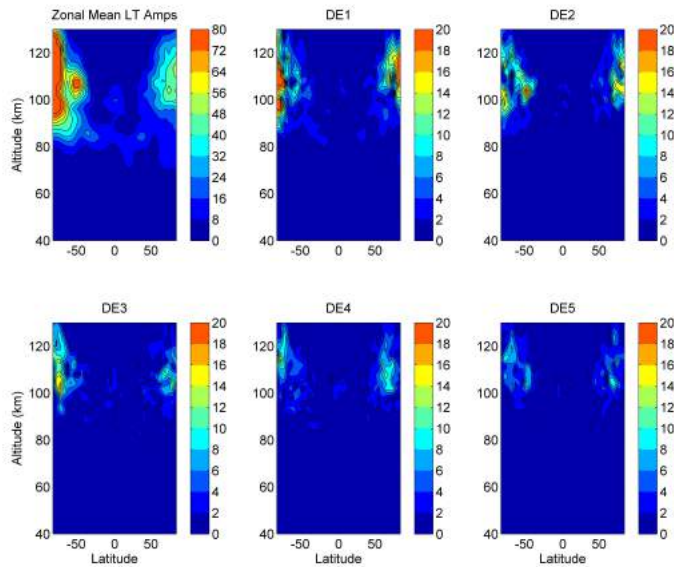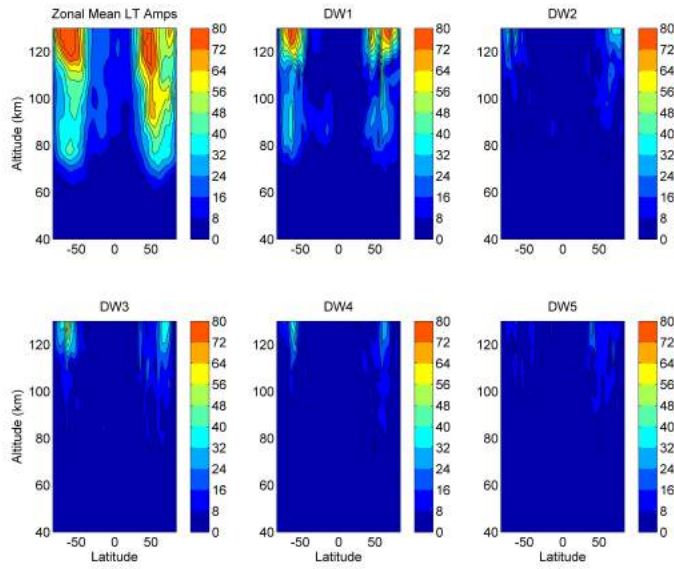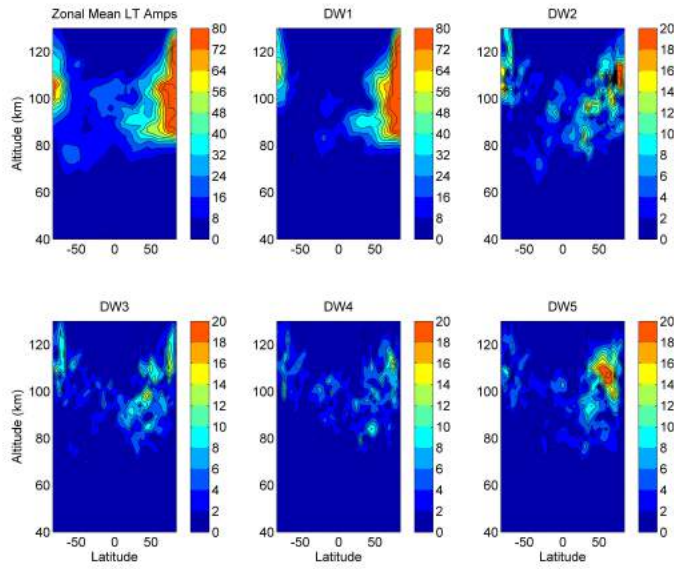
Figure B.21: Zonal mean of the local time meridional GW diurnal amplitudes (top left) and the amplitudes of westward diurnal tide mode projections with wavenumbers 1-5 for July in eCMAM
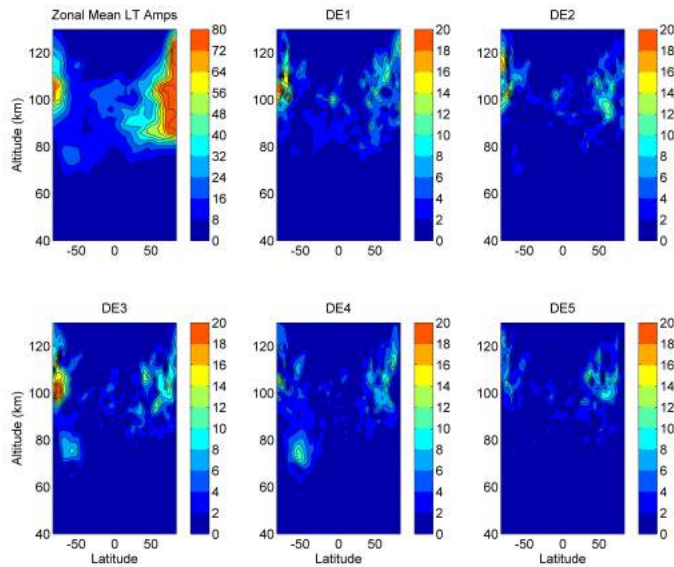
Figure B.22: Zonal mean of the local time meridional GW diurnal amplitudes (top left) and the amplitudes of eastward diurnal tide mode projections with wavenumbers 1-5 for July in eCMAM
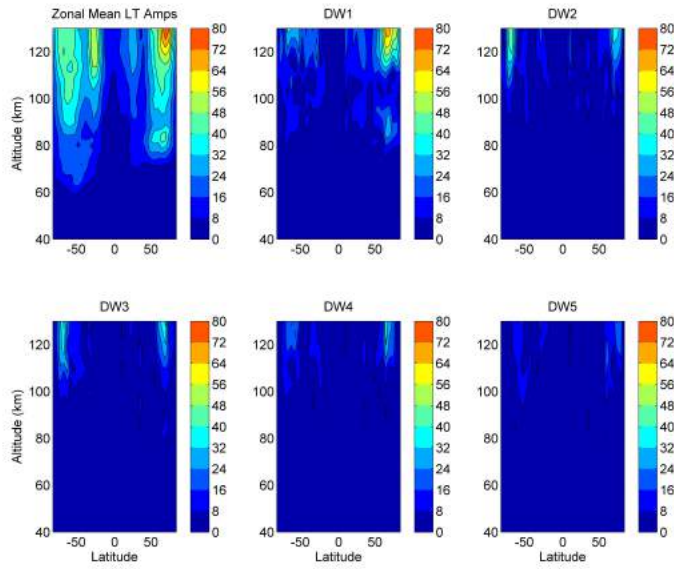
Figure B.23: Zonal mean of the local time meridional GW diurnal amplitudes (top left) and the amplitudes of westward diurnal tide mode projections with wavenumbers 1-5 for July in WACCM
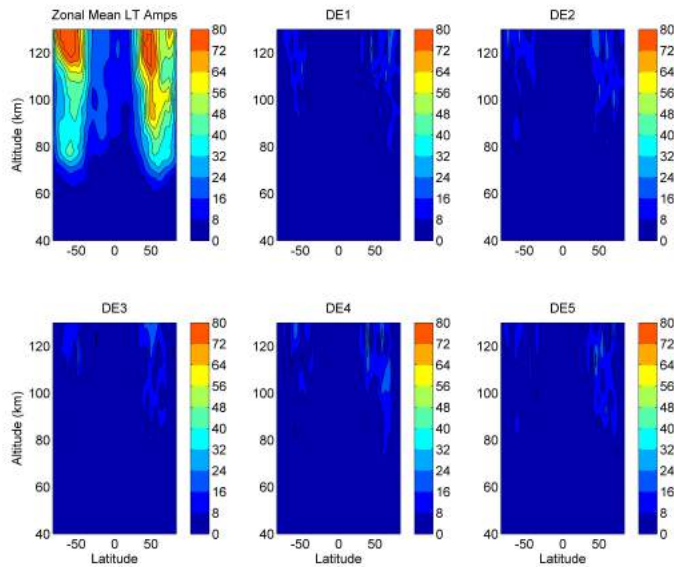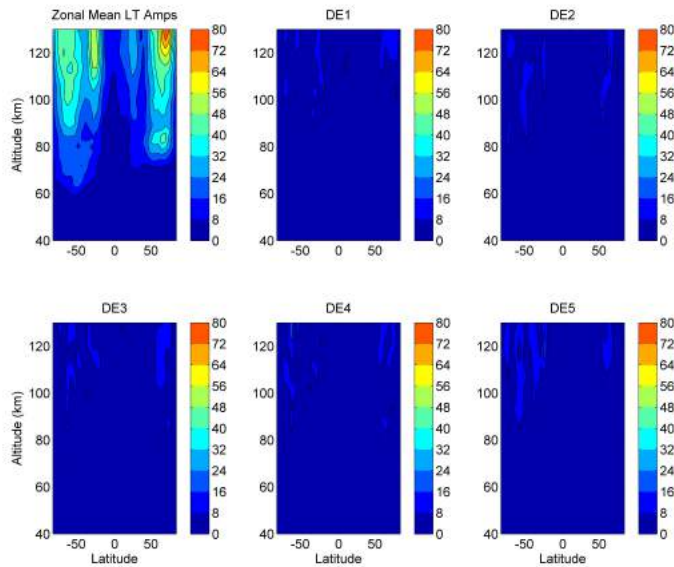

Figure B.24: Zonal mean of the local time meridional GW diurnal amplitudes (top left) and the amplitudes of eastward diurnal tide mode projections with wavenumbers 1-5 for July in WACCM

Bibliography

Acott, P. E., C.-Y. She, D. A. Krueger, Z.-A. Yan, T. Yuan, J. Yue, and S. Harrell (2011), Observed nocturnal gravity wave variances and zonal momentum flux in mid-latitude mesopause region over Fort Collins, Colorado, USA, *J. Atmos. Sol.-Terr. Phys.*, *73*(4), 449–456.

Agner, R., and A. Z. Liu (2015), Local time variation of gravity wave momentum fluxes and their relationship with the tides derived from lidar measurements, *Journal of Atmospheric and Solar-Terrestrial Physics*, *135*, 136–142.

Akmaev, R. (2006), Does the moon have a tidal effect on the atmosphere as well as the oceans?, *Scientifc American*.

Akmaev, R. A., T. J. Fuller-Rowell, F. Wu, J. M. Forbes, X. Zhang, A. F. Anghel, M. D. Iredell, S. Moorthi, and H.-M. Juang (2008), Tidal variability in the lower thermosphere: Comparison of whole atmosphere model (wam) simulations with observations from timed, *Geophysical Research Letters*, *35*(3), doi:10.1029/2007GL032584, l03810.

Alexander, M. J., and T. J. Dunkerton (1999), A spectral parameterization of mean-flow forcing due to breaking gravity waves, *J. Atmos. Sci.*, *56*(24), 4167–4182.

Alexander, M. J., S. D. Eckermann, D. Broutman, and J. Ma (2009), Momentum flux estimates for south georgia island mountain waves in the stratosphere observed via satellite, *Geophysical Research Letters*, *36*(12), n/a–n/a, doi:10.1029/2009GL038587, l12816.

Andrioli, V., P. Batista, B. Clemesha, N. Schuch, and R. Buriti (2015), Multi-year observations of gravity wave momentum fluxes at low and middle latitudes inferred by all-sky meteor radar, *Ann. Geophys*, *33*, 1183–1193.

Antonita, T. M., G. Ramkumar, K. K. Kumar, and V. Deepa (2008), Meteor wind radar observations of gravity wave momentum fluxes and their forcing toward the Mesospheric Semiannual Oscillation, *J. Geophys. Res.*, *113*, D10115, doi:10.1029/2007JD009089.

Bacmeister, J. T., M. R. Schoeberl, L. R. Lait, P. A. Newman, and B. Gary (1990), Er-2 mountain wave encounter over antarctica: Evidence for blocking, *Geophysical Research Letters*, *17*(1), 81–84, doi:10.1029/GL017i001p00081.

Baldwin, M. P., et al. (2001), The quasi-biennial oscillation, *Rev. Geophys.*, *39*(2), 179–229.

Beldon, C. L., and N. J. Mitchell (2010), Gravity wave-tidal interactions in the mesosphere and lower thermosphere over Rothera, Antarctica (68°S, 68°W), *J. Geophys. Res.*, *115*(D18), D18,101.

Burks, D., and C. Leovy (1986), Planetary waves near the mesospheric easterly jet, *Geophysical Research Letters*, *13*(3), 193–196, doi:10.1029/GL013i003p00193.

Chang, L., S. Palo, M. Hagan, J. Richter, R. Garcia, D. Riggin, and D. Fritts (2008), Structure of the migrating diurnal tide in the whole atmosphere community climate model (waccm), *Advances in Space Research*, *41*(9), 1398–1407.

Chang, L. C., S. E. Palo, and H.-L. Liu (2011), Short-term variability in the migrating diurnal tide caused by interactions with the quasi 2 day wave, *J. Geophys. Res.*, *116*(D12), D12,112.

Chapman, S., and R. S. Lindzen (1970), *Atmospheric Tides*, D. Reidel Publishing Company.

Conley, A. J., et al. (2012), Description of the ncar community atmosphere model (cam 5.0), *NCAR technical note*.

Crary, D. J., and J. M. Forbes (1983), On the extraction of tidal information from measurements covering a fraction of a day, *Geophysical Research Letters*, *10*(7), 580–582, doi:10.1029/GL010i007p00580.

Davis, R., J. Du, A. Smith, W. Ward, and N. Mitchell (2013), The diurnal and semidiurnal tides over ascension island (s, 14 w) and their interaction with the stratospheric quasi-biennial oscillation: studies with meteor radar, ecmam and waccm, *Atmospheric Chemistry and Physics*, *13*(18), 9543–9564.

Descloitres, J. (2003), Atmospheric gravity waves and internal waves off australia, `http://visibleearth.nasa.gov/view.php?id=69463`.

Eckermann, S. D., et al. (2009), High-altitude data assimilation system experiments for the northern summer mesosphere season of 2007, *Journal of Atmospheric and Solar-Terrestrial Physics*, *71*(3), 531–551.

Ejiri, M. K., M. J. Taylor, T. Nakamura, and S. J. Franke (2009), Critical level interaction of a gravity wave with background winds driven by a large-scale wave perturbation, *Journal of Geophysical Research: Atmospheres*, *114*(D18), n/a–n/a, doi:10.1029/2008JD011381, d18117.

England, S. L., A. Dobbin, M. J. Harris, N. F. Arnold, and A. D. Aylward (2006), A study into the effects of gravity wave activity on the diurnal tide and airglow emissions in the equatorial mesosphere and lower thermosphere using the Coupled Middle Atmosphere and Thermosphere (CMAT) general circulation model, *J. Atmos. Sol. -Terr. Phys.*, *68*, 293, doi:10.1016/j.jastp.2005.05.006.

Espy, P. J., G. O. L. Jones, G. R. Swenson, J. Tang, and M. J. Taylor (2004), Seasonal variations of the gravity wave momentum flux in the antarctic mesosphere and lower thermosphere, *J. Geophys. Res.*, *109*, D23109, doi:10.1029/2003JD004446.

Forbes, J. M., G. Jun, and M. Saburo (1991), On the interactions between gravity waves and the diurnal propagating tide, *Planetary and Space Science*, *39*(9), 1249–1257.

Forbes, J. M., X. Zhang, S. Palo, J. Russell, C. J. Mertens, and M. Mlynczak (2008), Tidal variability in the ionospheric dynamo region, *Journal of Geophysical Research: Space Physics*, *113*(A2), doi:10.1029/2007JA012737, a02310.

Forbes, M., J. (1995), *The Upper Mesosphere and Lower Thermosphere: A Review of Experiment and Theory*, chap. Tidal and Planetary Waves, pp. 67–88, American Geophysical Union.

Franke, S. J., X. Chu, A. Z. Liu, and W. K. Hocking (2005), Comparison of meteor radar and Na Doppler lidar measurements of winds in the mesopause region above Maui, Hawaii, *J. Geophys. Res.*, *110*, D09S02, doi:10.1029/2003JD004486.

Fritts, D. C., and M. J. Alexander (2003), Gravity wave dynamics and effects in the middle atmosphere, *Rev. Geophys.*, *41*(1), 1003, doi:10.1029/2001RG000106.

Fritts, D. C., and W. Lu (1993), Spectral estimates of gravity wave energy and momentum fluxes. Part II: Parameterization of wave forcing and variability, *J. Atmos. Sci.*, *50*(22), 3695–3713.

Fritts, D. C., and R. A. Vincent (1987), Mesospheric momentum flux studies at Adelaide, Australia: Observations and a gravity wave–tidal interaction model, *J. Atmos. Sci.*, *44*(3), 605–619.

Fritts, D. C., D. Janches, W. K. Hocking, N. J. Mitchell, and M. J. Taylor (2012), Assessment of gravity wave momentum flux measurement capabilities by meteor radars having different transmitter power and antenna configurations, *J. Geophys. Res.*

Gan, Q., J. Du, W. Ward, S. Beagley, V. I. Fomichev, and S. Zhang (2014), Climatology

of the diurnal tides from ecmam30 (1979 to 2010) and its comparison with saber, *Earth, Planets and Space, 66:103*.

Garcia, R. R., and S. Solomon (1985), The effect of breaking gravity waves on the dynamics and chemical composition of the mesosphere and lower thermosphere, *J. Geophys. Res.*, *90*(D2), 3850–3868.

Gardner, C. S., and A. Z. Liu (2007), Seasonal variations of the vertical fluxes of heat and horizontal momentum in the mesopause region at Starfire Optical Range, New Mexico, *J. Geophys. Res.*, *112*, D09113, doi:10.1029/2005JD006179.

Geller, M. A., et al. (2013), A comparison between gravity wave momentum fluxes in observations and climate models, *Journal of Climate*, *26*(17), 6383–6405.

Giorgetta, M. A., E. Manzini, and E. Roeckner (2002), Forcing of the quasi-biennial oscillation from a broad spectrum of atmospheric waves, *Geophysical Research Letters*, *29*(8), 86–1–86–4, doi:10.1029/2002GL014756.

Hagan, M. E., and R. G. Roble (2001), Modeling diurnal tidal variability with the national center for atmospheric research thermosphere-ionosphere-mesosphere-electrodynamics general circulation model, *J. Geophys. Res.*, *106*(A11), 24,869–24,882.

Hines, C. O. (1960), Internal atmospheric gravity waves at ionospheric heights, *Can. J. Phys.*, *38*, 1441–1481.

Hines, C. O. (1997), Doppler-spread parameterization of gravity-wave momentum deposition in the middle atmosphere. Part 1: Basic formulation, *J. Atmos. Sol.-Terr. Phys.*, *59*(4), 371–386.

Hocking, W. K. (2005), A new approach to momentum flux determinations using SKiYMET meteor radars, *Ann. Geophys.*, *23*(7), 2433–2439.

Hocking, W. K., B. Fuller, and B. Vandepeer (2001), Real-time determination of meteor-related parameters utilizing modern digital technology, *J. Atmos. Sol.-Terr. Phys.*, *63*(2-3), 155–169.

Hogan, T. F., et al. (2014), The navy global environmental model, *Oceanography*, *27*(3), 116–125.

Hough, S. S. (1898), On the application of harmonic analysis to the dynamical theory of the tides. part ii: On the general integration of laplace's dynamical equations, *Philosophical Transactions of the Royal Society of London A: Mathematical, Physical and Engineering Sciences*, *191*, 139–185, doi:10.1098/rsta.1898.0005.

Huang, F. T., H. G. Mayr, C. A. Reber, T. Killeen, J. Russell, M. Mlynczak, W. Skinner, and J. Mengel (2006), Diurnal variations of temperature and winds inferred from timed and uars measurements, *Journal of Geophysical Research: Space Physics*, *111*(A10), doi:10.1029/2005JA011426, a10S04.

Immel, T. J., E. Sagawa, S. L. England, S. B. Henderson, M. E. Hagan, S. B. Mende, H. U. Frey, C. M. Swenson, and L. J. Paxton (2006), Control of equatorial ionospheric morphology by atmospheric tides, *Geophys. Res. Lett.*, *33*, L15,108, doi:10.1029/2006GL026,161.

Isler, J. R., and D. C. Fritts (1996), Gravity wave variability and interaction with lower-frequency motions in the mesosphere and lower thermosphere over hawaii, *J. Atmos. Sci.*, *55*(1), 37–48.

Jiang, Q., and J. D. Doyle (2008), On the diurnal variation of mountain waves, *Journal of the Atmospheric Sciences*, *65*(4), 1360–1377.

Kim, Y.-H., A. C. Bushell, D. R. Jackson, and H.-Y. Chun (2013), Impacts of introducing a convective gravity-wave parameterization upon the qbo in the met office unified model, *Geophysical Research Letters*, *40*(9), 1873–1877, doi:10.1002/grl.50353.

Kim, Y.-J., S. D. Eckermann, and H.-Y. Chun (2003), An overview of the past, present and future of gravity-wave drag parametrization for numerical climate and weather prediction models, *Atmosphere-Ocean*, *41*(1), 65–98, doi:10.3137/ao.410105.

Klaassen, G. (2009), Testing lagrangian theories of internal wave spectra. part ii: Varying the number of waves, *Journal of the Atmospheric Sciences*, *66*(5), 1101–1125.

Kunz, A., L. L. Pan, P. Konopka, D. E. Kinnison, and S. Tilmes (2011), Chemical and dynamical discontinuity at the extratropical tropopause based on start08 and waccm analyses, *Journal of Geophysical Research: Atmospheres*, *116*(D24), doi:10.1029/2011JD016686, d24302.

Laplace, P. (1825), *Mechanique Celeste*, *5*.

Li, C.-Y. S. H.-L. L. J. Y. T. N. D. A. K. Q. W. X. D. a. W., T. (2009), Observation of local tidal variability and instability, along with dissipation of diurnal tidal harmonics in the mesopause region over fort collins, colorado (41n, 105w), *J. Geophys. Res.*, *114*, D06,106, doi:10.1029/2008JD011089.

Lieberman, R. S., D. A. Ortland, D. M. Riggin, Q. Wu, and C. Jacobi (2010), Momentum budget of the migrating diurnal tide in the mesosphere and lower thermosphere, *J. Geophys. Res.*, *115*(D20), D20,105.

Lindzen, R. S. (1981), Turbulence and stress owing to gravity wave and tidal breakdown, *J. Geophys. Res.*, *86*, 9707–9714.

Liu, A. Z., R. G. Roble, J. H. Hecht, M. F. Larsen, and C. S. Gardner (2004), Unstable layers in the mesopause region observed with na lidar during the turbulent oxygen mixing experiment (tomex) campaign, *Journal of Geophysical Research: Atmospheres*, *109*(D2), n/a–n/a, doi:10.1029/2002JD003056, d02S02.

Liu, A. Z., X. Lu, and S. J. Franke (2013), Diurnal variation of gravity wave momentum flux and its forcing on the diurnal tide, *J. Geophys. Res.*, *118*, 1668–1678.

Liu, H.-L., J. M. McInerney, S. Santos, P. H. Lauritzen, M. A. Taylor, and N. M. Pedatella (2014), Gravity waves simulated by high-resolution whole atmosphere community climate model, *Geophysical Research Letters*, *41*(24), 9106–9112, doi:10.1002/2014GL062468, 2014GL062468.

Liu, X., J. Xu, H.-L. Liu, and R. Ma (2008), Nonlinear interactions between gravity waves with different wavelengths and diurnal tide, *J. Geophys. Res.*, *113*, D08112, doi:10.1029/2007JD009136.

Lu, X., A. Z. Liu, J. Oberheide, Q. Wu, T. Li, Z. Li, G. R. Swenson, and S. J. Franke (2011), Seasonal variability of the diurnal tide in the mesosphere and lower thermosphere over Maui, Hawaii (20.7N, 156.3W), *J. Geophys. Res.*, *116*(D17), D17,103.

Lu, X., H.-L. Liu, A. Z. Liu, J. Yue, J. M. McInerney, and Z. Li (2012), Momentum budget of the migrating diurnal tide in the Whole Atmosphere Community Climate Model at vernal equinox, *J. Geophys. Res.*, *117*(D7), D07,112, 14 PP.

Mayr, H., J. Mengel, E. Talaat, H. Porter, and K. Chan (2003), Non-migrating diurnal tides generated with planetary waves in the mesosphere, *Geophysical research letters*, *30*(16).

Mayr, H. G., J. G. Mengel, K. L. Chan, and H. S. Porter (1999), Seasonal variations and planetary wave modulation of diurnal tides influenced by gravity waves, *Advances in Space Research*, *24*(11), 1541–1544.

McCormack, J. P., S. D. Eckermann, and T. F. Hogan (2015), Generation of a quasi-biennial oscillation in an nwp model using a stochastic gravity wave drag parameterization, *Monthly Weather Review*, *143*(6), 2121–2147.

McFarlane, N. (1987), The effect of orographically excited gravity wave drag on the general circulation of the lower stratosphere and troposphere, *Journal of the atmospheric sciences*, *44*(14), 1775–1800.

McLandress, C. (1998), On the importance of gravity waves in the middle atmosphere and their parameterization in general circulation models, *J. Atmos. Sol.-Terr. Phys.*, *60*(14), 1357–1383.

McLandress, C. (2002), The seasonal variation of the propagating diurnal tide in the mesosphere and lower thermosphere. Part II: The role of tidal heating and zonal mean winds, *J. Atmos. Sci.*, *59*(5), 907–922.

McLandress, C., J. F. Scinocca, T. Shepard, M. Reader, and Manney (2013), Dynamical control of the mesosphere by orographic and nonorographic gravity wave drag during the extended northern winters of 2006 and 2009, *JOURNAL OF THE ATMOSPHERIC SCIENCES*, *70*, 2152.

Meyer, C. K. (1999), Gravity wave interactions with mesospheric planetary waves: A mechanism for penetration into the thermosphere-ionosphere system, *J. Geophys. Res.*, *104*(A12), 28,181–28,196.

Nakamura, T., D. Fritts, J. Isler, T. Tsuda, V. R.A., and I. Reid (1997), Short-period fluctuations of the diurnal tide observed with low-latitude mf and meteor radars during cadre: Evidence for gravity wave/tidal interactions, *J. Geophys. Res.*, *102*(D22), 26,225–26,238, doi:10.1029/96JD03145.

Nappo, C. J. (2013), *An introduction to atmospheric gravity waves*, Academic Press.

Oberheide, J., J. M. Forbes, X. Zhang, and S. L. Bruinsma (2011), Climatology of upward propagating diurnal and semidiurnal tides in the thermosphere, *Journal of Geophysical Research: Space Physics*, *116*(A11), doi:10.1029/2011JA016784, a11306.

Ortland, D. A. (2005), A study of the global structure of the migrating diurnal tide using generalized hough modes, *Journal of the atmospheric sciences*, *62*(8), 2684–2702.

Ortland, D. A., and M. J. Alexander (2006), Gravity wave influence on the global structure of the diurnal tide in the mesosphere and lower thermosphere, *J. Geophys. Res.*, *111*, A10S10, doi:10.1029/2005JA011,467.

Pedatella, N. M., J. Oberheide, E. K. Sutton, H.-L. Liu, J. L. Anderson, and K. Raeder (2016), Short-term nonmigrating tide variability in the mesosphere, thermosphere, and ionosphere, *Journal of Geophysical Research: Space Physics*, *121*(4), 3621–3633, doi:10.1002/2016JA022528, 2016JA022528.

Placke, M., P. Hoffmann, R. Latteck, and M. Rapp (2015), Gravity wave momentum fluxes from mf and meteor radar measurements in the polar mlt region, *Journal of Geophysical Research: Space Physics*, *120*(1), 736–750, doi:10.1002/2014JA020460, 2014JA020460.

Preusse, P., S. Eckermann, J. Oberheide, M. Hagan, and D. Offermann (2001), Modulation of gravity waves by tides as seen in crista temperatures, *Advances in Space Research*, *27*(10), 1773–1778.

Ribstein, B., U. Achatz, and F. Senf (2015), The interaction between gravity waves and solar tides: Results from 4-d ray tracing coupled to a linear tidal model, *Journal of Geophysical Research: Space Physics*, *120*(8), 6795–6817, doi:10.1002/2015JA021349, 2015JA021349.

Richter, J. H., F. Sassi, and R. R. Garcia (2010), Toward a physically based gravity wave source parameterization in a general circulation model, *Journal of the Atmospheric Sciences*, *67*(1), 136–156, doi:10.1175/2009JAS3112.1.

Rienecker, M., et al. (2008), The geos-5 data assimilation system - documentation of versions 5.0.1, 5.1.0, and 5.2.0, *Tech. rep.*, Technical Report Series on Global Modeling and Data Assimilation.

Sato, K., S. Watanabe, Y. Kawatani, Y. Tomikawa, K. Miyazaki, and M. Takahashi (2009), On the origins of mesospheric gravity waves, *Geophys. Res. Lett.*, *36*(19), L19,801.

Schirber, S., E. Manzini, T. Krismer, and M. Giorgetta (2015), The quasi-biennial oscillation in a warmer climate: sensitivity to different gravity wave parameterizations, *Climate Dynamics*, *45*(3-4), 825–836.

She, C. Y., et al. (2004), Tidal perturbations and variability in the mesopause region over Fort Collins, CO (41N, 105W): Continuous multi-day temperature and wind lidar observations, *Geophys. Res. Lett.*, *31*, L24111, doi:10.1029/2004GL021165.

Suzuki, S., K. Shiokawa, Y. Otsuka, T. Ogawa, M. Kubota, M. Tsutsumi, T. Nakamura, and D. C. Fritts (2007), Gravity wave momentum flux in the upper mesosphere derived from oh airglow imaging measurements, *Earth Planets Space*, *59*(5), 421–428.

Tang, J., A. Z. Liu, and G. R. Swenson (2002), High frequency gravity waves observed in OH airglow at Starfire Optical Range, NM: Seasonal variations in momentum flux, *Geophys. Res. Lett.*, *29*(20), 1966, doi:10.1029/2002GL015794.

Thayaparan, T., W. K. Hocking, and J. MacDougall (1995), Observational evidence of tidal/gravity wave interactions using the UWO 2 MHz radar, *Geophys. Res. Lett.*, *22*(4), 373–376.

Vichare, G., and R. Rajaram (2013), Diurnal and semi-diurnal tidal structures due to o2, o3 and h2o heating, *Journal of Earth System Science*, *122*(5), 1207–1217.

Vincent, R. A., and I. M. Reid (1983), HF Doppler measurements of mesospheric gravity wave momentum fluxes, *J. Atmos. Sci.*, *40*(5), 1321–1333.

Vincent, R. A., S. Kovalam, I. M. Reid, and J. P. Younger (2010), Gravity wave flux retrievals using meteor radars, *Geophys. Res. Lett.*, *37*(14), L14,802.

Wang, H., J. P. Boyd, and R. A. Akmaev (2016), On computation of hough functions, *Geoscientific Model Development*, *9*(4), 1477.

Warner, C. D., and M. E. McIntyre (2001), An ultrasimple spectral parameterization for nonorographic gravity waves, *J. Atmos. Sci.*, *58*(14), 1837–1857.

Watanabe, S., and S. Miyahara (2009), Quantification of the gravity wave forcing of the migrating diurnal tide in a gravity wave-resolving general circulation model, *J. Geophys. Res.*, *114*(D7), D07,110.

Williams, B. P., D. C. Fritts, C. Y. She, and R. A. Goldberg (2006), Gravity wave propagation through a large semidiurnal tide and instabilities in the mesosphere and lower thermosphere during the winter 2003 macwave rocket campaign, *Ann. Geophys.*, *24*, 1199–1208.

Xue, X.-H., H.-L. Liu, and X.-K. Dou (2012a), Parameterization of the inertial gravity waves and generation of the quasi-biennial oscillation, *Journal of Geophysical Research: Atmospheres*, *117*(D6), doi:10.1029/2011JD016778, d06103.

Xue, X.-H., H.-L. Liu, and X.-K. Dou (2012b), Parameterization of the inertial gravity waves and generation of the quasi-biennial oscillation, *Journal of Geophysical Research: Atmospheres*, *117*(D6), n/a–n/a, doi:10.1029/2011JD016778, d06103.

Yamashita, C. (2008), Lidar study of stratospheric gravity waves and their impacts on polar mesospheric clouds at the south pole and rothera, antarctica, Master's thesis, University of Colorado at boulder.

Yigit, E., A. D. Aylward, and A. S. Medvedev (2008), Parameterization of the effects of vertically propagating gravity waves for thermosphere general circulation models: Sensitivity study, *Journal of Geophysical Research: Atmospheres*, *113*(D19), n/a–n/a, doi: 10.1029/2008JD010135, d19106.

Yudin, V. A., B. V. Khattatov, M. A. Geller, D. A. Ortland, C. McLandress, and G. G. Shepherd (1997), Thermal tides and studies to tune the mechanistic tidal model using uars observations, *Annales Geophysicae*, *15*(9), 1205–1220, doi:10.1007/s00585-997-1205-9.

Yue, J., C.-Y. She, and H.-L. Liu (2010), Large wind shears and stabilities in the mesopause region observed by na wind-temperature lidar at midlatitude, *Journal of Geophysical Research: Space Physics*, *115*(A10), n/a–n/a, doi:10.1029/2009JA014864, a10307.